Adam Wittek · Poul M.F. Nielsen
Karol Miller *Editors*

Computational Biomechanics for Medicine

Soft Tissues and the Musculoskeletal System

Springer

Computational Biomechanics for Medicine

Adam Wittek • Poul M.F. Nielsen • Karol Miller
Editors

Computational Biomechanics for Medicine

Soft Tissues and the Musculoskeletal System

Springer

Editors
Adam Wittek
Intelligent Systems for Medicine Laboratory
School of Mechanical and Chemical Engineering
The University of Western Australia
35 Stirling Highway
6009 Crawley/Perth
Western Australia
Australia
adwit@mech.uwa.edu.au

Karol Miller
Intelligent Systems for Medicine Laboratory
School of Mechanical and Chemical Engineering
The University of Western Australia
35 Stirling Highway
6009 Crawley/Perth
Western Australia
Australia
kmiller@mech.uwa.edu.au

Poul M.F. Nielsen
Department of Engineering Science
Auckland Bioengineering Institute
The University of Auckland
Private Bag 92019
Auckland 1142
New Zealand
p.nielsen@auckland.ac.nz

ISBN 978-1-4419-9618-3 e-ISBN 978-1-4419-9619-0
DOI 10.1007/978-1-4419-9619-0
Springer New York Dordrecht Heidelberg London

Library of Congress Control Number: 2011928799

Preface

A novel partnership between surgeons and machines, made possible by advances in computing and engineering technology, could overcome many of the limitations of traditional surgery. By extending surgeons' ability to plan and carry out surgical interventions more accurately and with less trauma, computer-integrated surgery (CIS) systems could help to improve clinical outcomes and the efficiency of health care delivery. CIS systems could have a similar impact on surgery to that long since realized in computer-integrated manufacturing. Mathematical modeling and computer simulation have proved tremendously successful in engineering. Computational mechanics has enabled technological developments in virtually every area of our lives. One of the greatest challenges for mechanists is to extend the success of computational mechanics to fields outside traditional engineering, in particular to biology, the biomedical sciences, and medicine.

Computational Biomechanics for Medicine Workshop series was established in 2006 with the first meeting held in Copenhagen. The fifth workshop was held in conjunction with the Medical Image Computing and Computer Assisted Intervention Conference (MICCAI 2010) in Beijing on 24 September 2010. It provided an opportunity for specialists in computational sciences to present and exchange opinions on the possibilities of applying their techniques to computer-integrated medicine.

Computational Biomechanics for Medicine V was organized into two parts: "Computational Biomechanics of Soft Tissues, Flow, and Injury Biomechanics" and "Computational Biomechanics of Musculoskeletal System and Its Tissues. Generation of Patient-Specific Finite Element Meshes." The application of advanced computational methods to the following areas was discussed:

- Medical image analysis
- Image-guided surgery
- Surgical simulation
- Surgical intervention planning
- Disease prognosis and diagnosis
- Injury mechanism analysis

After a rigorous review of manuscripts (8–12 pages), we accepted 13 papers which are included in this volume. The proceedings also include abstracts of two invited

lectures by world-leading researcher Professor Ming Zhang from The Hong Kong Polytechnic University, and Tsuyoshi Yasuki, General Manager of Advanced CAE Division at Toyota Motor Corporation, Japan.

Information about Computational Biomechanics for Medicine Workshops, including proceedings of previous meetings is available at http://cbm.mech.uwa.edu.au/.

We thank the MICCAI 2010 organizers for help with administering the workshop, the invited lecturers for deep insights into their research fields, the authors for submitting high quality work, and the reviewers for helping with paper selection.

Crawley, WA — Karol Miller
Auckland, New Zealand — Poul M.F. Nielsen
Crawley, WA — Adam Wittek

Contents

Contributors

Leon Axel Department of Radiology, New York University, New York, NY, USA, Leon.Axel@nyumc.org

Andrey N. Chernikov Computer Science Department, Old Dominion University, Norfolk, VA 23529, USA, andrey.n.chernikov@gmail.com

Nikos P. Chrisochoides Computer Science Department, Old Dominion University, Norfolk, VA 23529, USA, npchris@gmail.com

Anthony Doyle Auckland City Hospital, Auckland, New Zealand, ADoyle@adhb.govt.nz

Andriy Fedorov Department of Radiology, Brigham and Women's Hospital, Harvard Medical School, 75 Francis St, Boston, MA 02115, USA, fedorov@bwh.harvard.edu

L.M.J. Florack Department of Mathematics and Computer Science, Eindhoven University of Technology, Eindhoven, The Netherlands, l.m.j.florack@tue.nl

Panagiotis A. Foteinos Computer Science Department, College of William and Mary, VA 23187, USA
and
Computer Science Department, Old Dominion University, Norfolk, VA 23529, USA, pafotein@gmail.com

Nobuhiko Hata Department of Radiology, Brigham and Women's Hospital, Harvard Medical School, 75 Francis St, Boston, MA 02115, USA, hata@bwh.harvard.edu

J. Hennig Department of Diagnostic Radiology – Medical Physics, University Hospital, Freiburg, Germany
and
Freiburg Institute for Advanced Studies (FRIAS), Freiburg, Germany, juergen.hennig@uniklinik-freiburg.de

Harvey Ho Bioengineering Institute, University of Auckland, Auckland, New Zealand, harvey.ho@auckland.ac.nz

Peter Hunter Bioengineering Institute, University of Auckland, Auckland, New Zealand, p.hunter@auckland.ac.nz

Grand R. Joldes Intelligent Systems for Medicine Laboratory, School of Mechanical and Chemical Engineering, The University of Western Australia, 35 Stirling Highway, 6009 Crawley/Perth, WA, Australia, grandj@mech.uwa.edu.au

Wayne Jones Auckland City Hospital, Auckland, New Zealand, WayneJ@adhb.govt.nz

J.G. Korvink Freiburg Institute for Advanced Studies (FRIAS), Freiburg, Germany
and
Department of Microsystems Engineering, University of Freiburg, Freiburg, Germany, korvink@imtek.de

H. Köstler Lehrstuhl Informatik 10, Universität Erlangen-Nürnberg, Cauerstraße 6, 91058 Erlangen, Germany, harald.koestler@informatik.uni-erlangen.de

Jennifer A. Kruger Auckland Bioengineering Institute, The University of Auckland, Auckland, New Zealand, j.kruger@auckland.ac.nz

K.C. Li Department of Radiology, Xuanwu Hospital, Capital Medical University, Beijing, China, likuncheng1955@yahoo.com.cn

Yixun Liu Computer Science Department, College of William and Mary, VA 23187, USA
and
Computer Science Department, Old Dominion University, Norfolk, VA 23529, USA, yxliuwm@gmail.com

Z. Liu Changchun Institute of Optics, Fine Mechanics and Physics (CIOMP), Chinese Academy of Science, Changchun, China, zhenyu_ciomp@hotmail.com

M. Loch Lehrstuhl Informatik 10, Universität Erlangen-Nürnberg, Cauerstraße 6, 91058 Erlangen, Germany, lochmartin84@aol.com

Jiajie Ma Intelligent Systems for Medicine Laboratory, School of Mechanical and Chemical Engineering, The University of Western Australia, 35 Stirling Highway, 6009 Crawley/Perth, WA, Australia, jiajie@civil.uwa.edu.au

M. Markl Department of Diagnostic Radiology – Medical Physics, University Hospital, Freiburg, Germany, michael.markl@uniklinik-freiburg.de

Stephen McAnearney Intelligent Systems for Medicine Laboratory, School of Mechanical and Chemical Engineering, The University of Western Australia, 35 Stirling Highway, 6009 Crawley/Perth, WA, Australia, s.mcanearney@gmail.com

Dimitris Metaxas Department of Computer Science, Rutgers University, New Brunswick, NJ, USA, dnm@cs.rutgers.edu

Karol Miller Intelligent Systems for Medicine Laboratory, School of Mechanical and Chemical Engineering, The University of Western Australia, 35 Stirling Highway, 6009 Crawley/Perth, WA, Australia, kmiller@mech.uwa.edu.au

Albert Montillo GE Global Research Center, Niskayuna, NY, USA
and
Department of Computer Science, Rutgers University, Piscataway, NJ, USA, montillo@ge.com

Martyn P. Nash Department of Engineering Science, Auckland Bioengineering Institute, The University of Auckland, Auckland, New Zealand, martyn.nash@auckland.ac.nz

Poul M.F. Nielsen Department of Engineering Science, Auckland Bioengineering Institute, The University of Auckland, Private Bag 92019, Auckland 1142, New Zealand, p.nielsen@auckland.ac.nz

Jaykumar Puthran Auckland Bioengineering Institute, The University of Auckland, Auckland, New Zealand, j.puthran@auckland.ac.nz

Vijay Rajagopal Auckland Bioengineering Institute, The University of Auckland, Auckland, New Zealand, v.rajagopal@auckland.ac.nz

Hayley M. Reynolds Auckland Bioengineering Institute, The University of Auckland, Auckland, New Zealand, h.reynolds@auckland.ac.nz

O. Röhrle Institut für Mechanik (Bauwesen), Universität Stuttgart, Pfaffenwaldring 7, 70569 Stuttgart, Germany, roehrle@simtech.uni-stuttgart.de

F.F.J. Simonis Department of Biomedical Engineering, Eindhoven University of Technology, Eindhoven, Netherlands, f.f.j.simonis@student.tue.nl

A.F. Stalder Department of Radiology, Xuanwu Hospital, Capital Medical University, Beijing, China
and
Department of Diagnostic Radiology – Medical Physics, University Hospital, Freiburg, Germany, afstalder@gmail.com

G.J. Strijkers Department of Biomedical Engineering, Eindhoven University of Technology, Eindhoven, Netherlands, g.j.strijkers@tue.nl

Clare Tempany Department of Radiology, Brigham and Women's Hospital, Harvard Medical School, 75 Francis St, Boston, MA 02115, USA, ctempany@bwh.harvard.edu

H.C. van Assen Department of Biomedical Engineering, Eindhoven University of Technology, Eindhoven, The Netherlands, h.c.v.assen@tue.nl

Kumar Vemaganti University of Cincinnati, Cincinnati, OH, USA, Kumar.Vemaganti@gmail.com

Simon K. Warfield Computational Radiology Laboratory, Children's Hospital Boston and Harvard Medical School, 300 Longwood Avenue, Boston, MA 02115, USA, simon.warfield@childrens.harvard.edu

J.J.M. Westenberg Radiology, Leiden University Medical Center, Leiden, The Netherlands, j.j.m.westenberg@lumc.nl

Adam Wittek Intelligent Systems for Medicine Laboratory, School of Mechanical and Chemical Engineering, The University of Western Australia, 35 Stirling Highway, 6009 Crawley/Perth, WA, Australia, adwit@mech.uwa.edu.au

Jian Wu Department of Neurosurgery, Mianyang Central Hospital, Mianyang, Sichuan, China, stock_www@126.com

Xiani Yan Auckland Bioengineering Institute, The University of Auckland, Auckland, New Zealand, xyan075@aucklanduni.ac.nz

Jikuang Yang Research Center of Vehicle Traffic Safety/SKLVB, Hunan University, Changsha, China and
Department of Applied Mechanics, Chalmers University of Technology, Gothenburg, Sweden, jikuang.yang@chalmers.se

Tsuyoshi Yasuki Toyota Motor Corporation, 1 Toyota-cho, Toyota, Aichi, 471-8572, Japan, yasuki@giga.tec.toyota.co.jp

Ming Zhang Department of Health Technology and Informatics, The Hong Kong Polytechnic University, Hong Kong, China, htmzhang@inet.polyu.edu.hk

Benjamin Zwick Intelligent Systems for Medicine Laboratory, School of Mechanical and Chemical Engineering, The University of Western Australia, 35 Stirling Highway, 6009 Crawley/Perth, WA, Australia, benzwick@gmail.com

Part I
Computational Biomechanics of Soft Tissues, Flow and Injury Biomechanics

Development of Total Human Model for Safety Version 4 Capable of Internal Organ Injury Prediction

Tsuyoshi Yasuki

Abstract Although internal organ injury in car crashes occurs at a relatively lower frequency compared to bone fracture, it tends to be ranked higher in terms of injury severity. A generalized injury risk can be assessed in car crash tests by evaluating abdominal force and viscous criterion (VC) using a crash test dummy, but the injury risk to each organ cannot be estimated with current dummies due to a lack of parts representing the internal organs. Recently, human body modeling research has been conducted introducing organ parts. It is still a challenge to simulate the impact behavior of organ parts and their injury, based on an understanding of the differences in structure and material properties among the organs.

In this study, a next generation human body FE model named Total Human Model for Safety (THUMS) version 4 has been developed to predict internal organ injury. The model represents the geometry of organ parts, their location in a living human body, and their connections to surrounding tissues. The features of each organ part were taken into account in modeling, so that compressive material was assumed for hollow organs while incompressive material was applied to solid organs. Besides the major organ parts, other soft tissues such as membranes and fatty tissues were also incorporated in order to simulate relative motions among organs. The entire model was examined comparing its mechanical response to that in the literature. The study confirmed that the force-deformation response of the torso against anterior loading showed a good correlation with that of tested subjects.

T. Yasuki (✉)
Toyota Motor Corporation, 1 Toyota-cho, Toyota, Aichi, 471-8572, Japan
e-mail: yasuki@giga.tec.toyota.co.jp

A. Wittek et al. (eds.), *Computational Biomechanics for Medicine: Soft Tissues and the Musculoskeletal System*, DOI 10.1007/978-1-4419-9619-0_1,

Investigation of Brain Trauma Biomechanics in Vehicle Traffic Accidents Using Human Body Computational Models

Jikuang Yang

Abstract This chapter aimed to study the biomechanical response and injury mechanisms of brain in passenger car-to-pedestrian collision event. The kinematics of head impact to a passenger car was reconstructed using multibody dynamics (MBD) models. The brain injury biomechanics was investigated by using an FE model of human body head (HBM-head). The HBM-head model was developed in accordance with human head anatomy. The model consists of scalp, skull, dura mater, cerebrospinal fluid, pia mater, cerebrum, cerebellum, ventricle, brain stem, falx, tentorium, etc. The existing data from cadaveric head impact tests were used to validate the head FE model. The kinematic and kinetic responses of the head were determined by using MBD model. The brain injury-related physical parameters and the distribution of the intracranial pressure were calculated from simulations of head impact to the windscreen and A-pillar by using the HBM-head model. It is proved that the head FE model has good biofidelity and can be used to study head–brain trauma and injury mechanisms in vehicle collisions.

Keywords Traffic injury · Brain trauma · Head FE model · Pedestrian MBD model · Impact biomechanics

1 Introduction

The serious and fatal brain injuries are observed frequently in vehicle traffic accidents, which is a public health issue worldwide. It resulted in a large number of social and economic problems due to head trauma-related deaths, treatment and insurance compensation. To minimize the risk of brain injury in the accident, there is a need of advanced tools to get good knowledge about the kinematics of the accidents

J.K. Yang (✉)
Research Center of Vehicle Traffic Safety/SKLVB, Hunan University, Changsha, China
and
Department of Applied Mechanics, Chalmers University of Technology, Gothenburg, Sweden
e-mail: jikuang.yang@chalmers.se

A. Wittek et al. (eds.), *Computational Biomechanics for Medicine: Soft Tissues and the Musculoskeletal System*, DOI 10.1007/978-1-4419-9619-0_2,

and the causation of brain trauma as well as the correlation of brain injuries with the physical parameters in a vehicle crash environment.

In the past years, the head injury mechanisms and technology of injury prevention have been extensively studied by medical doctors and researchers in vehicle traffic safety field all over the world. Many studies on head–brain injury biomechanics were carried out by using physical and mathematical models. The finite element (FE) technique is an effective method for the prediction of human body injuries and analysis of injury mechanisms from vehicle traffic accidents. The finite element method was therefore developed rapidly and applied in the research field of head–brain injury biomechanics in recent two decades. These include the work of Ueno [1], Lighthall [2], Nagashima et al. [3], Chu [4], Trosseille [5], Bandak [6], Chu et al. [7], DiMasi et al. [8], Mendis et al. [9], Willinger et al. [10], Ueno et al. [11], Nishimoto and Murakami [12], Anderson et al. [13], Huang et al. [14], Willinger et al. [15], and Bradshaw et al. [16]. A number of the 3D head models have been presented and used to study human head response. For example, the head–brain FE model WSUBIM [17] was developed in Wayne State University in the USA, the ULP model [18] in Université Louis Pasteur, and the HUMOS model in EU 5th framework program (Human Models for Safety), THUMS model in Japan.

At the same time, these models have been used to study the trauma from vehicle traffic and sport accidents. The application of the validated FE models indicated that the FE models play an important role in the studies of mechanism of brain injuries by analyzing the intracranial pressure and the stress and strain of brain tissues. In order to accurately reflect the biomechanical response and injury mechanism of human head trauma in different crash accidents, it is necessary to further develop the brain FE model with the improved characteristics of human head in both the anatomy structure and the material models of biological tissues. It is also vital for researcher to evaluate the validity of the models using available biomechanical data from experimental studies. These issues have attracted an increasing attention in the simulation study on the human brain FE models.

The aim of this chapter is to investigate the mechanism of brain injury in vehicle collision by using a developed FE model of human body head (HBM-head) in accordance with human head–brain anatomy.

2 Method and Materials

The FE model of HBM-head was developed based on 3D anatomical image data [19]. The preprocessing and meshing of head brain 3D anatomy image data was carried out using Hypermesh software. The computations of brain biomechanics responses were carried out using nonlinear explicit dynamics finite element algorithm in LS-DYNA 3D code. The effectiveness of the head model was verified by comparing the results of the Nahum's impact experiment [20] using human head specimen. The sensitivity and biofidelity of the FE model for predicting brain injury were detected through parameter analysis at different impact speeds.

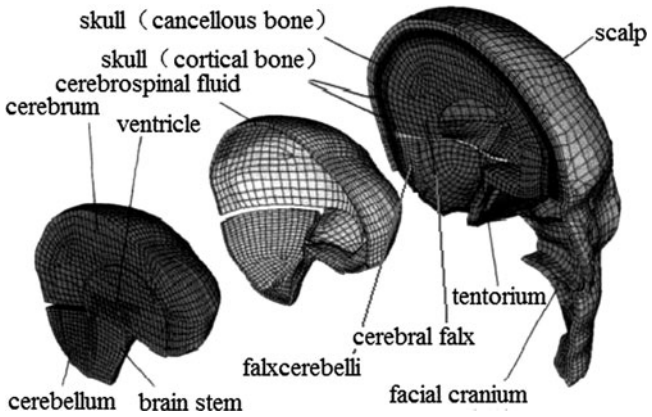

Fig. 1 An FE model of head was developed based on human head anatomy. The model consists of scalp, skull, cerebrospinal fluid (CSF), cerebrum, cerebellum, ventricle, brain stem, falx, and tentorium, etc.

2.1 Description of the HBM-Head FE Model

The HBM-head model consists of the scalp, skull, dura mater, cerebrospinal fluid (CSF), pia mater, cerebrum, cerebellum, ventricle, brain stem, falx, tentorium, etc. as shown in Fig. 1. The head is modeled using 66,624 nodes, 49,607 solid elements of eight-noded hexahedron, and 11,514 shell elements. The mass of the head model is 4.4 kg, which was based on the anthropometry size of a 50th male adult human body.

The thickness of scalp is defined as 5–7 mm [21] and it is described with two-layer solid elements. Skull was modeled with a hierarchical structure in the sandwich form of cortical bone and cancellous bone. The thickness of skull is about 5–7 mm. The two-layer solid element was used to simulate accurately the anatomical geometry of both sides of the skull. Dura mater is simulated with one layer of shell elements. The CSF of subarachnoid space is described using solid elements with a low shear modulus. The relative motion between the skull and brain is simulated by the relative sliding between the dura mater and CSF. The outer surface of CSF is defined to simulate arachnoids. The structure under the CSF is pia mater that closes the brain surface. The inner surface of CSF is defined to simulate the pia mater. The falx between the two hemispheres of the brain and the tentorium between the cerebrum and cerebellum are represented by solid elements. The overall quality of mesh was controlled in the process of modeling as shown in Table 1.

2.2 Material Parameters

Bio-tissue materials show typical viscoelastic properties related to load and speed. Viscoelastic material model is widely used to describe the material properties of

Table 1 Quality control parameters of elements

Quality control parameters	Threshold
Warpage	<35.20
Aspect ratio	<10.70
Skew	<64.00
Min. size	>0.70
Jacobian	>0.47
Min. angle quad	>16.69
Max. angle quad	<160.65

Table 2 Material definition of model components

Part	Material property	[a]$E/^{a}k$(MPa)	Poisson ratio	G_0(kPa)	G_∞(kPa)	$\beta(s^{-1})$
Falx	Elastic	31.5	0.45			
Tentorium	Elastic	31.5	0.45			
Cortical bone	Elastic	15,000	0.21			
Cancellous bone	Elastic	4,600	0.05			
Scalp	Elastic	16.7	0.42			
Cerebellum	Viscous Elastic	2,190		10	2	80
Cerebrum	Viscous Elastic	2,190		12.5	2.5	80
CSF	Viscous Elastic	1,050		1	0.9	80
Brain stem	Viscous Elastic	2,190		22.5	4.5	80
Dura mater	Elastic	31.5	0.45			
Pia mater	Elastic	11.5	0.45			

[a]E = Young's modulus, k = bulk modulus

brain tissue [17–19]. Researches have shown that water accounts for nearly 78% in brain tissue that result in incompressible characteristics. For the HBM-head model, a linear viscoelastic material was selected in this study, as the maximal strain of the head model is 0.1965 at an impact speed of 12 m/s in this study, which is based on Bathe [22]. The shear elasticity behavior of this material was obtained from the follow equation:

$$G(t) = G_\infty + (G_0 - G_\infty)\mathrm{e}^{-\beta t}$$

where G_0: short-term shear modulus, G_∞: long-term shear modulus, β: decay constant, t: time.

The bulk modulus of brain tissue was defined as 2.19 GPa, and the shear modulus was changed between 680 Pa and 268 kPa. The material parameters in literature [17–19] were used in HBM-head model as shown in Table 2. In order to obtain an accurate simulation of the relative motion between brain and skull during impact, the shear modulus and bulk modulus of CSF were lower than brain tissue. The material of cortical bone and cancellous bone were defined in reference to the skull material properties of the ULP model [18].

2.3 Contact Interface

During an event of vehicle crash, the cerebral meninges and CSF between the skull and brain will lead to a relative sliding between the skull and brain due to effect of inertial loading of the translation and rotation acceleration. There is very thin space filled with CSF between the dura mater and arachnoid preventing these structures sticking together. The CSF plays an important role for energy absorption and damping during an impact. This effect has been investigated by using finite element (FE) model of craniocerebral. There is space between arachnoid and pia mater and the space is filled with CSF. Some of blood vessel are going into the brain tissue. Some thin filament structures called arachnoid trabeculation in subarachnoid extend to pia mater from arachnoid. They play a role of fixing the pia mater to arachnoid. Based on the above knowledge of anatomy, a HBM-head FE model was developed using solid and shell elements. The dura mater is a layer attached to the inner surface of skull. The inferior of dura mater is a layer arachnoid. The pia mater is the membrane that is closely attached to the surface of brain tissue. Elements simulating pia mater are attached to the surface of brain. Outside of brain are elements representing CSF. The arachnoid is simulated by the outer surface of CSF. The contact algorithm was defined between dura mater and arachnoid in the HMB-head model. The solid elements between ventricle and brain tissue were connected using the common nodes.

2.4 Model Validation

The model was validated with the data from head impact experiments by Nahum [20]. The experimental samples were human cadavers without antiseptic treatment. The head was loaded at a certain speed using a rigid impactor with padding. The experiments were divided into two groups. The samples used in the first group have the numbers of 36–38, 41–44, and 54. The mass of impactor was defined from 5.23 to 23.09 kg. The velocity was from 4.36 to 12.95 m/s. The numbers of the second group were 46–52. These experiments were carried out at different speeds to the same sample and the speed changed from 4.42 to 8.69 m/s. And the mass of impactor was 5.23 kg. Different padding materials of impactor were used to obtain the proper impact duration.

The contact force between the impactor and head, the centroid acceleration of head and the pressure in five different positions from the Nahum experiments [20] were used in the validation of the model. The five positions were brain tissue region near the impact location on the frontal bone; the brain tissue of the side of parietal bone located in the upper of the juncture of coronal suture and squamous suture; the inferior part of the lambdoid suture of occipital bone; and the nucleus fastigii of cerebella of occipital. The detail curve data of NO 37 experiment was showed in Nahum's paper [20]. So the results of this experiment were selected to validate the simulation model. The mass of the cylinder impactor is 5.59 kg and the speed of impact is 9.94 m/s in the experiment.

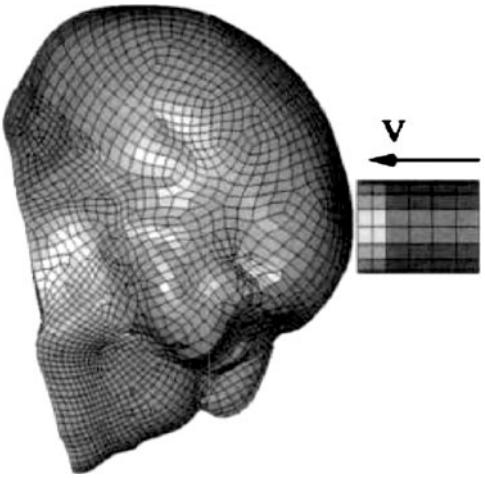

Fig. 2 Configuration for model validation

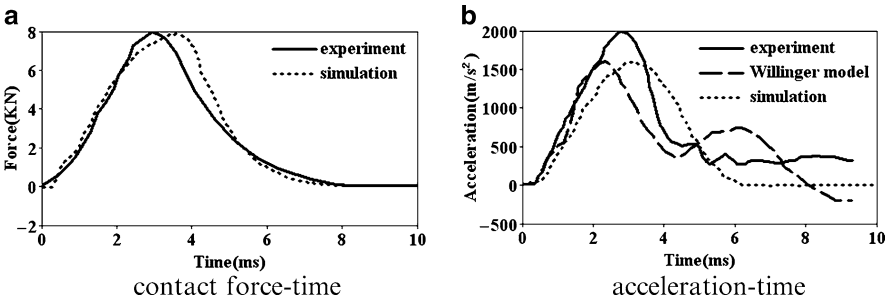

Fig. 3 The comparison of time history curve between Nahum experiment [20] and simulation

Figure 2 illustrates the configuration for simulation of the head impact test. The boundary conditions of simulation were defined based on test configurations. As the impact time was so short that the neck has little effect on head response in such short time. We assumed that the boundary condition of head is free. Referring to the Nahum experiment [20], the head was forward incline in order to make the Frankfurt plane to horizontal plane at an angle of 45°. The model of impactor with the padding materials was developed simulated by using foam material in the front end. In order to obtain the impact characteristic of padding materials, pre-analysis of different foam material were carried out with the stress–strain curves of corresponding material. According to the experiment method of Willinger et al., the mass of the cylinder impactor was set to 6.8 kg and the speeds of impact changed from 6 to 9.94 m/s.

Analysis of simulations indicated that the calculated contact force agreed well with the Nahum experiment at 6.8 m/s. The impact contact force is shown in Fig. 3.

Figure 3a illustrated a comparison of the impact forces between results from the simulation and the experiment. The accelerations of center of mass from the

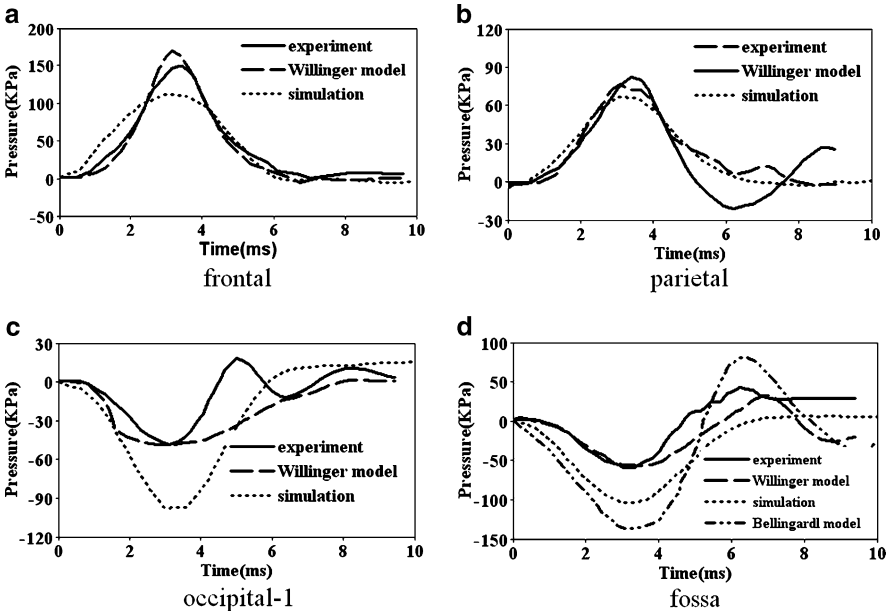

Fig. 4 The comparison of intracranial pressure time history curves between experiment and simulation

simulation, Nahum's experiment [20] and Kang's study [15] are given in Fig. 3b. The comparison among the intracranial pressure is shown in Fig. 4 in terms of results from simulation of this model and the experiment, as well as simulation curves by Kang's using ULP model and Belingardi, etc. [23].

3 Investigation of Brain Injury in Vehicle Collisions

In passenger car-to-adult pedestrian accidents, the head injuries attract particular attention due to the severe or fatal consequences. Many studies have been carried out in this area but the injury mechanisms and the tolerances of brain remain controversial. A study of the skull–brain injury mechanisms was conducted by using a MBD pedestrian model [24] and the HBM-head FE model (Fig. 5).

Head trauma accident data were selected from IVAC accident database [25] which was developed based on in-depth investigations of vehicle accidents in Changsha, China. A passenger car-to-pedestrian impact at 45 km/h was reconstructed using multibody dynamic (MBD) models to acquire the head impact conditions for the head impact velocity, head position, and head orientation. The HBM-head FE model was used for the reconstruction of skull fracture and brain injuries via a virtual test of head impact against windscreen and A-pillar (Fig. 5).

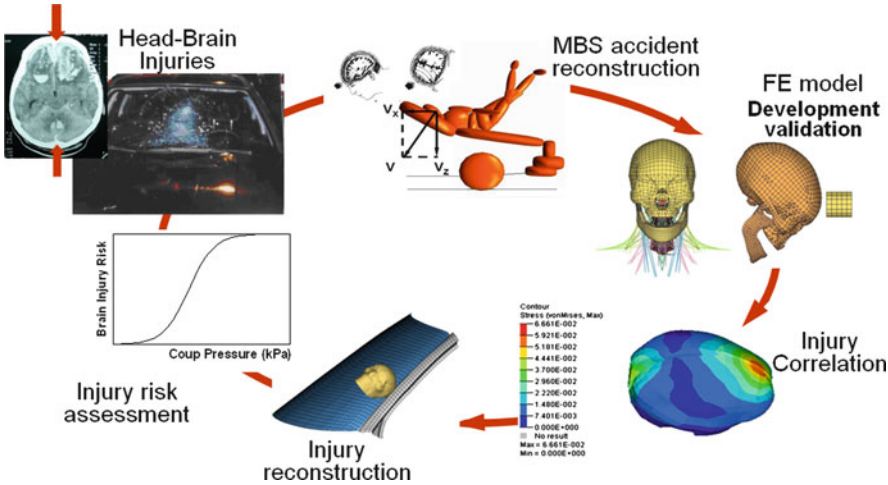

Fig. 5 A computational study of brain injury biomechanics based on accident data by using MBD and FE models

A stress analysis was conducted to determine the correlation of the stress and pressure distributions of the brain model with the injuries observed in the head–windscreen collisions.

From head–windscreen impact, the received contact force of the HBM-head model is 4.4 kN and the intracranial pressure maximum 250 kPa. From head–A-pillar impact, the received contact force of the HBM-head model is average 16 kN and the intracranial pressure maximum 815 kPa.

The skull fracture appeared in A-pillar impact, and there is no fracture in windscreen impact. The intracranial pressure maximum 250 kPa from windscreen impact could correlate with minor coup/countercoup injuries. The intracranial pressure maximum 815 kPa from A-pillar impact could correlate with severe coup/countercoup injuries.

It is necessary to point out that the approach used for calculation of the physical parameters for brain injuries in car-to-pedestrian impact will result in certain deviation. This could be due to the difference of the effective head mass between the FE head impact modeling and the head impact modeling with MBD pedestrian model in which a neck constraint force applied to the head [26].

The reconstruction results indicated that coup/countercoup pressure, Von Mises and shear stress were important physical parameters to evaluate the brain injury risk. The relationship between skull fracture and the predicted physical parameters can be determined. Thereby, we can finally obtain reasonable advices to improve safety design of car frontal structure for minimizing the risk of pedestrian head injuries.

4 Conclusions

Using both the MBD and HBM-head FE models is a valuable approach for reconstruction of vehicle-to-pedestrian collisions and analysis of the dynamic responses and injury-related physical parameters. For further study of the brain parameters, it is important to get an effective head mass in the simulations.

The brain injury-related parameters such as the head acceleration, stress, strain, contralateral intracranial pressure can be obtained, which indicate that the model can be used to study typical traffic injuries and the injury mechanism. Furthermore, the acquired knowledge can be used to improve the car safety design for protection of pedestrian head injuries.

Acknowledgments This study was sponsored by NSFC No. 10472031, the National "863 Program" No. 2006AA110101, the Ministry of Education of China "111 program" No. 111-2-11, and the SKLVB project No. 60870004.

References

1. Ueno, K., Melvin, J.W., Lundquist, E. and Lee, M.C.: Two-dimensional finite element analysis of human Brain Impact Responses: Application of a Scaling Law, Crashworthiness and Occupant Protection in Transportation Systems, Ed T.B. Khalil, AMD-Vol,106/BED-Vol,13, ASME, 1989:123–124.
2. Lighthall, J.W., Melvin, J.W., and Ueno, K.: Toward a Biomechanical Criterion for Functional Brain Injury. Proc. 12th Int. Techn. Conf. on Experimental Safety Vehicles, 1989: 627–633.
3. Nagashima, T., Shirakuni, T., and Rapoport, SI.: A two-dimensional, finite element analysis of vasogenic brain edema. Neurol Med Chir (Tokyo).1990;30:1–9.
4. Chu, C.S. and Lee, M.C.: Finite Element Analysis of Cerebral Contusion, Advances in Bioengineering, ASME-BED-Vol 20 1991:601–604.
5. Trosseille, X., Tarriere, C., Lavaste, F., Guillon, F., Domont, A.: Development of a FEM of the human head according to a specific test protocol, Proc. 30th Stapp Car Crash Conf, pp 235–253, SAE 922527, 1992.
6. Bandak, F.A, Eppinger, R.H.: A three Dimensional Finite Element Analysis of the Human Brain Under Combined Rotational and Translational Accelerations, Proc, 38th Stapp Car Crash Conf, 1994:145–163.
7. Chu, C.S., Lin, M.S., Huang, H.M., and Lee, M.C.: Finite element analysis of cerebral contusion. Journal of Biomechanics 1994;27:187–94.
8. DiMasi, F.P., Eppinger, R.H., and Bandak, F.A.: Computational analysis of head impact response under car crash loadings. Proc. 39th Stapp Car Crash Conference, SAE Paper No. 952718.Society of Automotive Engineers, Warrendale, PA. 1995.
9. Mendis, K., Stalnaker, R.L., and Advani, A.H.: A constitutive relationship for large deformation finite element modeling of brain tissue. J. Biomech. Engrg. 1995;117:279–285.
10. Willinger, R., Taleb, L., and Kopp, C-M.: Modal and temporal analysis of head mathematical models. Journal of Neurotrauma.1995;12:743–754.
11. Ueno, K., Melvin, J.W., Li, L., and Lighthall, J.W. Development of tissue level brain injury criteria by finite element analysis Journal of Neurotrauma 1995:12:695–706.
12. Nishimoto, T., Murakami, S.: Relation between diffuse axonal injury and internal head structures on blunt impact. Journal of Biomechanical Engineering.1998;120:140–147.

13. Anderson, R.W.G., Brown, C.J., Blumbergs, P.C., Scott, G., Finney, J.W., Jones, N.R., and McLean, A.J.: Mechanisms of axonal injury: an experimental and numerical study of a sheep model of head impact. Proc. International Conference on the Biomechanics of Impact (IRCOBI), 1999:107–120.
14. Huang, H.M., Lee, M.C., Chiu, W.T., Chen, C.T., and Lee, S.Y.: Three-dimensional finite element analysis of subdural hematoma. Journal of Trauma 1999:47:538–44.
15. Willinger, R., Kang, H.S., and Diaw, B.: Three-dimensional human head finite-element model validation against two experimental impacts. Ann Biomed Eng. 1999;27:403–10.
16. Bradshaw, D.R., Ivarsson, J., Morfey, C.L., and Viano, D.C.: Simulation of acute subdural hematoma and diffuse axonal injury in coronal head impact. Journal of Biomechanics 2001;34:85–94.
17. Zhang, L Y, Yang, KH, Dwarampudi, R. et al.: Recent advances in brain injury research: a new human head model development and validation. Proceeding of the 45th Stapp Car Crash Conference, San Antonio, Texas, 2001:23.
18. Willinger R, Ryan GA, McLean AJ, et al.: Mechanisms of brain injury related to mathematical modelling and epidemiological data. Accident Analysis and Prevention, 1994;26:767.
19. Yang, J.K., Xu, W., Otte, D.: 2008. Brain injury biomechanics in real word vehicle accident using mathematical models. Chinese Journal of Mechanical Engineering 21 (4), 81–86.
20. Nahum AM, Smith RW, Ward CC.: Intracranial pressure dynamics during head impact. Proceeding of the 21st Stapp Car Crash Conference, New Orleans, Louisiana, USA, 1977:339.
21. Horgan, T. J.: A finite element model of the human head for use in the study of pedestrian accidents(Doctor dissertation). College Dublin, National University of Ireland, 138–140. (2005).
22. Bathe, K.-J.: Finite Element Procedures, Prentice-Hall, Upper Saddle River, NJ: Prentice Hall, (1996).
23. Belingardi, G, Chiandussi, G, Gaviglio I.: Development and validation of a new finite element model of human head. Proc. 19th International Technical Conference of the Enhanced Safety of Vehicle (ESV), Washington, DC. 2005:35.
24. Yang, J.K., Lövsund, P., Cavallero, C. Bonnoit, J.: A Human- 3D Mathematical Model for Simulation of Car-Pedestrian Impacts. Traffic Injury Prevention, Vol. 2(2), pp. 131–149. (2000).
25. Kong, C.Y., Yang, J.K.: Logistic regression analysis of pedestrian casualty risk in passenger vehicle collisions in China. Accident Analysis & Prevention 42(4):987–993, (2010).
26. Yao JF, Yang, JK, Otte, D, Fredriksson R.: Reconstruction of Head-to-Bonnet Top Impact in Child Pedestrian-to-Passenger Car Crash. International IRCOBI Conference on the Biomechanics of Impact. ISBN/ISSN: 2-9514210-6-0, pp. 29–39, (2005).

Blood Flow Simulation in a Giant Intracranial Aneurysm and Its Validation by Digital Subtraction Angiography

Harvey Ho, Jian Wu, and Peter Hunter

Abstract In this study we simulate the blood flow in a giant aneurysm using computational fluid dynamics (CFD) techniques and validate the results using the 2D X-ray image sequence generated from digital subtraction angiography (DSA). The 3D geometry of the aneurysm was retrieved from a computed tomography angiography (CTA) image. The pulsatile blood flow was numerically solved, and the hemodynamic quantities such as the wall shear stress (WSS) and flow velocity field were analyzed at four instants of a cardiac cycle. The computed intra-aneurysm flow velocity was validated using a DSA sequence over several time frames. The time-averaged flow velocity ($\sim$0.2 m/s) agreed with the flow velocity estimated from the DSA. We further compared the Newtonian blood model with a non-Newtonian (Carreau) model and found that the Newtonian model overestimated the flow velocity and WSS.

Keywords Blood flow · Giant aneurysm · Digital subtraction angiography · Model

1 Introduction

In recent years, many image-based patient-specific computational fluid dynamics (CFD) models have been constructed for cerebral aneurysms (e.g., in [1–3]). These models provide an economic way to evaluate important hemodynamic quantities such as the wall shear stress (WSS) which are otherwise difficult to determine in vivo, or expensive to measure in vitro. The computed flow quantities may be further used for pathophysiological analysis and therapeutic planning [1, 4].

One of the main problems of patient-specific CFD models, however, is that they are difficult to validate in vivo. Indeed, many of the patient-specific CFD models were performed in the absence of in vivo validations. Although non-invasive validation methods, such as the phase contrast MR angiography (PC MRA) and the

H. Ho (✉)
Bioengineering Institute, University of Auckland, Auckland, New Zealand
e-mail: harvey.ho@auckland.ac.nz

A. Wittek et al. (eds.), *Computational Biomechanics for Medicine: Soft Tissues and the Musculoskeletal System*, DOI 10.1007/978-1-4419-9619-0_3,

transcranial Doppler sonography (TCD), do provide the possibility of measuring blood flow velocities, their current spatial and temporal resolutions have restricted their use in small intracranial arteries [5].

Hence, it is useful to explore other validation methods. In clinical practices, digital subtraction angiography (DSA) has been a "gold standard" in vascular disease diagnosis [1]. This procedure uses a catheter, which is inserted into a puncture site (usually the femoral artery) and advanced to a target location. By releasing a radio-opaque contrast agent, the anatomy of vascular lesions is revealed in X-ray images [1]. Although the main purpose of DSA is to yield the anatomic information of diseased vessels, it can also be used to estimate blood flow velocities from the movements of the contrast agent, and can thus be used for CFD validation purposes [1,6].

The DSA sequence reported in [1,6] was of low temporal resolution (2 Hz) and was not able to capture the dynamic *intra-aneurysmal* flow path. The purpose of this work is twofold: first, we present a computational pipeline from patient-specific vascular structure extraction to CFD simulation; second, we use a DSA sequence with a higher frequency (10 Hz) to quantitatively validate the CFD results for a giant intracranial aneurysm.

2 Method

2.1 Image Scanning

We retrospectively studied a CT angiography (CTA) image (GE Lightspeed VCT, GE Healthcare, Waukesha, Wisconsin) in which a giant cerebral aneurysm was found (Fig. 1a). The resolution of the CTA image was $0.432 \times 0.432 \times 0.625$ mm. A DSA (Infinix Celeve VS; Toshiba, Tokyo, Japan) scanning was further performed to gain a whole picture of the cerebral vasculature, using a temporal frequency of 10 Hz. The giant aneurysm and other blood vessels are shown in Fig. 1b.

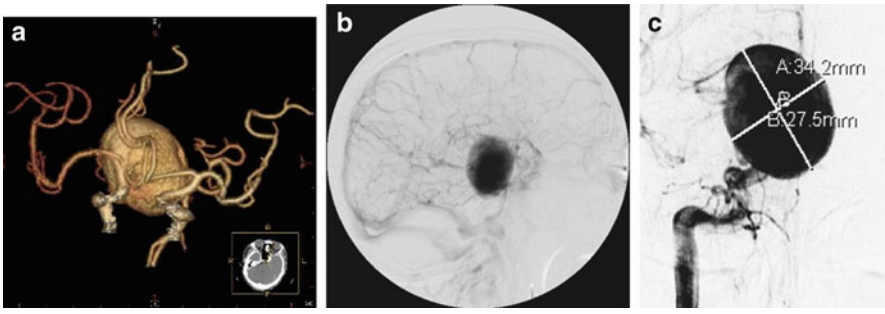

Fig. 1 (**a**) A giant intracranial aneurysm revealed in CTA image; (**b**) the anatomy of the aneurysm and blood vessels in its vicinity; (**c**) the size of the giant aneurysm

The aneurysm arises from the distal end of the right inner carotid artery (ICA) before it bifurcates into the right middle and anterior cerebral arteries (MCA and ACA). The size of this aneurysm is 34.2 and 27.5 mm along the long and short axis, respectively (Fig. 1c). This size is larger than the dimensional definition of giant intracranial aneurysms (fundus diameter $\geq$25 mm) [7].

2.2 *Surface Model Construction and Computational Grid Generation*

Based on the CTA image, the giant aneurysm was segmented and digitized into a surface mesh (Fig. 2a) using a MIMICS 10.0 software (Materialise, Leuven, Belgium). Note that the two efferent vessels (MCA and ACA) are much smaller than the afferent vessel (ICA).

To enable flow simulation to be properly carried out, the inlet, i.e., the ICA and the outlets, should be extruded so that the boundary flow effects will have a minimum influence on the intra-aneurysmal flow. This was performed using @neuFUSE, an imaging/visualization tool developed by @neurIST, as follows: (1) a 3D skeleton was extracted from the 3D vascular structure (Fig. 2b); (2) the inlet and outlet vessels were cropped at proper locations along the skeleton; and (3) the vessel ends were extruded (Fig. 2c).

Another essential CFD preprocessing procedure is the computational grid generation, whereby the flow domain (i.e., the volume contained inside the surface mesh) was discretized into numerous small elements. We used a grid generator ICEM (ANSYS Inc., Canonsburg, PA) and the resulting grid contains 618,000 tetrahedral elements (Fig. 3).

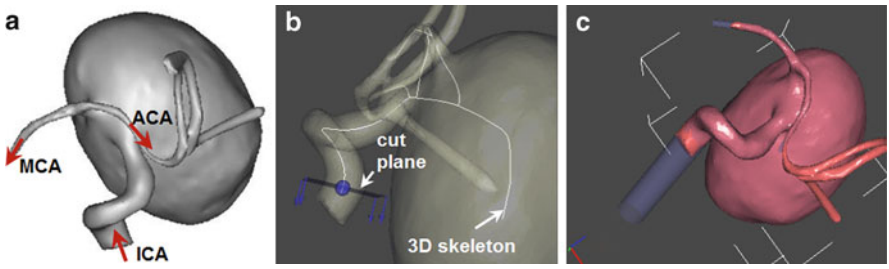

Fig. 2 Aneurysm model construction and boundary treatment: (**a**) surface mesh of the aneurysm; (**b**) a 3D skeleton was extracted and a cut position was defined; (**c**) the end vessel was extruded to facilitate CFD analysis

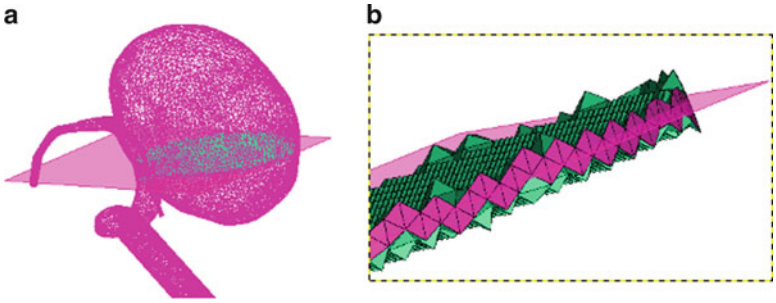

Fig. 3 Computational grid generation: (**a**) computational mesh generation; (**b**) a closer look at the computational elements (control volumes)

2.3 Flow Simulation

2.3.1 Governing Equations

Since the aneurysm size (27.5–34.2 mm) is much larger than the size of blood cells ($\sim$5 µm), the blood can be modeled as a continuum. The governing Navier–Stokes equation can be expressed in a vector form:

$$\nabla \cdot \mathbf{v} = 0 \tag{1}$$

$$\rho \left(\frac{\partial \mathbf{v}}{\partial \mathbf{t}} + \mathbf{v} \cdot \nabla \mathbf{v} \right) = -\nabla p + \nabla \cdot \tau \tag{2}$$

where $\mathbf{v}$ represents the flow velocity in 3D space, ρ is the blood density, p is the pressure, and τ is the shear stress.

2.3.2 Newtonian vs. Non-Newtonian Blood Models

For a Newtonian fluid, the shear stress (τ) has a linear relationship with the shear rate ($\dot{\gamma}$) and its viscosity (μ) is a constant. However, blood is a non-Newtonian fluid and it exhibits shear-thinning properties, especially at low shear rates ($<100\,\mathrm{s}^{-1}$) [8]. The question now is: what is the range of blood shear rates in this giant aneurysm? Figure 4a answers this question: the shear rate in a large portion of the giant aneurysm surface is under $100\,\mathrm{s}^{-1}$. For this reason, non-Newtonian models are more suitable for hemodynamics modeling for this aneurysm.

Various non-Newtonian models exist, e.g., the Carreau, Casson, and Power Law models [8]. In this work, we adopt the Carreau model which is expressed as:

$$\mu = \mu_\infty + (\mu_0 - \mu_\infty)[1 + (\lambda \dot{\gamma})^2]^{(n-1)/2} \tag{3}$$

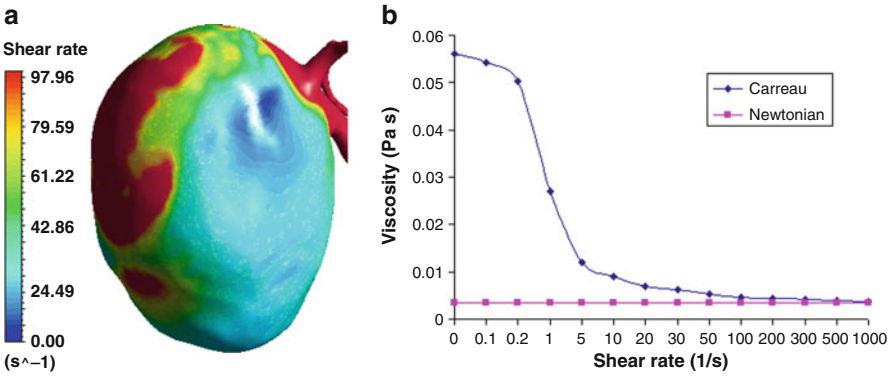

Fig. 4 (**a**) The shear rate in a large portion of aneurysm is under 100 s^{-1}; (**b**) Viscosity–Shear rate curves of the Newtonian and Carreau blood models

where μ_0, μ_∞ are blood viscosities when the shear rate is zero (μ_0) and when the shear rate is high enough so that blood can be treated as a Newtonian fluid (μ_∞). The parameters n and λ are obtained by fitting (3) with experimental data. We adopt their values from [8]: $\lambda = 3.313$ s, $n = 0.3568$, $\mu_0 = 0.056$ Pa s and $\mu_\infty = 0.00345$ Pa s.

Based on (3), we plot the viscosity–shear rate (μ-$\dot{\gamma}$) curves for the blood as a Newtonian fluid as well as a non-Newtonian fluid (Fig. 4b). Note that the blood viscosity decreases with an increased shear rate, especially in low shear rates (hence the term "shear-thinning"). The viscosity tends to be equivalent to the Newtonian viscosity (μ_∞) in high shear rates.

2.3.3 Flow Solver

To solve the governing equations, (1) and (2) were integrated over each of the small elements (also known as control volumes) of Fig. 3 to yield discretized equations. A commercial finite-volume-based flow code CFX 11.0 (ANSYS Inc., Canonsburg, PA) was used to solve these equations numerically [9].

Since blood flow in the middle cerebral region is pulsatile, we adopted the flow velocity waveform of ICA from our previous 1D model [10] (shown in Fig. 5a) and applied it as the inflow boundary condition. The zero pressure was used as the outflow boundary condition to allow free flow. Since the wall deformation of intracranial arteries is small [1, 2], the aneurysmal wall was simplified as rigid and no-slip condition was applied.

In the actual CFD simulation, a cardiac cycle was assumed to be 1 s. The temporal step was set as 0.01 s, and within each time step ten iterations were performed for numerical convergence.

3 Results

3.1 CFD Simulation

The transient flow over four cardiac cycles took about 16.5 h to compute on a desktop computer (Pentium Dual-Core 2.39 GHz), and the result at the last cycle was used for hemodynamic analysis. The computational results were post-processed at four time instants ($t = 0.25$, 0.5, 0.75, and 1.0 s) spanning both systole and diastole. Figure 5b visualizes the WSS at the aneurysm wall, and Fig. 5c shows the velocity streamline constructed from the flow field.

The CFD results suggest that the flow velocities (and hence the WSS yielded from radial velocity gradient) in the two small efferent arteries (MCA and ACA) are much higher than that in the aneurysm and the afferent artery (ICA): the mean flow velocity in MCA and ICA is about 2 m/s, while in ICA it is 0.3 m/s. This is due to the conservation law of mass: the inflow from the large ICA must be equal to the outflow from the much smaller MCA and ACA over a cardiac cycle.

Inside the aneurysm, the highest WSS (~2.1 Pa at systole, see Fig. 6) occurs at the region along the blood flow path and close to the ICA, whereas the WSS at the lateral wall is lower (0–0.5 Pa). The flow velocity streamlines, shown in Fig. 6, indicate that the highest flow velocity is about 0.7 s^{-1}, while the flow is stagnant at the center of the aneurysm.

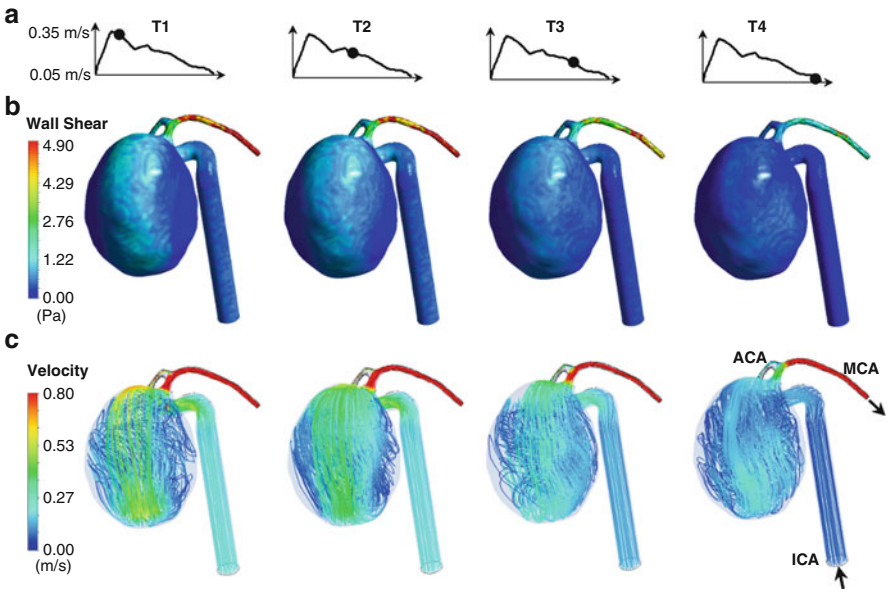

Fig. 5 CFD results of the giant aneurysm at four instants (0.25, 0.5, 0.75, and 1.0 s): (**a**) the velocity waveform (adopted from [10]) as the inflow boundary condition; (**b**) the WSS distribution at the aneurysm; (**c**) the velocity streamline (using 50 seed points) of the aneurysm

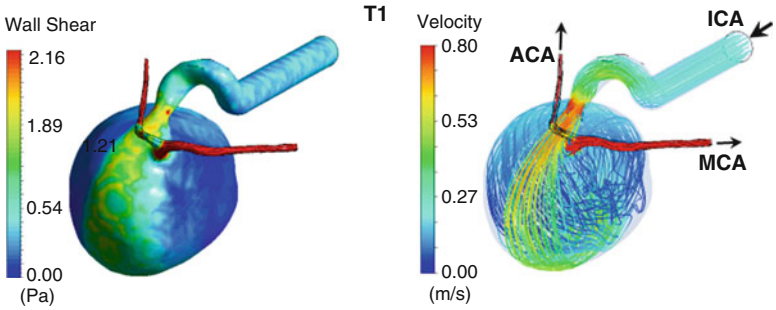

Fig. 6 The WSS and flow streamline at systole ($T1 = 0.25$ s)

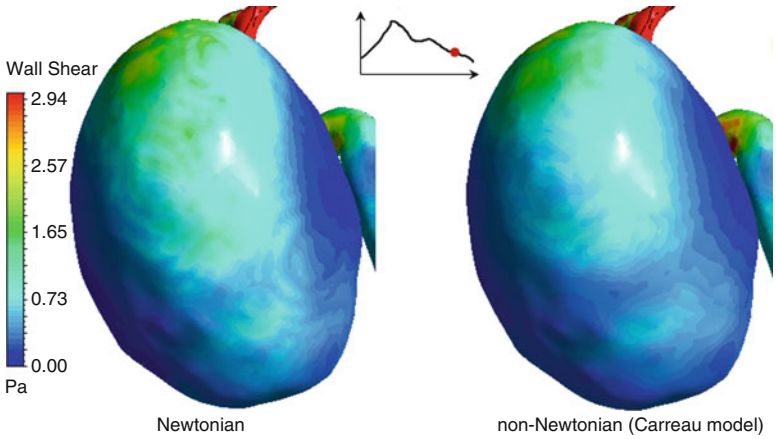

Fig. 7 Comparison of Newtonian and non-Newtonian blood models: the WSS for the new-Newtonian model is slightly lower at low shear rate regions ($t = 0.8$ s)

3.2 Effects of Non-Newtonian Blood Model

In the above simulation, the blood was modeled as a Newtonian fluid which is a good approximation when the shear rate is high (e.g., $>100\,\mathrm{s}^{-1}$) [11]. However, the shear rate and shear stress in the giant aneurysm are low in a large portion of aneurysm (as shown in Fig. 4a). Therefore, a non-Newtonian model is more suitable especially at low shear regions.

In order to observe the difference between the Newtonian and non-Newtonian models, a comparison of their WSS distributions ($t = 0.8\,s$, i.e., in diastole) is shown in Fig. 7. It can be seen that the low WSS regions is slightly larger in the Carreau model than the Newtonian model. We further check the flow velocity profile on a slice plane of the aneurysm (Fig. 8). Comparisons between the two models were made when $t = 0.3$ s (systole) and 0.8 s (diastole). In both instants, the velocity profiles of the Carreau model are more flattened than the Newtonian model.

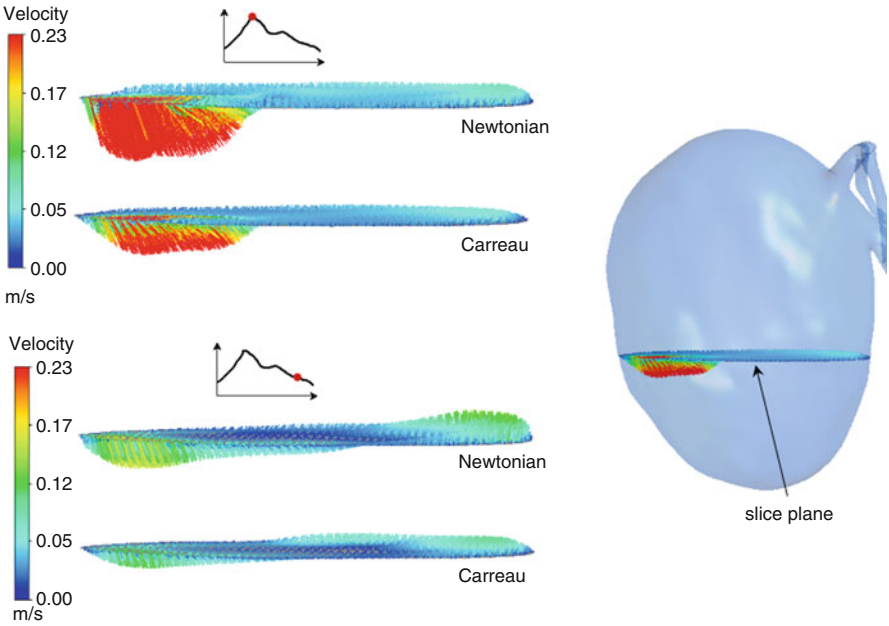

Fig. 8 Comparison of Newtonian and non-Newtonian blood models: the velocity profiles of the slice plane for the Carreau model is more flattened than the Newtonian model

This phenomena can be explained from the fact that higher blood viscosities occur in low shear rates (see the graph of Fig. 4b). Thus, a higher resistance or "drag force" slows blood flow down and leads to a more flattened profile. This observation is consistent with that reported in [8] and [11].

3.3 Validation

3.3.1 WSS Magnitude

The WSS results were compared with published data of MCA aneurysms in Shojima et al. [2] and Chien et al. [3], using the same 6-region method, i.e., WSS were evaluated from three sections crossing the aneurysm neck, middle, and top, and three other sections from the parent artery. The comparison, shown in Table 1, suggests that the computed WSS values are consistent with the results of other research groups.

Table 1 Comparison of WSS with literature. Unit: Pa(=N/m^2)

Time step	Our model	Shojima et al. [2]	Chien et al. [3]
Highest WSS	9.2	14.39 ± 6.21	15.0
Mean WSS	5.7	10.3 ± 5.2	11.7 ± 3.6

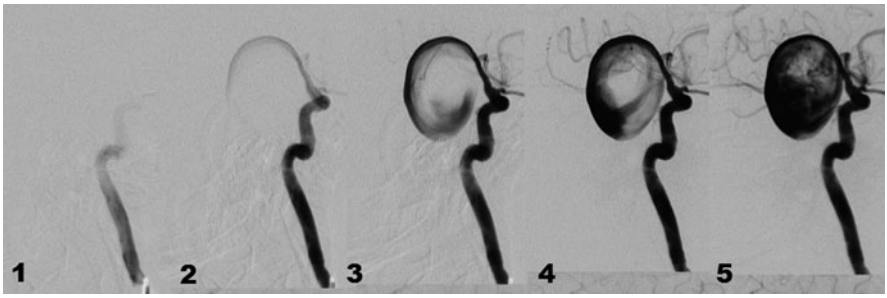

Fig. 9 DSA sequence showing the flow path of the contrast agent at $t = 1.2$, 1.6, 2.0, 2.4, and 2.8 s, respectively

3.3.2 Intra-aneurysmal Flow Velocity

The intra-aneurysmal flow velocity may be estimated directly from the DSA sequence upon careful examination of the distance and time which the contrast agent had traveled. For instance, in Fig. 9 the front of the contrast agent arrived at the neck of the aneurysm at instant 1 ($t = 1.2$ s); at instant 2 ($t = 1.6$ s) the agent front reached the middle lateral wall. Since the diameter of the aneurysm is about 35 mm (see Fig. 2c), the distance traveled by the contrast agent was approximately 55 mm. The travel time between instants 1 and 2 was $1.6\,\text{s} - 1.2\,\text{s} = 0.4\,\text{s}$, and the flow velocity therefore was $55 \div 0.4 \approx 138$ (mm/s). The mean flow velocities of four instants (visualized in Fig. 5c), on the other hand, is about 190 mm/s. We deem the difference is within an acceptable range. This difference may be further minimized by adopting the actual in vivo inflow velocity waveform using Doppler ultrasonography, which was not taken for this patient.

3.3.3 Flow Path Shape

A comparison was also made between the DSA sequence and CFD results regarding the shape of the flow path. This is shown in Fig. 10: the blood diverged after entering the aneurysm (indicated by black arrows), and the blood flow adhesively along the aneurysmal wall (indicated by the white arrows). These flow phenomena are seen in both DSA imaging and CFD results. It is also notable that the band width/thickness of the flow path is similar between the DSA and CFD results.

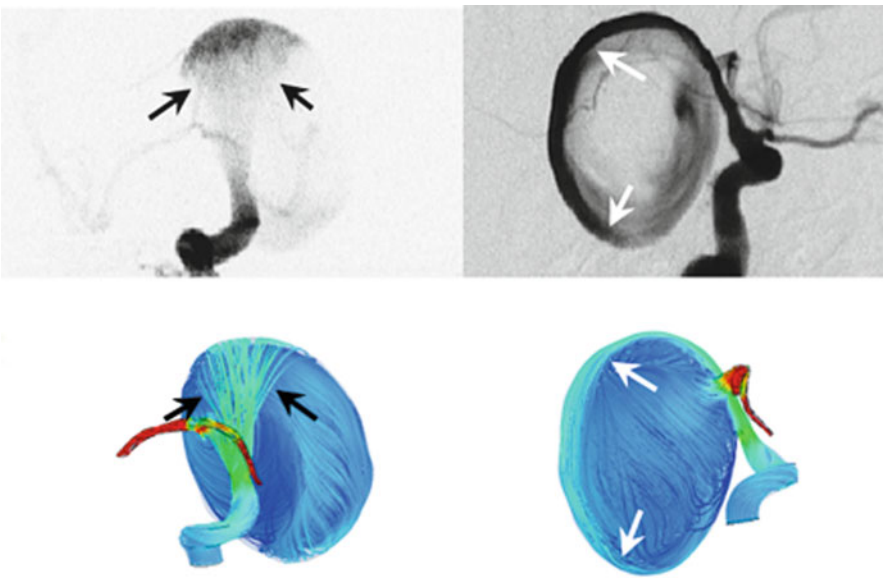

Fig. 10 Blood flow patterns: a comparison between DSA and CFD

4 Discussion

Clinical treatment of giant intracranial aneurysms remains as a daunting challenge for neurosurgeons and interventional radiologists alike [7]. Among the many factors that lead to the poor prognosis of giant aneurysms, hemodynamics is suggested to play an important role. Clearly, CFD can be used in the quantification of hemodynamic factors involved in giant aneurysms, given a suitable model is used. In this work, we compared the Newtonian model with a non-Newtonian (Carreau) blood model. We found that the Newtonian model overestimated the flow velocity and WSS, and that the velocity profiles of non-Newtonian flow are more flattened than Newtonian flow. This is a good example showing that computational results must be carefully validated to reliably interpret flow-induced effects such as vessel wall remodeling and growth.

There is no "standard" in vivo method for validating hemodynamic data. In this work, we used a series of DSA images to validate the CFD-derived flow velocities. Compared with other methods such as PC-MRA, this technique has the advantage that it can show the contrast agent movement hence the blood flow patterns, as evidenced in Fig. 9.

Estimating blood flow velocity information from 2D X-ray images is not new. Researchers have suggested different techniques such as transient measurement and optic flow for the estimation of flow velocities [12]. Also, the qualitative "reality check" type of flow streamline comparison between CFD and DSA (similar to Fig. 10) has been described in [1, 6]. However, applying a quantitatively

estimated blood flow velocity (from X-ray images) directly to CFD validation, to our knowledge, has not been reported.

The drawback of using DSA as a validation method, however, is that it is an invasive procedure. There are complication possibilities associated with the vascular access procedures, i.e., inserting a catheter into a puncture site. The manipulation of catheters may also cause injuries to the vessel lumen. On the other hand, since our study was performed in a retrospective manner, such kind of validation causes no extra pain/complication to patients but rather better utilizes the available data.

5 Conclusion

In this work, we performed a CFD simulation for the blood flow in a giant intracranial aneurysm digitized from a CTA image. The WSS results were compared with literature, and the CFD-derived velocities were compared with the flow velocity estimated from a DSA image sequence. We have shown that DSA can be a useful tool for CFD validation.

Acknowledgments This work was financially supported by a grant from the European aneurysm project @neurIST, which we gratefully acknowledge.

References

1. Steinman, D., Milner, J., Norley, C.J., Lownie, S.P., Holdsworth, D.W.: Image-based computational simulation of flow dynamics in a giant intracranial aneurysm. AJNR Am J Neuroradiol (2003) 559–566
2. Shojima, M., Oshima, M., Takagi, K., Torii, R., Hayakawa, M., Katada, K., Morita, A., Kirino, T.: Magnitude and role of wall shear stress on cerebral aneurysm. Stroke **35** (2004) 2500–2505
3. Chien, A., Castro, M., Tateshima, S., Sayre, J., Cebral, J., Vinuela, F.: Quantitative hemodynamic analysis of brain aneurysms at different locations. AJNR Am J Neuroradiol **30**(8) (2009) 1507–1512
4. Wetzel, S., Meckel, S., Frydrychowicz, A., Bonati, L., Radue, E., Scheffler, K., Hennig, J., Markl, M.: In vivo assessment and visualization of intracranial arterial hemodynamics with Flow-Sensitized 4D MR imaging at 3T. AJNR Am J Neuroradiol **28**(3) (2007) 433–438
5. McKinney, A., Palmer, C., Truwit, C., Karagulle, A., Teksam, M.: Detection of aneurysms by 64-Section multidetector CT angiography in patients acutely suspected of having an intracranial aneurysm and comparison with digital subtraction and 3D rotational angiography. AJNR Am J Neuroradiol **29**(3) (2008) 594–602
6. Ford, M., Stuhne, G., Nikolov, H., Habets, D., Lownie, S., Holdsworth, D., Steinman, D.: Virtual angiography for visualization and validation of computational models of aneurysm hemodynamics. Medical Imaging, IEEE Transactions on **24**(12) (2005) 1586 –1592
7. Peerless, S.J., Drake, C.G.: Treatment of giant cerebral aneurysms of the anterior circulation. Neurosurgical Review **5**(4) (1982) 149–154
8. Johnston, B.M., Johnston, P.R., Corney, S., Kilpatrick, D.: Non-Newtonian blood flow in human right coronary arteries: steady state simulations. Journal of Biomechanics **37**(5) (2004) 709–720

9. ANSYS: ANSYS CFX-Solver, Release 10.0: Theory. ANSYS Europe Ltd. (2005)
10. Ho, H., Sands, G., Schmid, H., Mithraratne, K., Mallinson, G., Hunter, P.: A hybrid 1D and 3D approach to hemodynamics modelling for a Patient-Specific cerebral vasculature and aneurysm. In: Medical Image Computing and Computer-Assisted Intervention MICCAI 2009. (2009) 323–330
11. Fisher, C., Rossmann, J.S.: Effect of Non-Newtonian behavior on hemodynamics of cerebral aneurysms. Journal of Biomechanical Engineering **131** (2009) 091004–9
12. Bogunovic, H., Loncaric, S.: Blood flow and velocity estimation based on vessel transit time by combining 2D and 3D X-Ray angiography. In: Medical Image Computing and Computer-Assisted Intervention MICCAI 2006. (2006) 117–124

Patient Specific Hemodynamics: Combined 4D Flow-Sensitive MRI and CFD

A.F. Stalder, Z. Liu, J. Hennig, J.G. Korvink, K.C. Li, and M. Markl

Abstract Both 4D flow-sensitive MRI and computational fluid dynamics (CFD) have successfully been applied to analyze complex 3D flow patterns in the cardiovascular system. However, both modalities suffer from limitations related to spatiotemporal resolution, measurement errors, and noise (MRI) or incomplete model assumptions and boundary conditions (CFD). The aim of this study was to directly compare the results of 4D flow-sensitive MRI and CFD in a simple model system in vitro and in complex models of the thoracic aorta in vivo. By comparing both modalities within a single framework, discrepancies were observed but the overall patterns were coherent. If adequate methods are used (e.g., patient-specific boundary conditions, fine boundary layer mesh), CFD can compute very accurate flow and vessel wall parameters, such as wall shear stress (WSS). The combination of 4D flow-sensitive MRI and CFD can be used to refine both methodologies, which may help to enhance the assessment and understanding of blood flow in vivo.

Keywords 4D flow-sensitive MRI · CFD · Hemodynamics · Blood flow

1 Introduction

The study of local hemodynamics within anatomically complex regions of the human vascular system is of high interest since these sites are predisposed to vascular diseases. Many studies have shown a correlation between disturbed flow patterns and the development of vascular disease (e.g., atherosclerosis, aneurysms) [1]. In this context, magnetic resonance imaging (MRI) offers the unique advantage

A.F. Stalder (✉)
Department of Radiology, Xuanwu Hospital, Capital Medical University, Beijing, China
and
Department of Diagnostic Radiology – Medical Physics, University Hospital, Freiburg, Germany
e-mail: afstalder@gmail.com

A. Wittek et al. (eds.), *Computational Biomechanics for Medicine: Soft Tissues and the Musculoskeletal System*, DOI 10.1007/978-1-4419-9619-0_4,

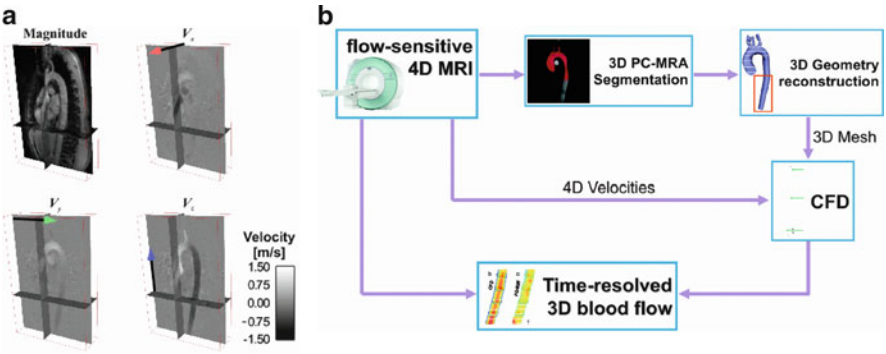

Fig. 1 (**a**) 3D flow-sensitive MRI includes anatomy and three-directional velocities over a 3D volume. (**b**) Combination of 4D flow-sensitive MRI and CFD: arterial geometry and blood velocities are extracted from 4D flow data and are eventually used for the boundary conditions for CFD. The combined information of blood flow hemodynamics from 4D flow-sensitive MRI and CFD can be used to validate the CFD or to assess the error of flow-sensitive MRI

to simultaneously assess the morphology and function in vivo. In particular, 4D flow-sensitive MRI presents a complete 3D coverage as well as an intrinsic sensitivity to flow in all the three directions (Fig. 1a).

Limitations of flow-sensitive MRI (or PC-MRI) include the relatively long imaging time and limited spatiotemporal resolution. In addition, several sources of errors affect flow-sensitive MRI and result in limited signal-to-noise ratio (SNR). 2D flow-sensitive imaging is now widely used in the clinical routine but due to its additional complexity, 3D flow-sensitive imaging is not yet part of the standard clinical methods.

An alternative approach to 4D flow-sensitive MRI is provided by CFD models with realistic boundary conditions (i.e., vascular geometry and inflow provided by computed tomography (CT), MRI, or ultrasound) as reported in a number of previous studies [2–4]. In this approach, the blood velocities are not directly measured over the complete arterial structures but are calculated based on fluid mechanics laws. However, blood flow in the arteries is particularly complex, including phenomena such as non-Newtonian rheology, compliant and moving arteries, and fluid–wall interactions. It is still debated how restricting assumptions on blood rheology, vessel properties, or blood-vessel interactions may affect the accuracy of the results. Due to limited knowledge on those phenomena and/or high complexity of computational models, those aspects are often neglected.

The aim of the presented method was to combine 4D flow-sensitive MRI and CFD into a single framework in order to enhance blood flow estimations. Consequently, 4D flow-sensitive MRI was used for the finite element model definition (geometry and boundary conditions) as well as for verification of the CFD solution. This integration allows the CFD solution and the MR measurements to be compared against each other in the same environment and coordinate system. In addition, the combination of both modalities in a single framework allows the initialization of the solver for the finiteelement model using the 3D velocities measured with MRI.

This combination has the potential to refine the assessment of blood flow in vivo by correcting the MR velocities based on flow models and refining the CFD models based on MR velocities.

2 Methods

2.1 4D Flow-Sensitive MRI

Data were acquired on a 3T MR system (Magnetom TRIO, Siemens, Germany, $G_{\max} = 40$ mT/m, rising time $= 200\,\mu$s, eight-channel receive coil) with a 4D flow-sensitive MRI sequence in a flow model in vitro and a healthy volunteer in vivo.

The flow model consisted in a rigid PVC tube with 3.4 cm inner diameter connected to a clinical bloodpump-system (Deltastream DP2, Medos, Stolberg, Germany), which produced a constant (nonpulsatile) flow of contrast agent (Gd-BOPTA, Multihance, Bracco) doped distilled water at 37° C. The 3D flow-sensitive MRI acquisition parameters were voxel size $= 0.4 \times 0.4 \times 0.6\,\text{mm}^3$, venc $= 0.5\,$m/s, TE/TR $= 4.62/8\,$ms, bandwidth $= 440\,$Hz/pixel, $\alpha = 13°$.

The thoracic aorta of a young healthy volunteer (age: 26, male) was imaged after injection of a blood pool contrast agent (MS325, Vasovist; Schering AG) using a respiration-controlled and ECG-gated 4D flow-sensitive MRI sequence (3) (spatial resolution $= 2.82 \times 1\text{m}.67 \times 3.5\,\text{mm}^3$, temporal resolution $= 48.8\,$ms, venc $= 1.5\,$m/s, TE/TR $= 3.67/6.1\,$ms, bandwidth $= 480\,$Hz/pixel, $\alpha = 13°$).

2.2 MR-Based CFD

The underlying principle of this approach is illustrated in Fig. 1b. On one hand, 4D flow-sensitive MRI is used to generate a 3D geometry. On the other hand, the velocity information is used for the boundary conditions for CFD. 4D flow-sensitive MRI and CFD results are then combined in a single framework to provide optimal estimation of hemodynamics in vivo.

2.2.1 Geometry Reconstruction

Based on the 4D flow-sensitive MRI data, a phase-contrast angiography (PC-MRA) was first calculated [5]:

$$I^{\text{PC-MRA}}\left(\vec{k}\right) = \frac{1}{N_t}\sum_{t_i=1}^{N_t}\left(I_{t_i}^{\text{mag}}\left(\vec{k}\right)\right)^2 \cdot \left|v_{t_i}\left(\vec{k}\right)\right|^2 \tag{1}$$

where t_i represent the time frames from 1 to N_t; $I_{t_i}^{\text{mag}}(\vec{k})$ is the normalized anatomy intensity magnitude at the time frame t_i. $\left|v_{t_i}(\vec{k})\right|$ is the magnitude of the velocity vector at the time frame t_i. $\vec{k} = (k_1, k_2, k_3) \in Z^3$ represents the discrete spatial coordinates.

The segmentation of the arteries was performed on the 3D PC-MRA data using level-set active contours (ITK-SNAP, Penn Image Computing and Science Lab, University of Pennsylvania, USA [6]). The initialization of the active contour was performed by manually positioning at least one seed sphere within the artery. The algorithm was evolved until segmentation of the complete arterial structure was achieved (Fig. 2).

The active contour segmentation generated a level-set volume which was further processed in order to generate an unstructured surface mesh (Paraview, Kitware Inc., NY, USA) (Fig. 3a–*a*). The unstructured mesh was then cleaned, simplified (quadric edge collapse decimation), and smoothed (Laplacian filter) using MeshLab (Visual Computing Lab – ISTI – CNR) (Fig. 3a–*c*). The resulting surface (with subvoxel resolution) was used for a geometry reconstruction based on Non-Uniform Rational B-Spline (NURBS, Fig. 3a–*d*) (Geomagic Studio 9, Geomagic Inc., NC, USA; Fachhochschule Nordwestschweiz, R. Kaiser).

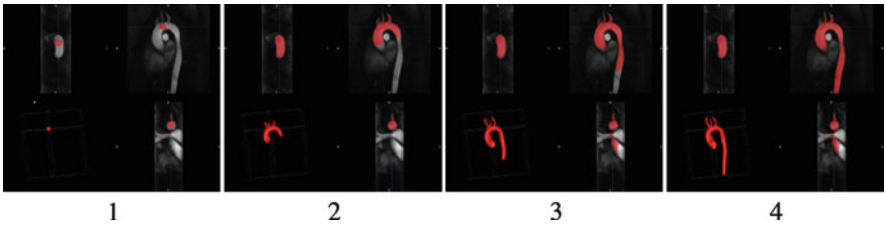

Fig. 2 3D active contour segmentation based on 3D PC-MRA: a single sphere used as initialization in the aortic arch (*image 1*) resulted in the segmentation of the complete thoracic aorta (*image 4*) after 2,500 iterations (approximately 3 min on a desktop computer)

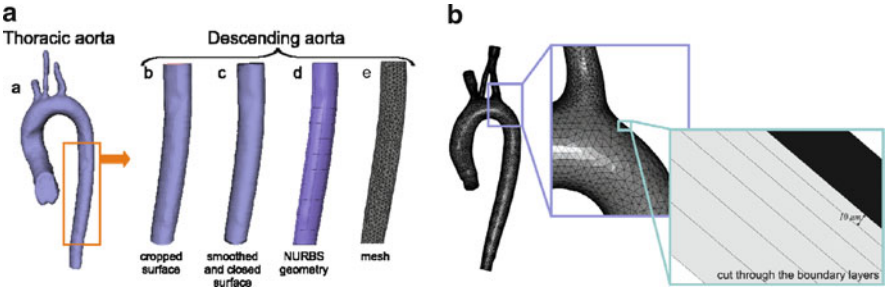

Fig. 3 (**a**) Processing of the arterial wall geometry for the descending aorta model. *a*: Unstructured surface mesh of the thoracic aorta. *b*: Selection of the descending part of the aorta. *c*: Surface after Laplacian filtering and with closed boundaries. *d*: Reconstructed geometry based on NURBS. *e*: Subdomain mesh. (**b**) Boundary layer mesh of the thoracic aorta model: the mesh is constructed of 1.9×10^6 elements including the mesh elements in the six boundary layers

The meshing was realized using a free mesher that automatically created an unstructured mesh of the subdomain with tetrahedral and prism elements (Fig. 3a−*e*). In order to reliably assess shear stresses at the surface boundaries, boundary layer meshes were used in one model. The boundary layers consisted of triangular elements over six layers, with an initial layer thickness of 10 μm and a stretching factor of 1.2 [7, 8] (Fig. 3b).

2.2.2 CFD Solver

The measured flow-sensitive 4D MRI data was used to define inflow and outflow boundary conditions which matched the in vivo situation. In order to map MR-velocities onto the knots of the mesh and at the time step required by the CFD solver, interpolation schemes were used in the spatial (tri-linear interpolation) and temporal (cosine interpolation) domains. In addition, the temporal domain was extended by periodicity (according to the cardiac period).

The Navier–Stokes equations for a Newtonian and incompressible fluid formed a partial differential equation (PDE) system:

$$\begin{cases} \rho\left(\dfrac{\partial \vec{v}}{\partial t}t + \vec{v}\cdot\nabla\vec{v}\right) = -\nabla p + \nabla\cdot\left[\eta\left(\nabla\vec{v} + (\nabla\vec{v})^T\right)\right] + \vec{f} \\ \nabla\cdot\vec{v} = 0 \end{cases} \tag{2}$$

with density ρ, velocity $\vec{v}$, pressure p, viscosity η, and an external force $\vec{f}$.

In practice, it was assumed that no external force was applied on the model (thus neglecting gravity) and the force $\vec{f}$ was set to zero.

The PDE problem (2) was solved using the PARallel sparse DIrect linear SOlver (PARDISO). For the time-dependent models, the CFD models were solved over several cardiac cycles to allow for stabilization. The 3D MR flow measurements were used for initialization as well. When the exact MR velocities (with some measurement errors) were used as boundary conditions, a stabilization algorithm (isotropic or anisotropic diffusion) was used.

CFD was performed using a commercial finite element solver (Comsol Multiphysics v3.4, Comsol Inc., Burlington, MA, USA, www.comsol.com). Blood was assumed to be incompressible with a density of 1,050 kg/m^3 and a dynamic viscosity of 0.0045 Pa s [9]. Newtonian approximation is supposed to be acceptable in large arteries where relatively high shear rates occur [4, 10].

2.2.3 CFD Models

Tube Model

The experimental model of stationary laminar flow in a straight rigid tube was used as a validation model. The mesh elements for this model were defined on the subdomain and it was solved using an adaptive mesh refinement technique resulting in 163×10^3 subdomain elements.

Descending Aorta Model

In this model, only a small part of the descending aorta of the volunteer was reconstructed and meshed for CFD (see Fig. 3a). The exact 4D flow dataset was used for the boundary condition at the inflow and a zero pressure reference (and no viscous stress) was defined at the outflow. The mesh elements for this model were defined on the subdomain only and it was solved over four cardiac cycles.

Thoracic Aorta Model

In this model, the complete thoracic aorta of the volunteer was reconstructed and meshed. This model was originally designed to produce an experimental model by rapid prototyping and hence presented nonphysiologic connection systems at its inlet/outlets (e.g., the left common carotid and the left subclavian artery were merged together). Due to the processing for rapid prototyping, this model was realized from a contrast-enhanced angiography dataset. This model used paraboloids scaled to the instantaneous flow of the flow-sensitive MRI data for the boundary conditions. Considering the rigid wall and the incompressibility assumptions, the net flow balance of the model was adjusted to be zero at every instant. The shape of the time-curve at the inflow was used for all inlet/outlets but the amplitude of every inlet/outlet was scaled to the measured flow volumes. In addition, the measured flow volumes at the outlets were slightly corrected in order to exactly match the flow volume at the inlet. This model was meshed with a very fine mesh over the subdomain and on boundary layers (242×10^3 elements, 1.9×10^6 degrees of freedom). This model was first solved as if it was stationary during mid-diastole (where the flow fluctuations over time are the smallest) and then the pseudo-stationary solution was used as initialization for the time-resolved solver (solved over five cardiac cycles).

3 Results

3.1 Tube Model

The velocity in the tube model simulated using CFD and measured using flow-sensitive MRI are shown in Fig. 4a. While the velocities measured using flow-sensitive MRI were generally noisy, the velocities based on CFD were very regular and presented parabolic-like shapes. It is visible that the velocities from flow-sensitive MRI were used for the boundary condition for the inflow of the CFD model as the CFD inlet appears noisy and irregular. However, those fluctuations were not propagated through the CFD simulation and the velocity field rapidly changed into a parabolic shape with increasing distance from the inflow. Despite the fluctuations in the flow-sensitive MRI velocity field, the overall correlation between CFD and flow-sensitive MRI were good. The flow-sensitive MRI velocities

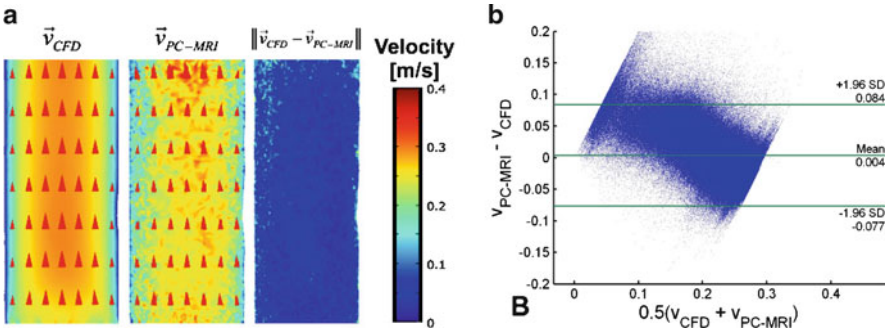

Fig. 4 (**a**) Flow velocities in the tube model calculated by CFD ($\vec{v}_{\mathrm{CFD}}$) and measured using flow-sensitive MRI ($\vec{v}_{\mathrm{PC-MRI}}$). The magnitude of the velocities and velocity difference $|\vec{v}_{\mathrm{CFD}} - \vec{v}_{\mathrm{PC-MRI}}|$ is given on the axial plane. In addition, the red arrowheads depict the local direction and amplitude of the velocities. (**b**) CFD vs. flow-sensitive MRI (PC-MRI) velocities in the tube model: Bland–Altman plot

demonstrated a near parabolic shape although zero-velocities could not be observed at the geometry edges. While the velocity was axially oriented for the CFD simulation, the direction of the velocity presented some fluctuations for the flow-sensitive MRI measurements.

A systematic voxel-wise analysis of the velocities between flow-sensitive MRI and CFD is shown in Fig. 4b with a Bland–Altman plot. It reveals a small average velocity difference of 0.004 m/s between flow-sensitive MRI and CFD, indicating thus that there was no systematic bias. This was expected considering that the flow-sensitive MRI data were used for the boundary condition. By looking at the distribution, it appears that low velocities were overestimated by flow-sensitive MRI while larger velocities were underestimated. This corresponds to the effects of a spatial low-pass filter and is thus consistent with what can be expected at limited resolution.

3.2 Descending Aorta Model

As shown in Fig. 5a, moderate spatial agreement was observed at peak systole between CFD and flow-sensitive MRI. The flow velocities computed from CFD were progressively regularized along the vessel from the inflow (top) to the outflow (bottom). At the outflow of the CFD model the velocity repartition seemed to be parabolic. In contrast, the velocities measured using flow-sensitive MRI presented a more irregular aspect with fluctuations throughout the model. In both cases, the velocities tended to increase toward the lower part of the aorta as the diameter is reduced.

The systematic voxel-wise analysis of the velocities between flow-sensitive MRI and CFD (Fig. 5b) was similar to the results found in the tube model (Fig. 4b). The Bland–Altman plot revealed again a small average velocity difference

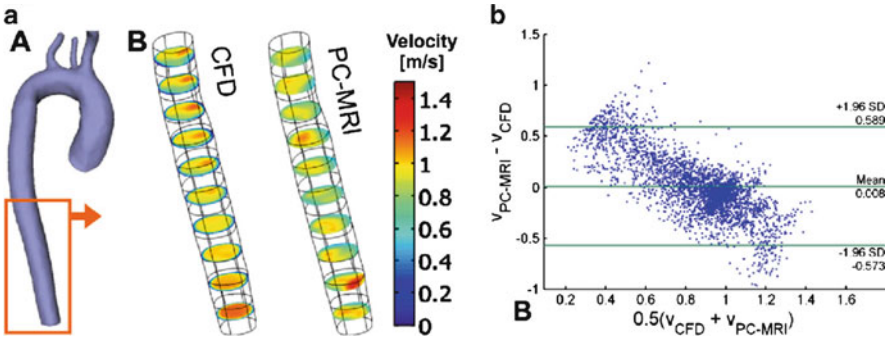

Fig. 5 (**a**) Systolic blood flow velocities in the descending aorta: CFD vs. flow-sensitive MRI. A: Section of the descending aorta geometry used in the model. B: Velocity calculated by CFD and measured using flow-sensitive MRI (PC-MRI) at ten transversal planes. The inflow (velocities from MRI taken for the boundary conditions for CFD) is at the top of the model while the outflow (open boundary for the boundary condition) is at the bottom. (**b**) CFD vs. flow-sensitive MRI (PC-MRI) velocities in the descending aorta model at peak systole: Bland–Altman plot

(0.008 m/s) validating that there was no systematic bias. The lower velocities were as well overestimated by flow-sensitive MRI while larger velocities were underestimated. Nevertheless, the differences were substantially larger for this model with a 95% confidence interval of [−0.573;0.589] m/s.

3.3 Thoracic Aorta Model

The flow–time curves for the thoracic aorta model are given in Fig. 6a. The time curve of plane 1 was taken for the boundary condition for the CFD and is thus identical for CFD and PCMRI. Considering that the CFD model assumes a non-compressible fluid and rigid walls, the relative shape of the flow-curve is the same for all planes of the CFD model. It only changes by a scaling factor that compensates for the flow to the supra-aortic arteries. The flow-curves for flow-sensitive MRI at planes 3, 6, and particularly 8, appeared delayed compared to the flow curve of CFD (and of previous planes). This effect is likely due to compliance (i.e., deformation due to elasticity of the arterial wall) in vivo which is expected to delay flow wave propagation.

The time-averaged WSS [11] and the oscillatory shear index (OSI, estimator of the temporal-variations of WSS) of the model are depicted in Fig. 6b. The distribution of time-averaged WSS revealed large WSS values in the right side of the ascending aorta as well as moderate WSS in the right side of the ascending aorta, in the aortic arch, and in the distal descending aorta. The contrast of WSS between the left and right side of the ascending aorta was particularly important. There were as well spatial fluctuations of WSS in the vicinity of the supra-aortic arteries. The proximal descending aorta presented relatively lower WSS. The OSI demonstrated a

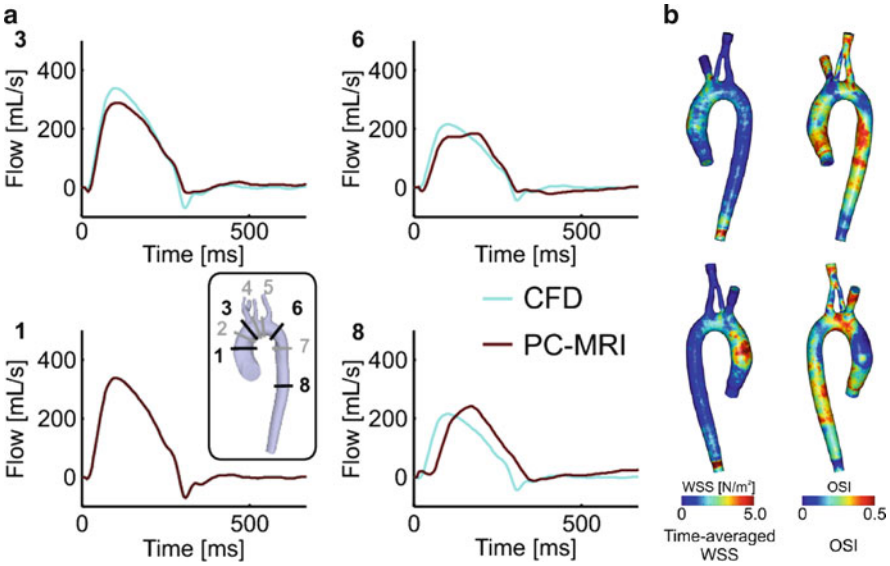

Fig. 6 (**a**) Blood flow in the thoracic aorta model derived from flow-sensitive MRI and CFD. Time resolved blood flow curves are given for the planes 1, 3, 6, and 8 as measured from flow-sensitive MRI (PC-MRI) and calculated using CFD. (**b**) CFD-based time-averaged Wall Shear Stress (WSS) and Oscillatory Shear Index (OSI, estimator of the temporal-variations of WSS) in the thoracic aorta model. Note that the connections at the inlet and outlets of the flow model have modified diameter compared to the original anatomy in vivo

sensibly different pattern with large values at the inflow of the ascending aorta and moderate levels in the aortic arch and proximal descending aorta. Those patterns presented yet substantial spatial fluctuations. Nevertheless, it seems that OSI was more important in the inner-curvature part of the aorta. The regions of highest OSI were observed at the base of the supra-aortic arteries and at the inner-curvature part of the proximal descending aorta. The distal descending aorta presented low levels of OSI. Interestingly, locations of high WSS often matched location of low OSI and locations of low WSS often matched locations of high OSI. It is somehow logical considering that low flow regions are more likely to be subject to retrograde flow as well. Nevertheless, the patterns of high OSI and low WSS at the base of the supra-aortic arteries as well as at the inner-part of the aortic arch and proximal descending aorta corresponded well to typical plaque locations [12–14]. With the exceptions of the particular hemodynamics at the inflow/outflow due to the connections, the measured WSS was about [0.5–1.5] N/m^2 throughout the aorta.

4 Discussion

The results of this study showed a direct comparison of 4D flow characteristics simulated by CFD and measured by flow-sensitive MRI in vivo based on an integration of both modalities into the same framework. This approach was motivated

by the complementarity of both approaches. On one hand, flow-sensitive MRI can directly measure hemodynamics in vivo but suffers from measurement errors and limited resolution. On the other hand, CFD can compute very accurate flow fields based on modeled arteries but depends on the validity of the hemodynamics models and boundary conditions.

Among the errors affecting flow-sensitive MRI, eddy currents, gradient field inhomogeneities, or concomitant gradients may be corrected or reduced. Nevertheless, even after these corrections, a certain level of error (e.g., the intrinsic measurement error) will still remain. In addition, the spatiotemporal resolution of MRI remains a limitation of 4D flow-sensitive MRI. CFD may introduce errors by using approximate models such as simplified boundary conditions, rigid and/or no-slip walls, or Newtonian rheology. Combination of 4D flow-sensitive MRI and CFD may be used to refine both methodologies and enhance the assessment of blood flow in vivo.

The integration of both modalities revealed a fair agreement between flow-sensitive MRI and MR-based CFD. Although some discrepancies could be observed, the overall qualitative agreement for flow velocities and directions between both modalities was good (Figs. 4a, 5a, and 6a). The systematic quantitative comparison of velocities based on CFD and flow-sensitive MRI (Figs. 4b, 5b, and 6a) revealed some slight discrepancies that could be explained by the different resolutions between the two modalities. In a study where both modalities were subsequently registered [15], such differences were not observed after artificially reducing the CFD resolution to match the MRI resolution. The partial volume effect (i.e., effect of limited spatial resolution) from MR measurements is likely to be one source of error of flow measurements using flow-sensitive MRI. However, some discrepancies in flow volume are likely to be due to geometry simplifications in the CFD model as well. Several small branches flowing out of the aorta were neglected in the flow models. In addition, errors in the flow–time curves (but not in the overall flow volume) may have been introduced in the CFD flow models by assuming the blood to be incompressible and the vessel walls to be rigid. While the incompressibility of blood is a reasonable and accepted simplification [16], assuming rigid vessel walls is likely to be a source of errors. Indeed, it is widely known that the blood vessels are changing their volume during the pulsatile pressure changes within the cardiac cycle. This effect, known as compliance, has an important role in the regulation of pulsatile blood flow in arteries and is responsible for delaying flow wave propagation (Fig. 6a). Furthermore, high Reynolds number can be present in the aorta and blood flow in vivo could be near to the onsets of turbulence [17] that would affect CFD calculations. Nevertheless, in the tube model in vitro (Fig. 4), where the CFD assumptions matched the reality (e.g., rigid wall), CFD was effective at removing the errors from the flow-sensitive MRI velocity field.

While flow-sensitive MRI data consists in the velocity information on a grid, the CFD model includes the velocity information in a much finer mesh and with a second order model. In addition, the CFD model contains information on the pressure and can be used to accurately derive parameters such as the viscous shear stress on the boundaries (when using very small boundary layer mesh). The shear stress at the

wall (WSS) and its oscillations (OSI) could be calculated using CFD and revealed patterns of pro-atherosclerotic low and oscillating WSS at the base of the supra-aortic arteries and at the inner-curvature of the aortic arch and proximal descending aorta (Fig. 6b) that coincided with the typical location of plaque in the thoracic aorta [12–14].

5 Conclusion

A methodology combining 4D flow-sensitive MRI and CFD into a single framework was presented. While numerous studies have presented CFD simulations based on realistic boundary conditions from CT and/or flow-sensitive MRI, the novel combination of both methodologies in three dimensions and over time opens up new opportunities for cross-validation and refinement of CFD models with MR measurements. Results in vitro and in vivo demonstrated the feasibility of this approach and showed the potential of the MR-based CFD approach to correct MR flow velocities and to provide detailed secondary flow parameters such as WSS.

The combination of flow-sensitive MRI and CFD in a single framework could be further used to refine the CFD models. Parameters such as viscosity, density, or vessel wall elasticity could potentially be optimized by comparing the CFD velocity field with the velocity field measured using MRI.

References

1. A. F. Stalder (2009) Quantitative analysis of blood flow and vessel wall parameters using 4D flow-sensitive MRI. PhD Thesis, University Freiburg
2. M. A. Castro, C. M. Putman, M. J. Sheridan, and J. R. Cebral (2009) Hemodynamic Patterns of Anterior Communicating Artery Aneurysms: A Possible Association with Rupture. AJNR Am J Neuroradiol
3. P. Papathanasopoulou, S. Zhao, U. Kohler, M. B. Robertson, Q. Long, P. Hoskins, X. Y. Xu, and I. Marshall (2003) MRI measurement of time-resolved wall shear stress vectors in a carotid bifurcation model, and comparison with CFD predictions. J Magn Reson Imaging 17:153–62
4. K. Perktold, R. O. Peter, M. Resch, and G. Langs (1991) Pulsatile non-Newtonian blood flow in three-dimensional carotid bifurcation models: a numerical study of flow phenomena under different bifurcation angles. J Biomed Eng 13:507–15
5. J. Bock, A. Frydrychowicz, A. F. Stalder, T. A. Bley, H. Burkhardt, J. Hennig, and M. Markl (2010) 4D phase contrast MRI at 3 T: effect of standard and blood-pool contrast agents on SNR, PC-MRA, and blood flow visualization. Magn Reson Med 63:330–8
6. P. A. Yushkevich, J. Piven, H. C. Hazlett, R. G. Smith, S. Ho, J. C. Gee, and G. Gerig (2006) User-guided 3D active contour segmentation of anatomical structures: significantly improved efficiency and reliability. Neuroimage 31:1116–28
7. D. Hazer, O. Bondarenko, R. Kroeger, R. Dillmann, and G. M. Richter (2007) Grid analysis for mesh-independent and stable CFD simulations in the aorta. In Proc. Curac, Karlsruhe, Germany
8. S. Prakash and C. R. Ethier (2001) Requirements for mesh resolution in 3D computational hemodynamics. J Biomech Eng 123:134–44

9. A. Gnasso, C. Carallo, C. Irace, V. Spagnuolo, G. De Novara, P. L. Mattioli, and A. Pujia (1996) Association between intima-media thickness and wall shear stress in common carotid arteries in healthy male subjects. Circulation 94:3257–62
10. D. A. Steinman (2004) Image-based computational fluid dynamics: a new paradigm for monitoring hemodynamics and atherosclerosis. Curr Drug Targets Cardiovasc Haematol Disord 4:183–97
11. A. F. Stalder, M. F. Russe, A. Frydrychowicz, J. Bock, J. Hennig, and M. Markl (2008) Quantitative 2D and 3D Phase Contrast MRI: Optimized Analysis of Blood Flow and Vessel Wall Parameters. Magn Reson Med 60:1218–1231
12. P. Tanganelli, G. Bianciardi, C. Simoes, V. Attino, B. Tarabochia, and G. Weber (1993) Distribution of lipid and raised lesions in aortas of young people of different geographic origins (WHO-ISFC PBDAY Study). World Health Organization-International Society and Federation of Cardiology. Pathobiological Determinants of Atherosclerosis in Youth. Arterioscler Thromb 13:1700–10
13. J. van der Linden, P. Bergman, and L. Hadjinikolaou (2007) The topography of aortic atherosclerosis enhances its precision as a predictor of stroke. Ann Thorac Surg 83:2087–92
14. J. J. Wentzel, R. Corti, Z. A. Fayad, P. Wisdom, F. Macaluso, M. O. Winkelman, V. Fuster, and J. J. Badimon (2005) Does shear stress modulate both plaque progression and regression in the thoracic aorta? Human study using serial magnetic resonance imaging. J Am Coll Cardiol 45:846–54
15. L. Boussel, V. Rayz, A. Martin, G. Acevedo-Bolton, M. T. Lawton, R. Higashida, W. S. Smith, W. L. Young, and D. Saloner (2009) Phase-contrast magnetic resonance imaging measurements in intracranial aneurysms in vivo of flow patterns, velocity fields, and wall shear stress: Comparison with computational fluid dynamics. Magn Reson Med 61:409–417
16. A. Quarteroni, M. Tuveri, and A. Veneziani (2000) Computational vascular fluid dynamics: problems, models and methods. Comput Visual Sci 2:163–197
17. A. F. Stalder, A. Frydrychowicz, M. F. Russe, J. G. Korvink, J. Hennig, and M. Markl (2009) Blood flow in the healthy aorta: turbulent or not? In Proc. 17th Scientific Meeting, International Society for Magnetic Resonance in Medicine, Hawaii, p. 3851

The Effects of Young's Modulus on Predicting Prostate Deformation for MRI-Guided Interventions

Stephen McAnearney, Andriy Fedorov, Grand R. Joldes, Nobuhiko Hata, Clare Tempany, Karol Miller, and Adam Wittek

Abstract Accuracy of image-guided prostate interventions can be improved by warping (i.e., nonrigid registration) of high-quality multimodal preoperative magnetic resonance images to the intraoperative prostate geometry. Patient-specific biomechanical models have been applied in several studies when predicting the prostate intraoperative deformations for such warping. Obtaining exact patient-specific information about the stress parameter (e.g., Young's modulus) of the prostate peripheral zone (PZ) and central gland (CG) for such models remains an unsolved problem. In this study, we investigated the effects of ratio of Young's modulus of the central gland E_{CG} to the peripheral zone E_{PZ} when predicting the prostate intraoperative deformation for ten cases of prostate brachytherapy. The patient-specific prostate models were implemented by means of the specialized nonlinear finite element procedures that utilize total Lagrangian formulation and explicit integration in time domain. The loading was defined by prescribing deformations on the prostate outer surface. The neo-Hookean hyperelastic constitutive model was applied to simulate the PZ and CG mechanical responses. The PZ to CG Young's modulus ratio E_{CG}:E_{PZ} was varied between 1:1 (upper bound of the literature data) and 1:40 (lower bound of the literature data). The study indicates that the predicted prostate intraoperative deformations and results of the prostate MRIs nonrigid registration obtained using the predicted deformations depend very weakly on the E_{CG}:E_{PZ} ratio.

Keywords Young's modulus · Prostate · Deformation · Non-linear · Finite element · Patient specific

S. McAnearney (✉)
Intelligent Systems for Medicine Laboratory, School of Mechanical and Chemical Engineering, The University of Western Australia, 35 Stirling Highway, 6009 Crawley/Perth, WA, Australia
e-mail: s.mcanearney@gmail.com

A. Wittek et al. (eds.), *Computational Biomechanics for Medicine: Soft Tissues and the Musculoskeletal System*, DOI 10.1007/978-1-4419-9619-0_5,

1 Introduction

Magnetic resonance imaging (MRI) provides unique and versatile capabilities in visualizing the normal structures of the prostate and in localizing the disease [1]. MRI can therefore be valuable in aiding image-guided prostate interventions, e.g., image-guided biopsy, brachytherapy, or prostatectomy. The procedure planning is typically done using high-quality preprocedural MRI obtained using different imaging techniques. However, during the therapy, the prostate deforms as a result of intervention, imaging protocols, and changes to the patient's position [2]. Consequently, the clinical target volume, such as tumor and critical healthy areas, determined from the preoperative MRIs needs to be updated to the new position/shape in the intraoperative images. This is typically done by warping (i.e., nonrigid registration, as in [3, 4]) of the pre-operative images to the intraoperative prostate geometry, which requires information about the prostate intraoperative deformations. A very promising solution for obtaining such information is predicting the intraoperative prostate deformations using models that rely on the principles of continuum mechanics [5]. Such models [3–7] are typically implemented using the finite element method that makes it possible to accurately represent the organs' geometry and has been extremely successful in various engineering applications [8].

Obtaining the patient-specific information about the prostate tissues constitutive properties (such as, e.g., Young's modulus and other stress parameters) remains an unsolved problem. Therefore, the effects of uncertainties in determining such properties on the results of nonrigid registration using the deformations predicted by means of biomechanical models have been investigated in several studies. For instance, Zhang et al. [9] found that the Young's modulus (E) significantly affects the accuracy of the model, while the Poisson's ratio does not. On the other hand, Wittek et al. [10] indicated that prediction of brain deformation due to craniotomy-induced brain shift very weakly depends on the tissue constitutive model when the appropriate nonlinear (i.e., taking into account finite deformations) formulation of continuum mechanics is used and the loading is defined by prescribing the deformation on the boundary. This finding forms the basis for the present investigation in which we analyze the effects of the ratio of prostate central gland and peripheral zone Young's modulus when predicting the prostate deformations due to brachytherapy.

2 Methods

2.1 Patients and Image Acquisition

Ten retrospective image sets of patients who received MR-guided brachytherapy were provided by the Department of Radiology, Brigham and Women's Hospital (Harvard Medical School, Boston, MA, USA). The patient entry requirements for

this therapy have been previously described in [11]. The patients were chosen as per the policy described in [11], which include only those with American Joint Commission on Cancer clinical stage T1cNXM0 prostate cancer.

A detailed description of the preoperative and intraoperative imaging protocols used in image acquisition is given in [3]. Relevant details to this investigation are as follows. Preoperative images were acquired using 1.5T MR-imaging (Signa LX, GE Medical Systems, Milwaukee, WI) with patient in supine position with endorectal coil fitted (4–6 cm in diameter). The preoperative image voxel size was $0.469 \times 0.469 \times 3$ mm.

The intraoperative images were acquired using 0.5T MR-imaging (Signa SP, GE Medical Systems, Milwaukee, WI) with the patient in the lithotomy position, with the rectal obturator (diameter 2 cm) used to fix the perineal template in place. The intraoperative voxel size was $0.938 \times 0.938 \times 5$ mm.

For further analysis and contrasting of computational grids for biomechanical models, the central gland and peripheral zone of the prostate were traced manually by two independent operators at Brigham and Women's Hospital (Harvard Medical School, Boston, MA, USA). Analysis of inter- and intraoperator variability has been performed, with no significant differences identified [3]. A representative example (case 1) is provided in Fig. 1. The segmentation was done using 3D Slicer [12], a surgical simulation and navigation tool.

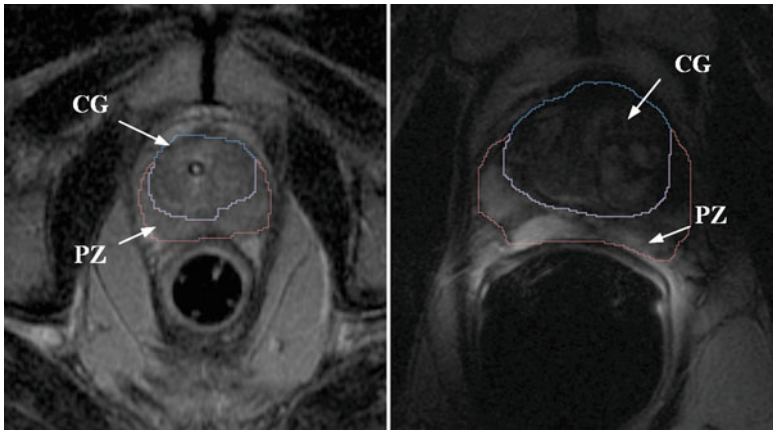

Fig. 1 Segmented preoperative (*right*) and intraoperative (*left*) images showing prostate substructures, central gland (CG), peripheral zone (PZ). Physical prostate deformation is influenced by the presence of the imaging coil (preoperative) or obturator (intraoperative), bladder filling, and patient position among other factors [2]

2.2 Biomechanical Modeling

2.2.1 Problem Formulation and Finite Element Algorithms Used

Following [9], the image registration was treated as a "displacement-zero-problem" (for definition see [13]) in which the loading is prescribed by the deformation of the boundary. In this study, the boundary deformation was defined by prescribing the displacements at every node of the prostate models outer surfaces. These displacements were determined from the triangulated (i.e., discretized using triangles) surfaces recovered from the manually traced contours of the total prostate gland, see Fig. 1. We used the conformal mapping approach by Haker et al. [4] to recover the surface displacements. In this method, the triangulated surfaces defining the pre- and intraoperative organ boundary are mapped to a unit sphere and retriangulated in a consistent manner, which results in point correspondence. Given such correspondence, the two surfaces are aligned affinely, so that the sum of the squared distances between the corresponding points is minimized, and the residual displacements are then used to initialize the surface displacements for modeling 3D deformations. The accuracy of this method was examined visually and determined acceptable for these cases. The aim of this study was to investigate the effect of varying Young's modulus under the same initial conditions. This comparison is made possible as the same registration procedure is used for each value of Young's modulus. Although important, the evaluation of the absolute accuracy of the surface matching and registration processes is outside the scope of this chapter. The distributions of surface displacement magnitudes for each case are summarized in Fig. 2.

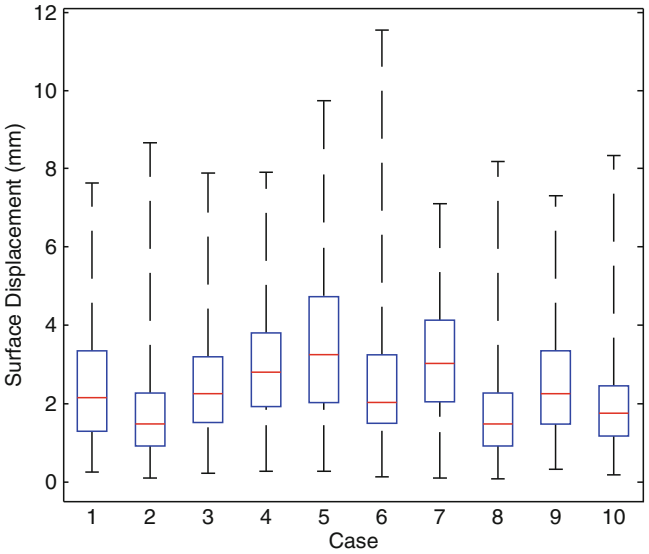

Fig. 2 Surface displacement magnitudes (mm) for the retrospective cases examined. The "whiskers" represent the maximum and minimum surface displacement values for each case

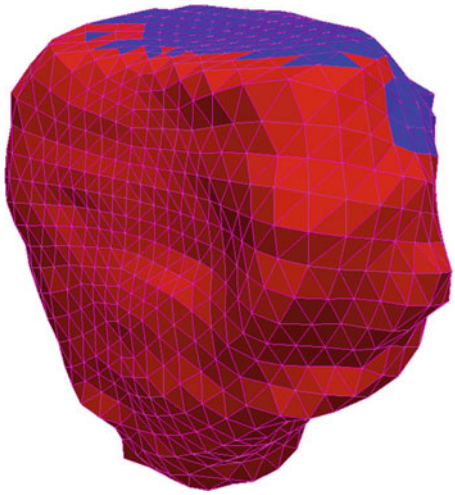

Fig. 3 Example of the prostate finite element mesh used in this study (Case 2. *Red*: PZ, *Blue*: CG)

For numerical integration of the equations of continuum mechanics, we used a suite of nonlinear finite element algorithms developed by Joldes et al. [14, 15] previously validated for brain shift computation [15,16]. The algorithms utilize total Lagrange formulation for stress update [17] and dynamic relaxation combined with explicit integration in time domain for steady-state computation. As indicated in [16] the algorithms by Joldes et al. [14, 15] facilitate computations within the real-time constraints of image-guided surgery on a standard personal computer.

2.2.2 Computational Grids (Finite Element Meshes)

The tetrahedral finite element meshes for the analyzed geometries were constructed as part of the procedure used for recovering the surface displacements, as described in [4]. The unit sphere that we used to establish correspondence between the surface points was meshed with tetrahedra. The inverse mapping of the geometry to this sphere allows warping the unit sphere mesh to each of the geometries. The mesh regions of CG and PZ were assigned based on the location of the tetrahedra with respect to the CG/PZ tracings. 13,744 tetrahedrons and 2,858 nodes were used in each mesh (see Fig. 3).

To prevent volumetric locking, the average nodal formulation as implemented by Joldes et al. [18] was used for tetrahedral elements.

2.3 Investigation of the Effects of Young's Modulus

A very wide range of Young's modulus E values has been reported in the literature for both normal and "cancerous" prostatic tissue. It has been hypothesized that

Table 1 Summary of the literature data of prostate Young's modulus E

Study	Method	Prostate tissue type	Young's modulus E (kPa)
Zhang et al. [19]	Unconstrained stress-relaxation tests on 8 mm samples. Eight samples. In vitro.	PZ healthy	15.9 ± 5.9
	Unconstrained stress-relaxation tests on 8 mm samples. Nine samples. In vitro.	PZ cancerous	40.4 ± 15.7
	Crawling wave sonoelastography. One sample. In vitro.	PZ healthy	19.2
	Crawling wave sonoelastography. One sample. In vitro.	PZ cancerous	62.9
Phipps et al. [20]	Mechanical cyclic probing using electromechanical shaker. Four samples. In vitro.	TG cancerous (treated)	118 ± 50
	Mechanical cyclic probing using electromechanical shaker. five samples. In vitro.	TG cancerous (untreated)	110 ± 2
Kemper et al. [21]	Dynamic sinusoidal elastography (7 samples). In vivo.	CG healthy	2.2 ± 0.3
	Dynamic sinusoidal elastography (7 samples). In vivo.	PZ healthy	3.3 ± 0.5
Krouskop et al. [22]	Mechanical testing at differing strain rates. 32 samples. In vitro.	CG healthy	63 ± 18
	Mechanical testing at differing strain rates. 32 samples. In vitro.	PZ healthy	70 ± 14
	Mechanical testing at differing strain rates. 21 samples. In vitro.	PZ cancerous	221 ± 32
	Mechanical testing at differing strain rates. 28 samples. In vitro.	PZ benign prostatic hyperplasia	36 ± 11
Yang et al. [23]	Macro- and micromechanical testing using electromechanical shaker. Six samples. In vitro.	PZ benign prostatic hyperplasia	200

this variation is to large extent due to differences in measurement techniques and experimental conditions between various studies [19]. A summary of the Young's modulus values for the total gland (TG), central gland (CG), and peripheral zone (PZ) available in the literature is given in Table 1. The table covers both the "healthy" and "cancerous" prostatic tissue.

It is seen from Table 1, that the cancerous prostatic tissue is "stiffer" (i.e., is characterized by larger Young's modulus) than the healthy tissue. This is consistent with the data for prostate by Kemper et al. [21] and breast cancer determined by Sinkus et al. [24].

When determining the ratio of Young's modulus of the PZ and CG for the present investigation, we used the information reported in [25] that 70% of prostate cancers occur in the PZ. We therefore increased the Young's modulus of the peripheral zone E_{PZ} while keeping the Young's modulus of the central gland constant at $E_{CG} = 5$ kPa (approximate lower bound for E_{CG} from Table 1). $E_{CG} = 5$ kPa was used rather than the actual lower bound of 2.2 kPa to facilitate investigation of the E_{CG}:E_{PZ} ratio. From Table 1, the highest value of cancerous E_{PZ} was found to be 221 kPa. Thus, to investigate the "worst case" scenario, the ratio E_{CG}:E_{PZ} was increased from 1:1 (homogeneous prostate) to 1:40 which yields (for $E_{PZ} = 200$ kPa), E_{CG}:E_{PZ} = 5:200 kPa. Ratio of 1:40 should be interpreted as an extreme one. For instance, Sinkus et al. [24] reported the average ratio of Young's modulus of healthy and cancerous (for breast cancer) tissue of around 1:2.

We use two measures to assess the impact of changing the Young's modulus. First, we consider the magnitude of the difference vector between the mesh vertex displacements obtained using 1:1 ratio and the displacements obtained using the studied ratio. Second, we calculate the dice similarity coefficient (DSC) [26] for the CG and PZ between the registered and intraoperative images which is a measure of overlap between these structures in pre- and intraoperative images. DSC is one of the metrics that is commonly used in the assessment of the registration quality.

3 Results

Changing the E_{CG}:E_{PZ} ratio from 1:1 to 1:40 resulted in up to 4.5 mm difference in nodal displacement, which is within the voxel size ($0.938 \times 0.938 \times 5$ mm^3) of the intraoperative images used in this study (Table 2). It should be noted, however, that in majority of the nodes this difference was much smaller as indicated by the median difference of up to only 0.4 mm.

A very clear pattern of the spatial distribution of differences in the calculated nodal displacements due to varying of ratio was observed: the largest differences were at the interface between the PG and CG, as seen in Fig. 4.

The results obtained when comparing the registered (using the deformations predicted by means of the finite element prostate models) segmented pre-operative images with the intraoperative ones are consistent with those obtained for the nodal displacements. Varying the E_{CG}:E_{PZ} ratio exerted a very weak effect on the DSC

Table 2 Displacement difference (mm) when changing the E_{CG}:E_{PZ} ratio from 1:1 to 1:40

Patient	Mean (mm)	Minimum (mm)	Maximum (mm)	Median (mm)	1st Quartile (mm)	3rd Quartile (mm)
1	0.54	0	3.32	0.42	0	0.83
2	0.28	0	2.41	0.21	0	0.45
3	0.38	0	2.94	0.28	0	0.65
4	0.42	0	2.71	0.31	0	0.71
5	0.56	0	3.97	0.32	0	0.94
6	0.43	0	4.05	0.31	0	0.64
7	0.75	0	4.56	0.56	0	1.23
8	0.19	0	2.44	0.07	0	0.29
9	0.33	0	2.38	0.27	0	0.55
10	0.28	0	1.92	0.23	0	0.44

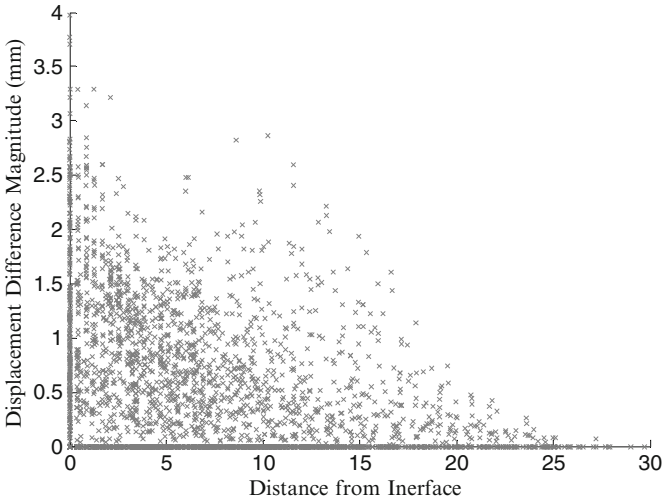

Fig. 4 Relationship between nodal displacement difference when changing the E_{CG}:E_{PZ} ratio from 1:1 to 1:40 and the node distance from the CG–PZ interface

for these two sets of images. The DSC appears to decrease as the ratio is decreased, which corresponds to reduced quality of the registration. We did not find statistically significant differences (CG: $p = 0.125$ and PZ: $p = 0.0625$ at 0.05 significance level) between the DSC values for 1:1 and 1:40 ratios with the paired Wilcoxon's signed rank test.

4 Discussion

The results indicate that the predicted prostate intraoperative deformations very weakly depend on the ratio of Young's modulus of the peripheral zone and central gland. Despite increasing this ratio from 1:1 to the extremely small value of 1:40

Table 3 DSC values for CG for the segmented intraoperative and registered preoperative images

	Case 01	Case 02	Case 03	Case 04	Case 05	Mean
E_{CG}:E_{PZ} = 1:1	0.828	0.881	0.892	0.720	0.753	0.815
E_{CG}:E_{PZ} = 1:5	0.818	0.882	0.884	0.710	0.746	0.808
E_{CG}:E_{PZ} = 1:40	0.813	0.882	0.880	0.705	0.741	0.804

Table 4 DSC values of PZ for the segmented intraoperative and registered preoperative images

	Case 01	Case 02	Case 03	Case 04	Case 05	Mean
E_{CG}:E_{PZ} = 1:1	0.685	0.827	0.770	0.687	0.685	0.731
E_{CG}:E_{PZ} = 1:5	0.666	0.826	0.757	0.674	0.673	0.719
E_{CG}:E_{PZ} = 1:40	0.656	0.825	0.751	0.668	0.665	0.713

(which implies that the Young's modulus of the cancerous tissue is 40 times larger than that of the healthy prostate), the maximum differences in the calculated nodal displacements was within the voxel size of prostate intraoperative MRIs (Table 2). The effects on the actual image registration, as measured by the Dice coefficient for the registered (using the predicted prostate deformations) and the actual intraoperative MRIs, were negligible for practical purposes (Tables 3 and 4).

The results obtained here indicate also that the spatial distribution of the effects of E_{CG}:E_{PZ} on the predicted deformation field within the prostate is nonuniform. The effects accumulate near the interface between the peripheral zone and central gland. Therefore, as tumors often occur near this interface, caution is required when formulating any clinical recommendations based on the results of this study.

The significance of our results for the clinical decision making requires additional investigation. One of the limitations of our study is the use of DSC as the measure of alignment, which does not allow studying the local error distribution. We observe that the distribution of the displacement difference at the fixed distance from the interface between the central gland and peripheral zone is not uniform. Since accurate targeting is critical for image-guided procedures, additional investigation is warranted to quantify the differences in the local region (e.g., suspected tumor site) near the interface.

In this study, following [15] and [10], prostate image registration was treated as a displacement-zero-traction problem of continuum mechanics, i.e., the loading was defined by prescribing deformations on the prostate boundary. It has been previously indicated that for such formulation, the predicted organ intraoperative deformations (and results of image registration obtained using the predicted deformations) very weakly depend on the tissue constitutive model. However, the conclusions derived from our results may not apply to situations when the loading is prescribed through natural boundary conditions (i.e., forces, pressure acting on the boundary).

Acknowledgments The financial support of the Australian Research Council (Grants DP0664534, DP1092893, DP0770275, DP1092893, and LX0774754) is gratefully acknowledged. Andriy fedorov, Nobuhiko Hata, and Clare Tempany were supported by NIH grants U41RR019703 and R01CA111288.

References

1. Afnan J, Tempany C (2010) Update on Prostate Imaging. Urol Clin North Am 37(1):23–25
2. Stijn W, Heijmink M, Tom W et al (2009) Changes in prostate shape and volume and their implications for radiotherapy after introduction of endorectal balloon as determined by MRI at 3T. Int J Radiation Oncology Biol Phys 73(5):1446–1453
3. Bharatha A, Hirose M, Hata N et al (2001) Evaluation of three-dimensional finite element-based deformable registration of pre- and intra-operative prostate imaging. Med Phys 28(12): 2551–2560
4. Haker S, Warfield S, Tempany C (2004) Landmark-guided surface matching and volumetric warping for improved prostate biopsy targeting and guidance. In: MICCAI 2004, LNCS 3216. Springer, Berlin
5. Crouch J, Pizer S, Chaney S et al (2003) Medially based meshing with finite element analysis of prostate deformation. In: MICCAI 2003, LNCS 2878. Springer, Berlin
6. Ferrant M, Warfield S, Guttmann C et al (1999) 3D image matching using a finite element based elastic deformation model. In: MICCAI'99: Proceedings of the second international conference on medical image computing and computer-assisted intervention. Springer, London
7. Hogea C, Abraham F, Biros, et al (2007) A robust framework for soft tissue simulations with application to modeling brain tumor mass-effect in 3D images. Phys Med Biol. 10.1088/0031-9155/52/23/008
8. Bathe K-J (1996) Finite element procedures. Prentice-Hall, Upper Saddle River
9. Zhang Y, Goldgof D, Sarkar S et al (2007) A sensitivity analysis method and its application in physics-based nonrigid motion modeling. Ima Vis Comput 25:262–273
10. Wittek A, Hawkins T, Miller K (2009) On the unimportance of constituitive models in computing brain deformation for image-guided surgery. Biomech Model Mechanobiol 8:77–84
11. D'Amico A, Cormack R, Tempany C et al (1998) Real-time magnetic resonance image-guided interstitial brachytherapy in the treatment of select patients with clinically localized prostate cancer. Int J Radiation Oncology Biol Phys 42(3):507–515
12. 3D Slicer, www.slicer.org
13. Miller K (2005) Method of testing very soft biological tissues in compression. J Biomech 38:153–158
14. Joldes GR, Wittek A, Miller K (2009) Suite of finite element algorithms for accurate computation of soft tissue deformation for surgical simulation. Med Image Anal doi:10.1016/j.media.2008.12.001
15. Joldes GR, Wittek A, Miller K (2009) Computation of intra-operative brain shift using dynamic relaxation. Comput Methods Appl Mech Engrg 198:3313–3320
16. Joldes GR, Wittek A, Mathieu C et al (2009) Real-time prediction of brain shift using nonlinear finite element algorithms. In: MICCAI 2009, LNCS 5762. Springer, Berlin
17. Miller K, Joldes GR, Lance D et al (2007) Total lagrangian explicit dynamics finite element algorithm for computing soft tissue deformation. Commun Numer Meth Engng 23:121–134
18. Joldes GR, Wittek A, Miller K (2008) Non-locking tetrahedral finite element for surgical simulation. Commun Numer Meth En 25(7):827–836
19. Zhang M, Nigwekar P, Castaneda B et al (2008) Quantitative characterization of viscoelastic properties of human prostate correlated with histology. Ultrasound in Med and Biol 34(7): 1033–1042
20. Phipps S, Yang T, Habib F et al (2005) Measurement of tissue mechanical characteristics to distinguish between benign and malignant prostate disease. J Urology 66:447–450

21. Kemper J, Sinkus R, Lorenzen J et al (2004) MR elastography of the prostate: initial in-vivo application. Fortschr Röntgenstr 176(8): 1094–1099
22. Krouskop T, Wheeler T, Kallel F et al (1998) Elastic moduli of breast and prostate tissue under compression. Ultrasonic Imaging 20:260–274
23. Yang T, Leung S, Phipps S et al (2006) In-vitro dynamic micro-probing and the mechanical properties of human prostate tissues. Technol Health Care 14:281–296
24. Sinkus R, Tanter M, Xydeas T (2005) Viscoelastic shear properties of in vivo breast lesions measured by MR elastography. Magn Reson Imaging (23):159–165
25. Tempany C, Straus S, Hata N et al (2008) MR-Guided prostate interventions. J Magn Reson Imaging 27:356–367
26. Dice L (1945) Measures of the amount of ecological association between species. Ecology 26:297–302

On the Effects of Model Complexity in Computing Brain Deformation for Image-Guided Neurosurgery

Jiajie Ma, Adam Wittek, Benjamin Zwick, Grand R. Joldes, Simon K. Warfield, and Karol Miller

Abstract Intra-operative images acquired during brain surgery do not provide sufficient detail to confidently locate brain internal structures that have been identified in high-resolution pre-operative images. However, the pre-operative images can be warped to the intra-operative position of brain using predicted deformation field. While craniotomy-induced brain shift deformation can be accurately computed using patient-specific finite element models in real-time, accurate segmentation and meshing of brain internal structures remains a time-consuming task. In this chapter, we conduct a parametric study to evaluate the sensitivity of the predicted brain shift deformation to model complexity, which includes the effects of disregarding the differences in properties between the parenchyma, tumour and ventricles and applying different approaches for representing the ventricles (as a very soft solid or cavity) to minimise segmentation and meshing effort for model generation. The results suggest that the difference in brain shift deformation predicted by models due to such variation is not significant. Segmentation of brain parenchyma and skull seems sufficient to build models that can accurately predict craniotomy-induced brain shift deformation.

Keywords Model complexity · Neuroimage segmentation · Non-linear finite element model · Brain shift deformation

1 Introduction

Intra-operative images that can be acquired during image-guided brain surgery do not provide sufficient contrast and resolution to confidently locate the abnormalities (such as tumour) and critical healthy regions [1]. This problem can be solved by warping the high-quality pre-operative images to the current (intra-operative)

J. Ma (✉)
Intelligent Systems for Medicine Laboratory, School of Mechanical and Chemical Engineering, The University of Western Australia, 35 Stirling Highway, 6009 Crawley/Perth, WA, Australia
e-mail: jiajie@civil.uwa.edu.au

A. Wittek et al. (eds.), *Computational Biomechanics for Medicine: Soft Tissues and the Musculoskeletal System*, DOI 10.1007/978-1-4419-9619-0_6,

position of the brain. Accurate alignment between the pre- and intra-operative anatomies requires taking into account the craniotomy-induced brain shift deformation, which implies non-rigid registration. Traditionally, non-rigid registration relies on image processing-based methods, such as optical flow [2,3], mutual information-based similarity [4], entropy based alignment [1] and block matching [3]. However, these methods do not take into account mechanical properties of the anatomical features depicted in the images and may result in non-physical deformation fields [5]. To ensure the plausibility of the predicted deformation field, biomechanical models are used to complement image-based methods. Patient-specific models implemented using nonlinear finite element procedures are used to predict the craniotomy-induced brain shift deformation [5–8]. As the craniotomy-induced brain surface deformation can exceed 20 mm [9], geometrical non-linearity should be included in the model for accurate prediction. The choice of brain tissue constitutive model, when used with an appropriate modelling approach, has negligible effect on the accuracy of computed brain deformation [8–10].

Recent developments in specialised nonlinear finite element algorithms and solvers enable real-time computation of soft organ deformation [11, 12]. For instance, such algorithms and solvers have been used by Joldes et al. [13] to accurately predict brain deformation in five cases of craniotomy-induced brain shift with a computation time of less than 4 s on a graphics processing unit.

Despite the progress in algorithm development, construction of patient-specific models, in particular segmentation and meshing of brain internal structures such as tumour and ventricles still poses a significant challenge. Commonly accepted tools for automatic segmentation of brain internal structures are not established yet. Meshing of the segmented brain internal structures such as tumour and ventricles using hexahedra elements (which are less expensive in terms of computation) is also a time-consuming task [13]. A straightforward approach for reducing the time required for segmentation and meshing would be to ignore the difference between brain internal structures such as tumour and ventricles, which have typically been included in craniotomy-induced brain shift models [5, 13].

In this chapter, using five patient-specific brain shift models developed and validated by Joldes et al. [13], we performed a parametric study to determine how the predicted brain shift deformation is affected by model complexity. As fast and reliable segmentation and meshing of tumour and ventricles present itself as a formidable challenge, we investigated the effects of excluding the tumour and ventricles from the model as well as simulating the ventricles as either a very soft solid or cavity.

The subsequent sections present the following topics: Sect. 2 describes the investigation of the effects of model complexity including the approaches for modelling and evaluation of the studied effects. Section 3 presents comparisons of the predicted brain shift deformation obtained using models with different complexity. The discussion and conclusions are given in Sect. 4.

2 Methods

2.1 Model Complexity

In this study, we use five patient-specific craniotomy-induced brain shift models originally developed and validated by Joldes et al. [13] as the starting point. These cases represent different situations that may occur in neurosurgery as characterised by tumours located in different parts of the brain: anteriorly (Cases 1 and 2), laterally (Case 3) and posteriorly (Cases 4 and 5) (see Fig. 1).

For each case, the model developed by Joldes et al. [13] (referred to as the complete model, *Model A*, see Fig. 2), consisting of the parenchyma, skull, tumour and ventricles is a geometrically accurate representation of the clinical case. The brain shift deformations predicted by these models were used as a reference point. To investigate the effects of model complexity, the complete models were simplified to create models of decreasing complexity as follows.

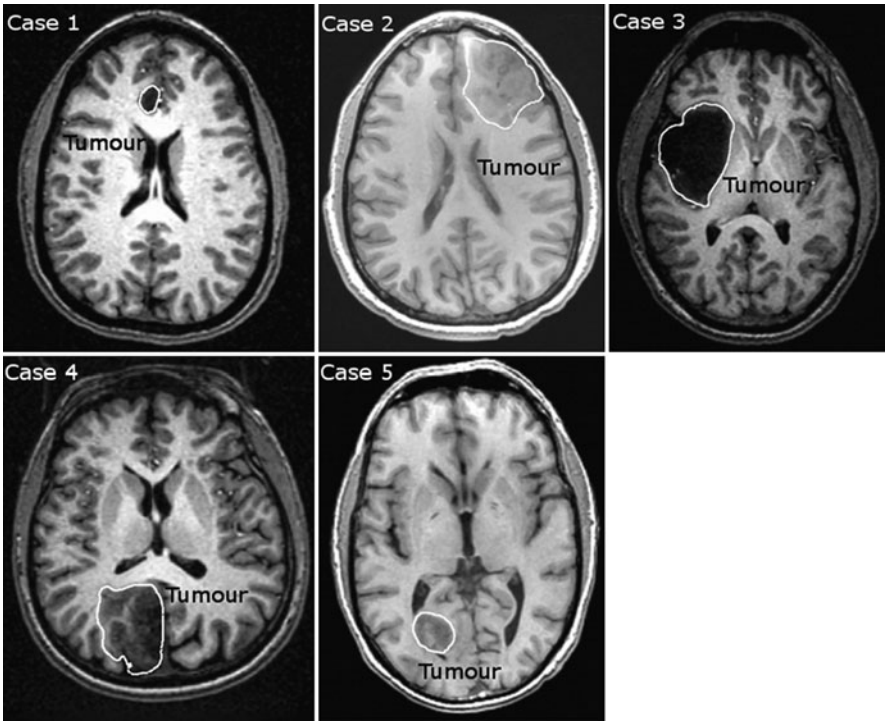

Fig. 1 Preoperative MRIs (inferior view) showing tumour location in the cases analysed in this study. Tumours are labelled and highlighted with a *white contour line*

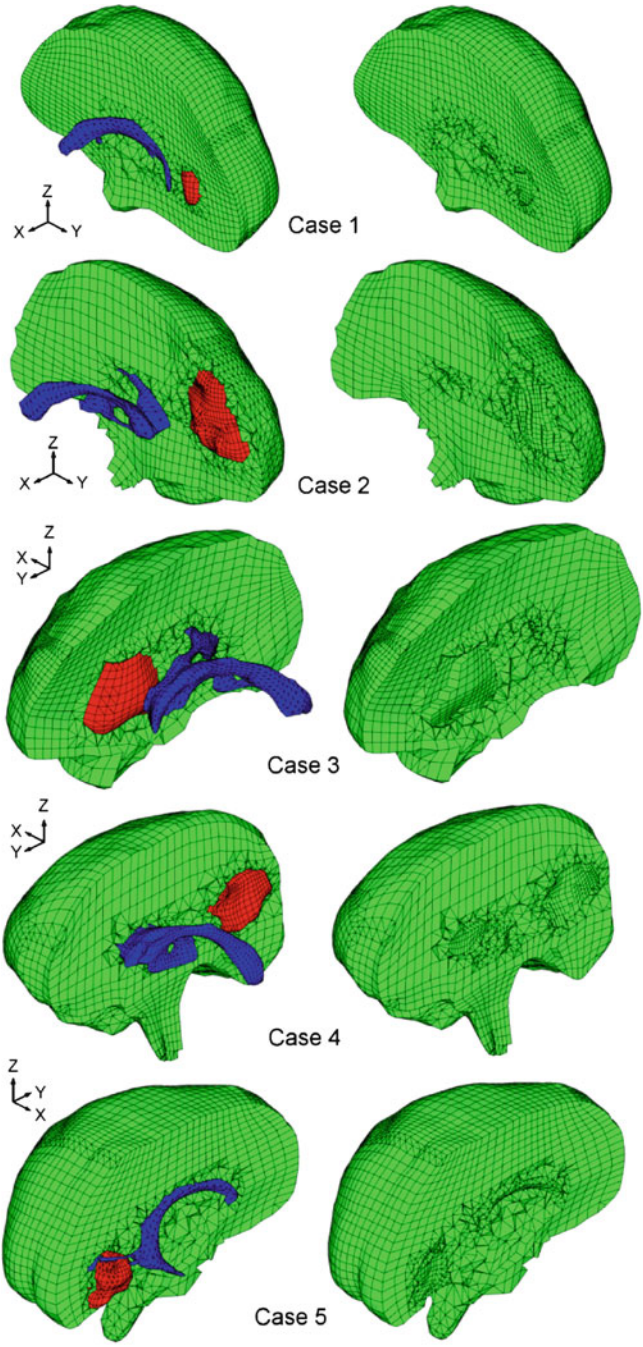

Fig. 2 The complete model (*A, left*) and homogeneous one (*D, right*) for the five cases of craniotomy induced brain shift analysed here. In the complete model, the parenchyma, tumour and ventricles were simulated. In the homogeneous model, the tumour and ventricles were included in the parenchyma

Model B. Simplified model consisting of the parenchyma, skull, and tumour. The ventricles were modelled as an empty cavity. This was realised by excluding the ventricle elements from the complete model (A). This simplification removes the need for conducting meshing of the ventricles.

Model C. Simplified model consisting of the parenchyma and skull. The tumour was excluded from the model and its volume was amalgamated with the parenchyma. The ventricles were modelled as an empty cavity. This simplification further removes the need to segment and mesh a tumour.

Model D. Homogenous model consisting of the parenchyma and skull. The tumour and ventricles were not modelled and were instead included in the parenchyma. This was realised by assigning parenchyma properties to tumour and ventricle elements. This simplification further removes the need to segment the ventricles. For this model, segmentation of the brain parenchyma and skull is sufficient (Fig. 2).

2.2 Boundary Conditions, Loading and Brain Tissue Constitutive Model

Following Joldes et al. [13], the craniotomy-induced brain shift model was loaded by prescribing nodal displacements to a set of nodes under the craniotomy determined from the segmented pre- and intra-operative cortical surfaces [14]. The maximum brain surface deformation varies from 4 mm (Case 1) to 7 mm (Case 2). The boundary conditions for the model were defined as a contact interface between the rigid skull and remaining nodes of the brain surface. This interface prevents the brain surface from penetrating the skull while allowing for frictionless sliding and separation between brain and skull.

Following Joldes et al. [13], the neo-Hookean hyperelastic constitutive model [15] was used for tumour and parenchyma, with a Young's modulus of 6,000 and 3,000 Pa and a Poisson's ratio of 0.49 for both. Following Wittek et al. [5], the ventricles were modelled as a very soft compressible elastic solid with Young's modulus of 10 Pa and Poisson's ratio of 0.1 to account for volume decrease due to fluid leakage.

The specialised nonlinear finite element solver developed by Joldes et al. [12, 16] and Miller et al. [11] for real-time computation of soft organ deformation was used to calculate the craniotomy-induced brain shift deformation.

2.3 Evaluation of the Effects of Model Complexity

We compare the intra-operative geometries of the tumour and ventricles obtained by registration of the pre-operative data using the deformation fields predicted by different models. Following Joldes et al. [13], the bounds of tumour and ventricles

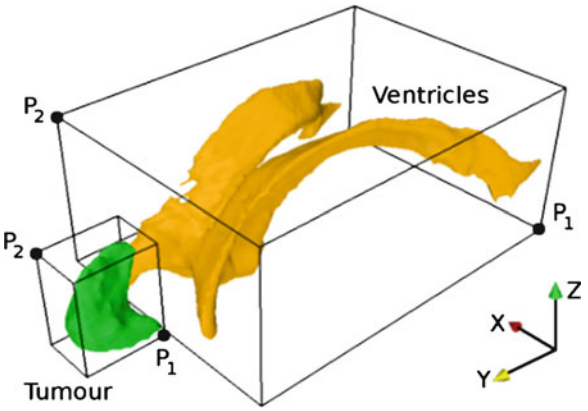

Fig. 3 The vertices P_1 and P_2 define a cuboidal box bounding the tumour or ventricles. The *X*, *Y*, *Z* coordinates of the vertices provide a quantitative measure of the predicted brain shift

Table 1 Differences in the *X*, *Y*, *Z* coordinates of vertices P_1 and P_2 defining the bounds of the tumour and ventricles (Fig. 3) between the complete model (*A*) and the simplified ones (*C*, *D*)

	Tumour						Ventricles					
	X		*Y*		*Z*		*X*		*Y*		*Z*	
Unit: mm	P_1	P_2	P_1	P_2	P_1	P_2	P_1	P_2	P_1	P_2	P_1	P_2
Model C: Tumour modelled as parenchyma, ventricles as a cavity												
Case 1	0.02	0.04	0.06	0.01	0.09	0.01	0.00	0.00	0.00	0.00	0.02	0.00
Case 2	0.09	0.02	0.23	**0.74**	**0.13**	0.12	0.01	0.02	0.00	**0.05**	**0.07**	0.02
Case 3	0.00	**0.14**	0.02	0.02	0.02	0.02	0.03	**0.04**	0.03	0.01	0.01	0.01
Case 4	0.00	0.00	0.00	0.04	0.03	0.03	0.01	0.00	0.02	0.01	0.02	0.00
Case 5	0.01	0.02	0.01	0.01	0.01	0.02	0.00	0.00	0.00	0.00	0.00	0.00
Model (*D*): Homogenous mesh, tumour and ventricles modelled as parenchyma												
Case 1	0.01	0.10	0.16	0.10	0.02	0.01	**0.16**	0.07	0.06	0.05	0.05	**0.14**
Case 2	0.09	0.01	0.25	**0.85**	**0.15**	0.09	0.02	0.02	0.01	**0.09**	0.12	0.06
Case 3	0.00	**0.14**	0.01	0.02	0.02	0.02	0.04	0.05	0.02	0.03	0.01	0.01
Case 4	0.00	0.00	0.00	0.04	0.03	0.03	0.01	0.01	0.01	0.01	0.02	0.00
Case 5	0.00	0.02	0.01	0.00	0.01	0.02	0.01	0.00	0.01	0.01	0.00	0.00

The numbers in bold indicate the maximum differences in the *X*, *Y*, and *Z* directions

are used to provide quantitative information about the shape and position of tumour and ventricles. The bounds can be interpreted as the *X*, *Y*, *Z* coordinates of vertices P_1 and P_2 defining cuboidal boxes bounding the tumour and ventricles (Fig. 3).

To provide a comparison of the brain shift deformation prediction from the finite element modelling perspective, nodal displacements of the nodes defining the tumour and ventricles are compared one-by-one, between the complete model (*A*) and Model (*D*) in which homogenous constitutive properties were used for the entire brain. The homogenous models (*D*) were selected here because the maximum differences in the tumour and ventricles bounds (Table 1) were observed between them and the complete models (*A*).

3 Results

The differences in X, Y, Z coordinates of the bounds of the tumour and ventricles (Fig. 3) between the complete model (A) and model (B) (i.e. the one with the ventricles simplified as an empty cavity) were not observable up to 0.01 mm. Given that the resolution of intra-operative MRIs used in this study was $0.86 \times 0.86 \times 2.5$ mm^3, these differences are relatively very small and their values are not reported here. The differences between the intra-operative bounds of ventricles and tumour predicted by the complete model (A) and the simplified ones (C, D) are listed in Table 1. The maximum differences were observed between the complete model (A) and the homogeneous one (D): 0.85 mm in the Y (anterior–posterior) direction for the tumour (Case 2) and 0.16 mm in the X (lateral) direction for the ventricles (Case 1). These differences are within the resolution of the intra-operative images ($0.86 \times 0.86 \times 2.5$ mm^3).

Table 2 lists the maximum and median differences in nodal displacement in the X, Y, Z directions (Fig. 3) for each case. Please note that the maximum differences in the X, Y, Z directions may not have been observed from the same node. For the tumour, the single largest difference (0.95 mm) and the highest median difference (0.26 mm) was observed in the Y (anterior–posterior) direction in Case 2. For the ventricles, the single largest difference (0.90 mm) and the highest median difference (0.15 mm) was observed in the Y (anterior-posterior) direction in Case 1. The maximum differences are close to the resolution ($0.86 \times 0.86 \times 2.5$ mm^3) of the intra-operative images used in this study.

The absolute resultant differences of nodal displacements predicted by models (A) and (D) for tumour and ventricles are shown in Fig. 4. The difference is indicated using a colour code. It is clear from Fig. 4 that for most of the nodes, the difference is well below the resolution ($0.86 \times 0.86 \times 2.5$ mm^3) of the intra-operative images used in this study.

To visualise the differences of the predicted brain shift deformation obtained using models with different complexity, the registered (deformed using the calculate

Table 2 Maximum and median differences in nodal displacements in X, Y, Z directions of nodes defining the tumour and ventricles between the complete model (A) and the homogenous one (D)

	Tumour						Ventricles					
	X		Y		Z		X		Y		Z	
Unit: mm	Max	Mdn	Max	Mdn	Max	Mdn	Max	Mdn	Max	Mdn	Max	Mdn
Model D: Homogenous model, tumour and ventricles modelled as parenchyma												
Case 1	0.16	0.05	0.40	0.17	0.18	0.05	0.50	0.12	**0.90**	**0.15**	0.56	0.15
Case 2	0.28	0.08	**0.95**	**0.26**	0.31	0.10	0.61	0.14	0.62	0.12	0.44	0.09
Case 3	0.24	0.06	0.17	0.04	0.15	0.02	0.12	0.04	0.07	0.02	0.07	0.01
Case 4	0.07	0.02	0.23	0.04	0.10	0.02	0.03	0.01	0.04	0.02	0.03	0.01
Case 5	0.04	0.01	0.04	0.01	0.03	0.01	0.05	0.01	0.03	0.01	0.04	0.00

The numbers in bold indicate single largest difference and highest median difference in tumour and ventricles

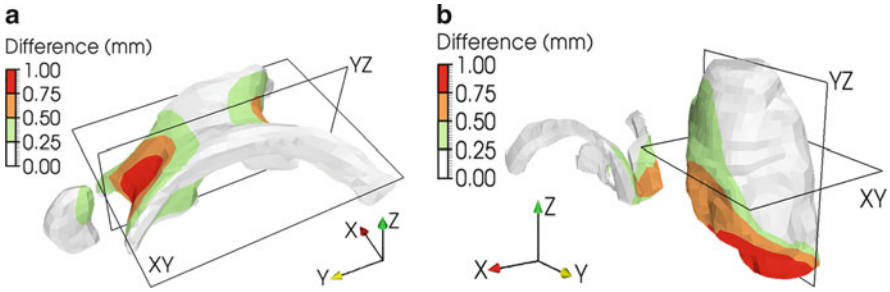

Fig. 4 The absolute resultant differences of nodal displacements predicted by model (*A*) and (*D*) in tumour and ventricles in (**a**) Case 1 and (**b**) Case 2. The difference is indicated by a *colour code*

brain deformation field) contours of ventricles and tumour predicted by the complete model (*A*) and homogenous one (*D*) are imposed on the intra-operative MR images for Cases 1 and 2 in Fig. 5. The MR images corresponding to the XY (transverse) and YZ (sagittal) planes (as shown in Fig. 4) were selected to visualise the maximum differences in nodal displacement predictions. The images are enlarged and cropped to highlight the area of interest. Figure 5 shows the contours overlap except for some minor misalignments.

4 Discussion and Conclusions

In this chapter, a parametric study was performed to investigate how the brain shift deformation prediction is affected by the difference in model complexity. Five cases of craniotomy-induced brain shift [13] were investigated. For each case, a complete model (*A*) consisting of parenchyma, skull, tumour and ventricles was used as the starting point. This model was simplified to create models of decreasing complexity (i.e. *B*, *C* and *D*, see Sect. 2.1). The craniotomy-induced brain shift deformation calculated using models with different complexity is compared in terms of the bounds indicating the intra-operative geometries of tumour and ventricles, and of nodal displacements on one-by-one basis.

The results of this study show that the difference in brain shift deformation prediction obtained using models with different complexity is not significant. The differences in the bounds of tumour and ventricles predicted using the complete model (*A*) and simplified ones (*B*, *C* and *D*) were negligible. They did not exceed 0.85 mm (Table 1), which is within the resolution ($0.86 \times 0.86 \times 2.5$ mm^3) of intra-operative MR images. Good agreement of brain shift deformation predictions obtained using models with different complexity is confirmed by the comparison of the nodal displacements. The maximum difference in nodal displacements predicted using the complete model (*A*) and the homogeneous one (*D*) is 0.95 mm (Table 2), which is very close to the resolution ($0.86 \times 0.86 \times 2.5$ mm^3) of intra-operative MR image. For most of the nodes, the difference is well below the resolution of the

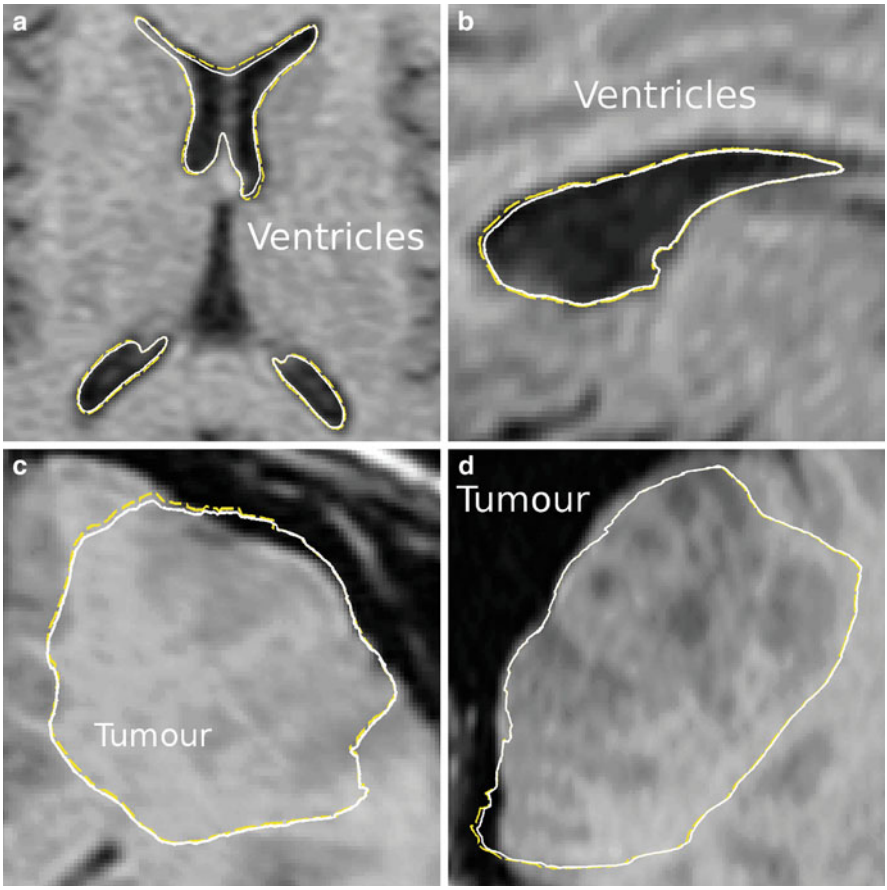

Fig. 5 The registered contours of ventricles in Case 1 and tumour in Case 2 predicted by the complete model (Model A, *continuous line*) and homogenous one (Model D, *dash line*) are imposed on the intra-operative MR images. The MR images corresponding to the XY and YZ planes in Case 1 and Case 2 were selected to show the maximum differences in nodal displacements. The images are enlarged and cropped to highlight the area of interest: (**a**) ventricles in Case 1 (XY plane), (**b**) ventricles in Case 1 (YZ plane), (**c**) tumour in Case 2 (XY plane), (**d**) tumour in Case 2 (YZ plane)

intra-operative images (Fig. 4). The contours of ventricles and tumour registered using the deformation fields predicted by the complete model (A) and the homogenous one (D) also suggests good agreement (Fig. 5).

From the results, it is clear that the predicted brain shift deformation is very weakly affected by the change in model complexity, with the largest difference observed between the complete model (A) and the homogenous one (D) in which homogenous material properties was used for the entire model. The magnitudes of the difference suggest that an exact modelling of tumour and ventricles is not needed to predict the brain shift deformation to an acceptable accuracy (within

the resolution of intra-operative images). This parametric study suggests that a segmentation of brain parenchyma alone seems to be sufficient to build models that can accurately predict craniotomy-induced brain shift deformation. As accurate segmentation and meshing of brain internal structures is the most time-consuming step when preparing patient-specific models, the amount of time, cost and expertise required for generating the patient-specific model can be greatly reduced.

It must be stated that these results are only valid for computation of craniotomy-induced brain shift using the modelling frameworks [5] developed for medical image registration in which the loading was defined through essential boundary conditions (i.e. prescribing cortical surface deformation) determined from intra-operative MR images. The conclusion may not apply to modelling frameworks in which the loading was defined through natural boundary conditions (e.g. loading by gravity force and/or pressure caused by interactions between the brain and cerebrospinal fluid).

Furthermore, the validity of this conclusion is confined as only five cases of craniotomy-induced brain shift were investigated. The difference induced by change of model complexity varies from case to case. The maximum difference occurs in Case 2 in which the maximum brain surface deformation (up to 7 mm) is observed. As the brain surface deformation due to craniotomy can exceed 20 mm [9], a study of more cases with larger displacements at the craniotomy site is required.

Acknowledgements The financial support of the Australian Research Council (Grants DP0664534, DP1092893, DP0770275 and LX0774754), National Institute of Health (Grants R03 EB008680, R01 RR021885 and R01 EB008015), CIMIT, and Australian Academy of Science is gratefully acknowledged. We thank Prof. Ron Kikinis of Harvard Medical School for very helpful suggestions.

References

1. Warfield, S.K., Haker, S.J., Talos, I.F., Kemper, C.A., Weisenfeld, N., Mewes, A.U.J., Goldberg-Zimring, D., Zou, K.H., Westin, C.F., Wells, W.M., Tempany, C.M.C., Golby, A., Black, P.M., Jolesz, F.A., Kikinis, R.: Capturing Intraoperative Deformations: Research Experience at Brigham and Women's Hospital. Medical Image Analysis 9, 145–162 (2005)
2. Beauchemin, S.S., Barron, J.L.: The computation of optical flow. ACM Computing Surveys 27, 433–467 (1995)
3. Dengler, J., Schmidt, M.: The dynamic pyramid-a model for motion analysis with controlled continuity. International Journal of Pattern Recognition and Artificial Intelligence 2, 275–286 (1988)
4. Viola, P., Wells III, W.M.: Alignment by maximization of mutual information. International Journal of Computer Vision 24, 137–154 (1997)
5. Wittek, A., Miller, K., Kikinis, R., Warfield, S.K.: Patient-Specific Model of Brain Deformation: Application to Medical Image Registration. Journal of Biomechanics 40, 919–929 (2007)
6. Joldes, G.R., Wittek, A., Miller, K.: Computation of intra-operative brain shift using dynamic relaxation. Computer Methods in Applied Mechanics and Engineering 198, 3313–3320 (2009)
7. Miller, K., Wittek, A., Horton, A., Dutta Roy, T., Berger, J. and Morriss, L. Modelling brain deformation for computer-integrated neurosurgery (invited review). International Journal for Numerical Methods in Biomedical Engineering 26(1), 117–138 (2010)

8. Wittek, A., Hawkins, T., Miller, K.: On the unimportance of constitutive models in computing brain deformation for image-guided surgery. Biomechanics and Modeling in Mechanobiology 8(1), 77–84 (2009)
9. Roberts, D.W., Hartov, A., Kennedy, F.E., Miga, M.I., Paulsen, K.D.: Intraoperative Brain Shift and Deformation: A Quantitative Analysis of Cortical displacement in 28 cases. Neurosurgery 43, 749–758 (1998)
10. Skrinjar, O., Nabavi, A., Duncan, J.: Model-Driven Brain Shift Compensation. Medical Image Analysis 6, 361–373 (2002)
11. Miller, K., Joldes, G.R., Lance, D. and Wittek, A.: Total Lagrangian Explicit Dynamics Finite Element Algorithm for Computing Soft Tissue Deformation. Communications in Numerical Methods in Engineering 23, 121–134 (2007)
12. Joldes, G.R., Wittek, A., Miller, K.: Suite of finite element algorithms for accurate computation of soft tissue deformation for surgical simulation. Medical Image Analysis 13(6), 912–919 (2009)
13. Joldes, G.R., Wittek, A., Mathieu, C., Warfield, S.K., Miller, K.: Real-time prediction of brain shift using nonlinear finite element algorithms. In: 12th international conference on medical image computing and computer-assisted intervention MICCAI 2009. Lecture Notes in Computer Science LNCS, vol 5762, London, UK, pp 300–307 (2009)
14. Yeoh, O.: Some Forms of Strain-Energy Function for Rubber. Rubber Chemistry and Technology 66, 754–771 (1993)
15. Joldes, G.R., Wittek, A., Miller, K.: An Efficient Hourglass Control Implementation for the Uniform Strain Hexahedron Using the Total Lagrangian Formulation. Communications in Numerical Methods in Engineering 24, 1315–1323 (2008)
16. Joldes, G.R., Wittek, A., Miller, K.: Non-locking Tetrahedral Finite Element for Surgical Simulation. Communications in Numerical Methods in Engineering. 25(7), 827–836 (2008)

Total Lagrangian Explicit Dynamics-Based Simulation of Tissue Tearing

Kumar Vemaganti, Grand R. Joldes, Karol Miller, and Adam Wittek

Abstract This study presents an approach to modeling the tearing of tissue in two dimensions taking into account both material and geometrical nonlinearities. The approach is based on the total Lagrangian explicit dynamics (TLED) algorithm and realigns edges in the mesh along the path of the tear by node relocation. As such, no new elements are created during the propagation of the tear. The material is assumed to be isotropic, and the tearing criterion is based on the maximum node-averaged principal stress. Preliminary results show that the approach is capable of handling both isotropic and anisotropic tears.

Keywords Tissue tearing · Tissue cutting · Total Lagrangian · Explicit dynamics · Soft tissue

1 Introduction

Simulations of tearing and cutting of tissue for use in computer-integrated surgery often pose significant challenges not only because of material and geometrical nonlinearities, but also due to the need to modify the mesh in real-time.

Much of the literature on cutting and tearing of soft tissue and other soft materials has focused on the geometrical aspects of the problem. Broadly, three approaches have been put forth: element deletion (e.g., [1]), mesh division (e.g., [2]), and mesh adaptation (e.g., [3–5]). While the first approach violates mass conservation principles, the second leads to an increase in the number of elements and nodes, a decrease in the size of the smallest element, and, consequently, a decrease in the time step size for explicit methods. The last approach, in which nodes are relocated to align element edges with the tear or cut, also leads to a decrease in the size of the smallest element but no new elements are introduced. A hybrid of the latter approaches has also been proposed [6].

K. Vemaganti (✉)
University of Cincinnati, Cincinnati, OH, USA
e-mail: Kumar.Vemaganti@gmail.com

A. Wittek et al. (eds.), *Computational Biomechanics for Medicine: Soft Tissues and the Musculoskeletal System*, DOI 10.1007/978-1-4419-9619-0_7,

Most published works use a spring-mass model or isotropic linear elastic model to represent the material response of soft tissue and completely ignore its well-known nonlinear response. Also often ignored is the large deformation undergone by soft tissue. A recent exception to this trend is the anisotropic tearing model investigated by [7]. Nonetheless, tearing/cutting approaches that fully account for material and geometrical nonlinearities are not currently available.

In this study, we develop an approach to modeling tissue tearing based on the total Lagrangian explicit dynamics (TLED) algorithm developed by Miller et al. [8]. The TLED algorithm is an efficient numerical algorithm for computing deformations of very soft tissues and easily handles both geometrical and material nonlinearities. It is based on the total Lagrangian formulation, where stresses and strains are measured with respect to the original configuration. This allows for the pre-computation of certain spatial derivative quantities and thus speed up computation. The current implementation is two-dimensional and uses linear triangular elements. The material is assumed to be isotropic, nonlinearly elastic, and capable of undergoing large deformations.

Tissue is assumed to undergo tearing when the node-averaged maximum principal stress exceeds a certain threshold. The tear is assumed to propagate perpendicular to the eigen-direction corresponding to the maximum principal stretch. Element edges are aligned with the direction of the tear, and the tear is allowed to propagate through the mesh.

The rest of the chapter is organized as follows. In Sect. 2, we briefly review the TLED algorithm introduced in [8]. We then present the details of the two-dimensional tearing algorithm and show results from its implementation. The chapter ends with a discussion of the results and some concluding remarks.

2 Review of the TLED Algorithm

The TLED algorithm is now summarized. The notation used here is adopted from [9] and [8], where the left superscript represents the current time and the left subscript the reference configuration.

The global system of equations to solve at time step n may be written as:

$$\mathbf{M}\ddot{\mathbf{u}}_n + \mathbf{K}(\mathbf{u}_n)\mathbf{u}_n = \mathbf{R}_n, \tag{1}$$

where $\mathbf{u}$ is the vector of global displacements, $\mathbf{M}$ is the global mass matrix, $\mathbf{K}$ is the global (nonlinear) stiffness matrix, and $\mathbf{R}$ is the vector of global nodal forces.

The TLED algorithm updates the displacements at the end of each time step using

$$\left(\frac{1}{\Delta t^2}\mathbf{M}\right)\mathbf{u}_{n+1} = \mathbf{R}_n - \sum_i \mathbf{F}_n^{(i)} - \frac{1}{\Delta t^2}\mathbf{M}(\mathbf{u}_{n-1} - 2\mathbf{u}_n), \tag{2}$$

where

$$\sum_i \mathbf{F}_n^{(i)} = \mathbf{K}(\mathbf{u}_n)\mathbf{u}_n = \sum_i \int_{V^{(i)}} \mathbf{B}^{\mathrm{T}}{}_n \tilde{\mathbf{S}}_n \, \mathrm{d}V. \tag{3}$$

Here, $\mathbf{F}_n^{(i)}$ is the nodal reaction force vector at step n, $\tilde{\mathbf{S}}_n$ the second Piola–Kirchhoff stress tensor, $\mathbf{B}^{\mathrm{T}}{}_n$ the strain–displacement matrix, and $V^{(i)}$ the volume of the ith element.

If a diagonal mass matrix is used, as is the case in this work, then this is a fully explicit step. Material nonlinearites are taken into account by computing the second PK stress $\tilde{\mathbf{S}}_n$ using the appropriate nonlinear constitutive model.

The overall algorithm may be stated as follows:

1. Load information about mesh, boundary conditions, material properties, etc.
2. For each element, precompute the area, determinant of the Jacobian, spatial derivatives of shape functions $\partial\mathbf{h}$, and strain–displacement matrices ${}^{t}_{0}B_{L0}$.
3. Compute diagonal mass matrix ${}^{0}\mathbf{M}$.
4. Initialize nodal displacements ${}^{0}\mathbf{u} = \mathbf{0}$, ${}^{-\Delta t}\mathbf{u} = \mathbf{0}$.
5. Apply prescribed forces and displacements for the first time step: ${}^{\Delta t}R_i^{(k)} \leftarrow R^{(k)}(\Delta t)$ and ${}^{\Delta t}u_i^{(k)} \leftarrow d(\Delta t)$.
6. At each time step, obtain net nodal reaction forces $\mathbf{F}$ as follows:
   a. For each element in the mesh, compute reaction forces as follows:
      i. Compute the deformation gradient ${}^{t}_{0}\mathbf{X}$ using nodal displacements from previous time step.
      ii. Calculate the full strain–displacement matrix:

$$ {}^{t}_{0}\mathbf{B}_L^{(k)} = {}^{t}_{0}\mathbf{B}_{L0}^{(k)}\,{}^{t}_{0}\mathbf{X}^{\mathrm{T}} \tag{4} $$

      iii. Compute the second PK stress tensor ${}^{t}_{0}\tilde{\mathbf{S}}$ at integration points.
      iv. Compute nodal reaction forces for the element:

$$ {}^{t}\mathbf{F}^{(m)} = \int_{0V} {}^{t}_{0}\mathbf{B}^{\mathrm{T}}{}_L\,{}^{t}_{0}\tilde{\mathbf{S}}\,\mathrm{d}\,{}^{0}V \tag{5} $$

   b. Explicitly compute displacements:

$$ {}^{t+\Delta t}u_i^{(k)} = \frac{\Delta t^2}{M_k}\left({}^{t}R_i - {}^{t}F_i^{(k)}\right) + 2\,{}^{t}u_i^{(k)} - {}^{t-\Delta t}u_i^{(k)} \tag{6} $$

   c. Apply loads for next step:

$$ {}^{t+\Delta t}R_i^{(k)} \leftarrow R^{(k)}(t+\Delta t);\ \ {}^{t+\Delta t}u_i^{(k)} \leftarrow d(t+\Delta t) \tag{7} $$

3 The Tearing Algorithm

The proposed cutting algorithm is based on the idea of moving nodes to align element edges with the path of the tear. It is assumed that this path can be determined from knowledge of the current state of stress, strain, etc., in the domain. Because the

underlying formulation is total Lagrangian, all mesh modifications are done in the reference configuration. This in particular means that the tear direction determined from the current state of stress must be mapped back to the reference configuration to align element edges with the tear. This is easily accomplished since the mapping is done through the inverse deformation gradient.

In the present work, the tearing condition is taken to be based on the maximum principal stress at a node:

$$f = \sigma_{\text{pr,max}} - \sigma_{\text{tol}} \geq 0. \tag{8}$$

If the condition $f \geq 0$ is satisfied at a node, then the node is marked as a candidate for the tear to pass through it, and appropriate mesh modifications are made as discussed below.

The tearing condition is checked and the mesh modifications are carried out at the end of step 6b in the TLED algorithm shown in the previous section.

3.1 Mesh modification

If it is determined that the tear condition is satisfied at an interior node, then the following modifications are made to the mesh.

- Of the edges passing through the node, find the two that are closest to the tear direction.
- Move relevant nodes to align these edges with the tear direction.
- Update by interpolation the displacements, etc., associated with moved nodes.
- Recompute element-specific quantities such as area, **B**, etc.
- Introduce new node at the location of the critical node and new edges along the tear path.
- Update element connectivity and other data structures.

Figure 1 shows a schematic of these modifications.

Similarly, if the tear condition is satisfied at a boundary node, then the mesh is modified accordingly. In this case, generally but not always, only one of the edges around the node needs to be realigned. This is shown in Fig. 2.

Finally, if the tear condition is satisfied at a node that is the only connection between two parts of the domain, then the mesh is modified by introducing a duplicate node at that location and separating the parts. This is illustrated in Fig. 3.

Because we use an explicit scheme to solve equations of motion, the time step used in the algorithm has a significant effect on stability. The critical time step is equal to the ratio of the smallest characteristic length of an element (L_{e}) to the dilatational wave speed c

$$\Delta t \leq \frac{L_{\text{e}}}{c}. \tag{9}$$

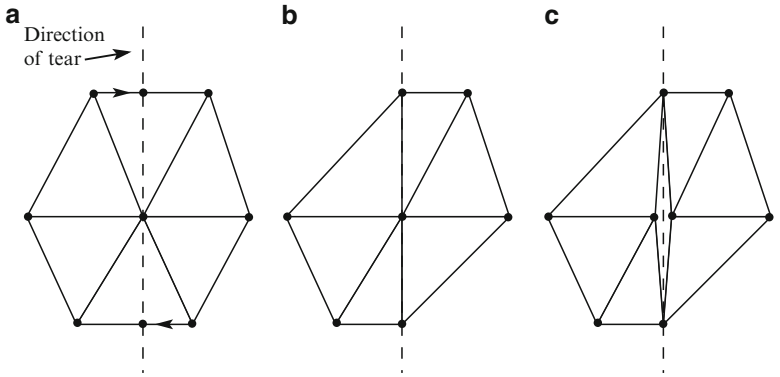

Fig. 1 Mesh modification for interior nodes. (**a**) After determining the edges closest to the tear direction, (**b**) nodes are moved to align the edges with tear. (**c**) A new node and two new edges are then introduced

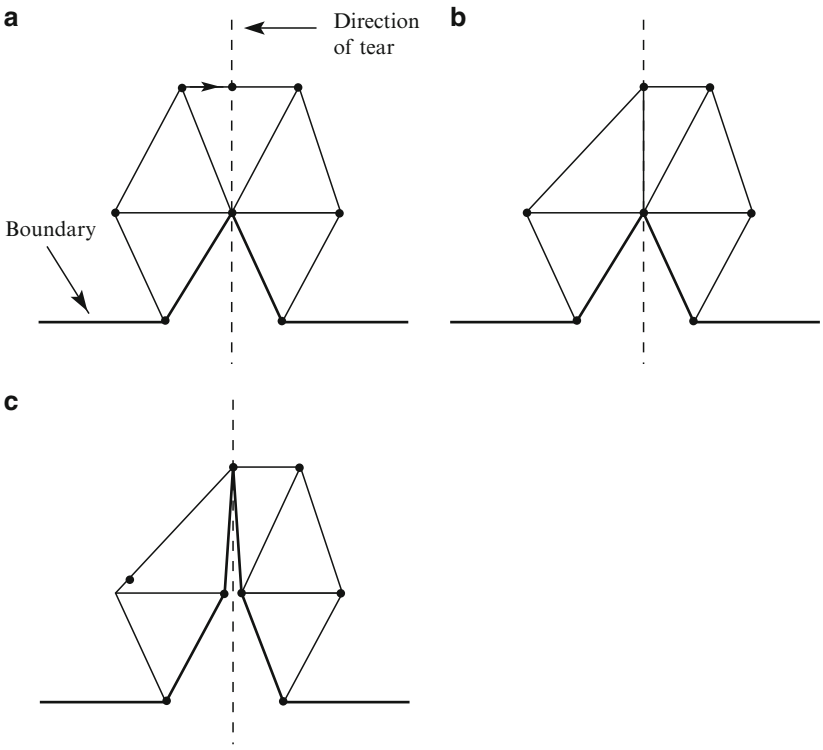

Fig. 2 Mesh modification for boundary nodes. (**a**) After determining the edge(s) closest to the tear direction, (**b**) node(s) are moved to align the edge(s) with tear. (**c**) One new node and one or two new edges are then introduced, depending on the tear direction

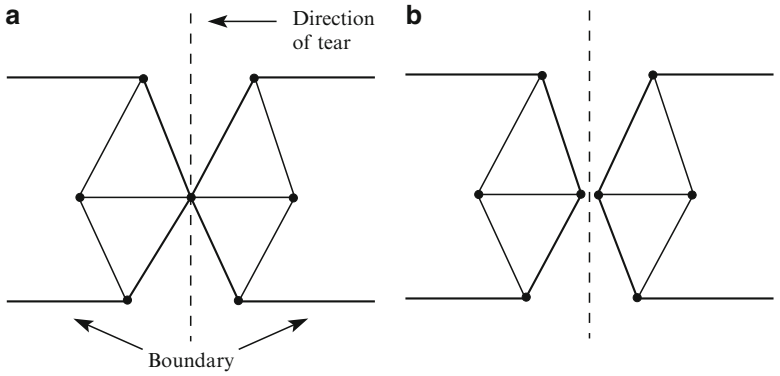

Fig. 3 Mesh modification for domain separation. (**a**) If a tear passes through a node connecting two masses, (**b**) a new node is introduced

For triangular elements, the characteristic length is

$$L_{\mathrm{e}} = \frac{A}{h_{\max}}, \tag{10}$$

where A is the element area and $h_{\max}$ is the tallest side. In the proposed approach, the realignment of element edges leads to a reduction of Δt by a factor of 2 at the most.

4 Results

As a model problem, we consider the tearing of a notched rectangle of size 4 cm × 10 cm shown in Fig. 4. The material is assumed to be Neo-Hookean with Young's modulus (in the reference configuration) 3,000 Pa and Poisson's ratio 0.49. The material's mass density is 1,000 kg/m^3. The left edge of the rectangle is held fixed and the right edge displaced by 2 cm with the following profile:

$$d(t) = (10 - 15t + 6t^2)t^3, \tag{11}$$

where t is the relative time varying from 0 to 1.

A relatively coarse mesh is used to model the region. It is assumed that tissue tearing occurs when the maximum principal stress reaches or exceeds 1,100 Pa. The displacement loading on the right edge is applied in 1,000 steps.

The results of the simulation are shown in Fig. 5, where the contour levels indicate the maximum nodal principal stress, and the red circle represents the location of its highest value in the domain. At step 750, the maximum principal stress at the tip of the notch is just below the tolerance for tearing. The tearing criterion is met at step 772 at the notch tip, and the node there is treated as a boundary node.

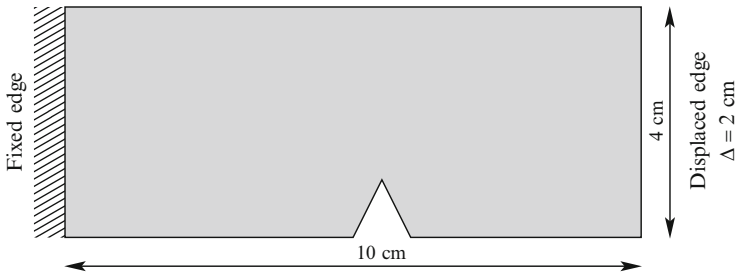

Fig. 4 Schematic of a notched rectangle undergoing 20% strain loading in the horizontal direction

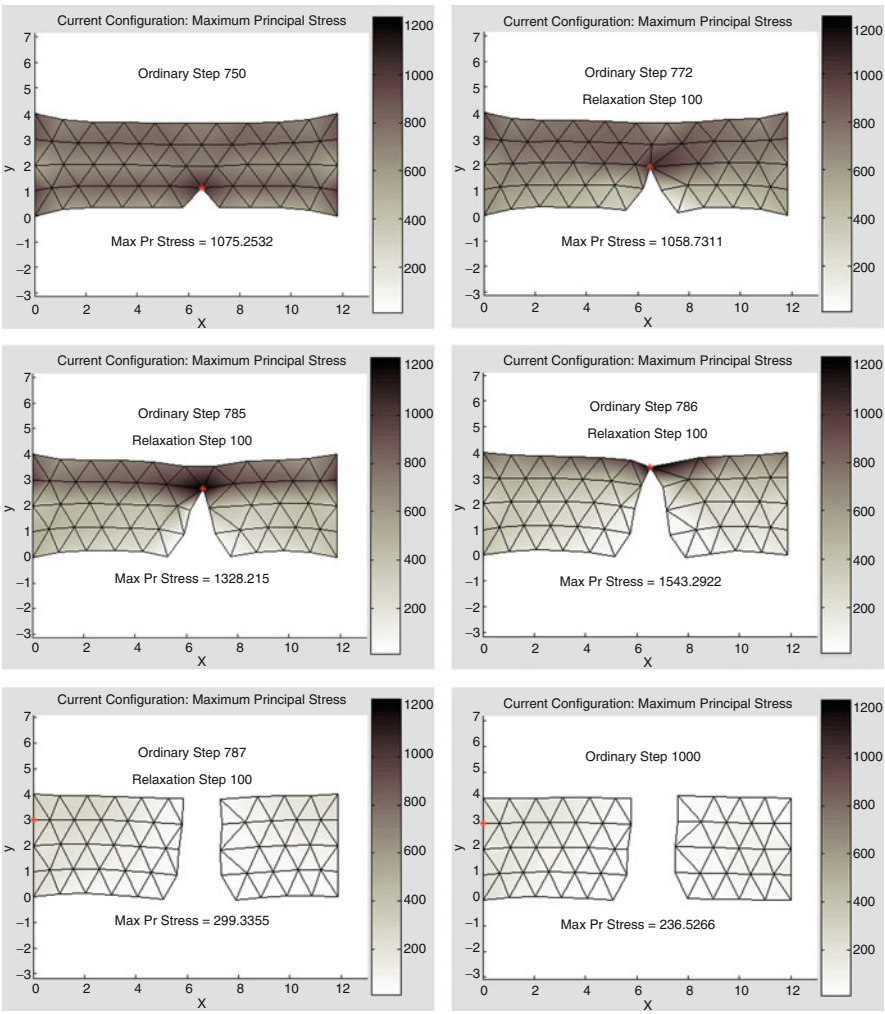

Fig. 5 Contour plot of maximum (nodal) principal stress at various stages of tearing for a notched rectangle undergoing 20% strain

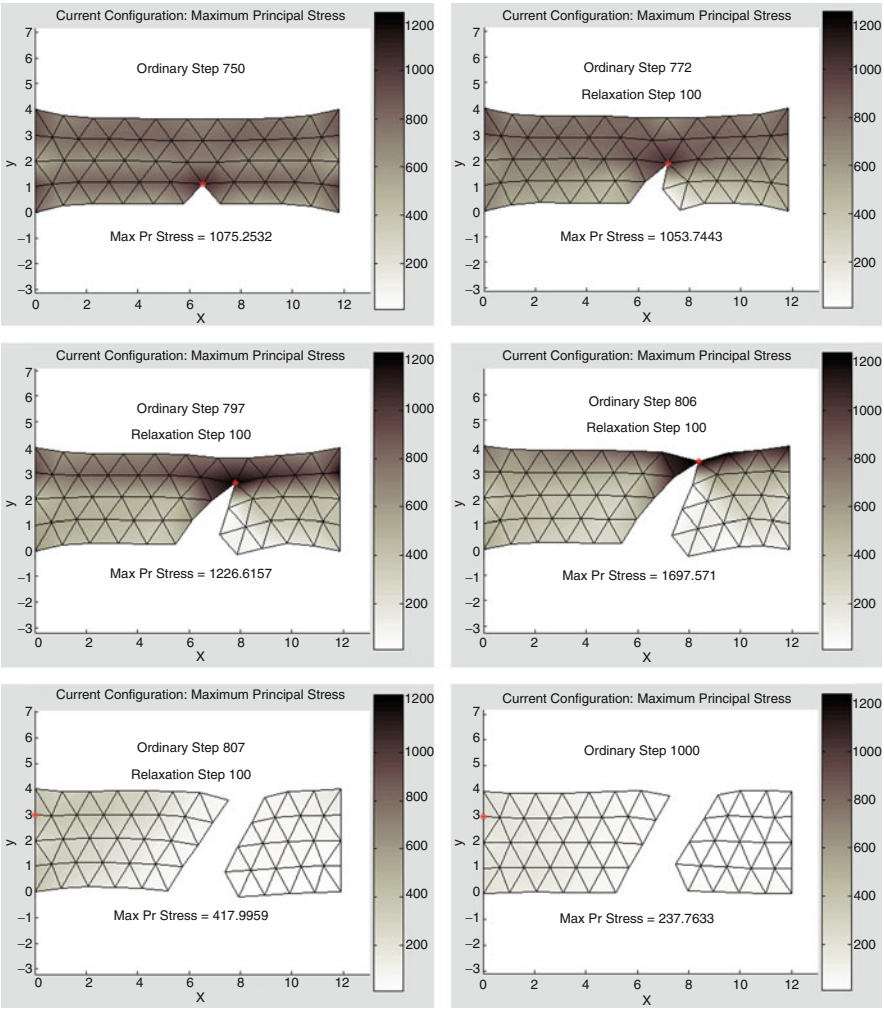

Fig. 6 Contour plot of maximum (nodal) principal stress at various stages of tearing for a notched rectangle undergoing 20% strain. The tear is assumed to have a preferred direction of $\pi/3$ with the horizontal

After the tear is introduced, 100 steps of dynamic relaxation (DR) are carried out, during which time there are no changes in the loading. The dynamic relaxation steps help diffuse the disturbances that emanate from the sudden introduction of a cut in the domain [10]. The number of DR steps is ad hoc at present and chosen based on testing.

The process is repeated and further tearing occurs at steps 785 and 786, at the end of which the domain is on the verge of splitting into two parts. At step 787, the two parts finally separate. The simulation concludes at step 1000, resulting in

the domain partition shown. Because the simulation is completely based on explicit dynamics, the separation of the domain into two parts poses no problems in the updating scheme.

Next, the simulation is repeated assuming that the tear has a preferential direction of $\pi/3$ with the horizontal. This time, the simulation proceeds as before and the mesh modification proceeds smoothly leading to the partition shown in Fig. 6.

5 Concluding Remarks

In the literature, there are few simulations of tissue tearing. Some of the existing approaches include element subdivision and remeshing. In this work, we adopt an approach whereby no new elements are created, but the mesh is modified on the fly by aligning element edges along the tear path. Because the approach is built on top of the TLED algorithm, material and geometrical nonlinearities are taken into account fully.

We have made some simplifying assumptions in our work. First, we have assumed the material response to be isotropic. A more interesting and challenging simulation would involve tearing of fibrous materials, where a preferred direction of tearing is dictated by the material's anisotropy. Our approach can be easily adapted to such a case if a reasonable tear criterion can be formulated; see, for instance, [7]. Second, we have only investigated a hyperelastic Neo-Hookean response. Experiments with other hyperelastic materials as well as viscohyperelastic materials are planned.

A major test of the proposed approach will be its extension to three spatial dimensions. While the results from our 2D experiments are encouraging, 3D implementations are typically orders of magnitude more complex. Nonetheless, we believe that our TLED-based approach is feasible in three dimensions considering the fact that much work has already been published on tetrahedra-based cutting and tearing [2, 4, 5].

Acknowledgments This research was carried out while the first author was a visiting professor at the University of Western Australia.

References

1. J. Yan, J.S. Strenkowski, Journal of Materials Processing Technology **174**, 102 (2006)
2. A.B. Mor, T. Kanade, in *MICCAI 2000*, ed. by S.L. Delp, A.M. DiGioia, B. Jaramaz (Springer-Verlag, 2000), pp. 598–608
3. H.W. Nienhuys, A.F. van der Stappen, in *MICCAI 2001*, ed. by W. Niessen, M. Viergever (Springer-Verlag, 2001), pp. 145–152

4. C. Mendoza, C. Laugier, in *IS4TM 2003*, ed. by N. Ayache, H. Delingette (Springer-Verlag, 2003), pp. 175–182
5. C. Mendoza, C. Laugier, in *Proceedings of the 2003 IEEE International Conference on Robotics and Automation* (2003), pp. 1109–1114
6. M. Harders, D. Steinemann, M. Gross, G. Szekely, in *MICCAI 2005*, ed. by J. Duncan, G. Gerig (Springer-Verlag, 2005), pp. 567–574
7. J. Allard, M. Marchal, S. Cotin, in *Medicine Meets Virtual Reality 17* (IOS Press, 2009), pp. 13–18
8. K. Miller, G.R. Joldes, D. Lance, A. Wittek, Commun. Numer. Meth. Engng. **23**, 121 (2007)
9. K.J. Bathe, *Finite Element Procedures* (Prentice-Hall, Englewood Cliffs, NJ, 1996)
10. G.R. Joldes, A. Wittek, K. Miller, Int. J. Numer. Meth. Biomed. Engng. **27**, 173 (2011)

Real-Time Nonlinear Finite Element Computations on GPU: Handling of Different Element Types

Grand R. Joldes, Adam Wittek, and Karol Miller

Abstract Application of biomechanical modeling techniques in the area of medical image analysis and surgical simulation implies two conflicting requirements: accurate results and high solution speeds. Accurate results can be obtained only by using appropriate models and solution algorithms. In our previous papers, we have presented algorithms and solution methods for performing accurate nonlinear finite element analysis of brain shift (which includes mixed mesh, different nonlinear material models, finite deformations and brain–skull contacts) in less than 5 s on a personal computer using a Graphics Processing Unit (GPU) for models having up to 50,000 degrees of freedom. In this chapter, we compare several approaches for implementing different element types on the GPU using the NVIDIA Compute Unified Device Architecture. Our results can be used as a guideline for selecting the best GPU implementation approach for finite element algorithms which require mixed meshes or even for meshless methods.

Keywords Finite element method implementation · Graphics Processing Unit · CUDA · Mixed meshes

1 Introduction

Researchers in the surgical simulation community commonly use mathematical models based on linear elasticity because of their computational efficiency [1–3]. These models are not capable of providing realistic predictions of finite deformations of the tissue because of the assumptions of very small deformations and linear material response. Years of experience accumulated by researchers working on the theory of elasticity and the finite element method have shown that the linear

G.R. Joldes (✉)
Intelligent Systems for Medicine Laboratory, School of Mechanical and Chemical Engineering, The University of Western Australia, 35 Stirling Highway, 6009 Crawley/Perth, WA, Australia
e-mail: grandj@mech.uwa.edu.au

A. Wittek et al. (eds.), *Computational Biomechanics for Medicine: Soft Tissues and the Musculoskeletal System*, DOI 10.1007/978-1-4419-9619-0_8,

elasticity assumptions cannot be used for systems undergoing large deformations. Many examples of the limitations of linear theory were published, see, e.g. [4, 5]. Therefore, an efficient finite element algorithm that accounts for both geometric and material nonlinearities is needed.

For real-time intraoperative applications very high computational efficiencies are required. Highly nonlinear 3D finite element models with more than 50,000 degrees of freedom need to be solved in less than 1 min.

To alleviate the problems mentioned above we developed at the Intelligent Systems for Medicine Laboratory a Total Lagrangian Explicit Dynamics (TLED) finite element algorithm [6]. This algorithm accounts for both geometric and material nonlinearities, and allows near-real-time computations on a standard PC. The key idea behind TLED is to use the Total Lagrangian formulation of the finite element method, where all variables are referred to the original configuration of the system. Second Piola–Kirchhoff stress and Green strain are used. The decisive advantage is that all spatial derivatives are calculated with respect to the original configuration and therefore can be precomputed. Our numerical experiments show that TLED is approximately three times faster than algorithms based on Updated Lagrangian formulation used by all commercial finite element packages and the great majority of researchers [7–9].

An explicit dynamics algorithm can be easily transformed into a Dynamic Relaxation algorithm with the inclusion of a mass proportional damping [10]. Such an algorithm allows the iterative computation of the final, deformed configuration of an organ without the need of solving any large system of equations [11–14].

Like every other FE algorithm, TLED requires the creation of finite element meshes. Explicit finite element algorithms work efficiently when eight-noded hexahedral elements are used [4, 5]. As human organs have very irregular shapes, meshing them using hexahedra presents itself as a very significant problem. One needs to create the mesh for each patient undergoing surgery, based on her/his radiological images. Over the years, despite significant research effort (see, e.g. [15]) there has been little success in the development of automatic (or semiautomatic) methods for creation of hexahedral meshes, suitable for nonlinear, finite deformation computations, from medical images. Recently popular voxel-based meshing methods cannot be used in near-real-time applications because they produce meshes with too many degrees of freedom and with many elements of poor quality requiring labor-intensive corrections [15]. Therefore mixed meshes, containing both hexahedral and tetrahedral elements, are normally used.

With the latest developments in technology, graphics processing units (GPU) have been adapted for general purpose scientific computations. Although the potential of using GPU for general purpose computations has been known for some time, developing software for GPU was difficult, as the GPU could only be programed through a graphics interface, imposing a high learning curve to the novice and the overhead of an inadequate interface to the nongraphics application. Only recently the major GPU manufacturer NVIDIA has developed the Compute Unified Device Architecture (CUDA) which offers a complete development environment (with a C-like compiler and a software development kit) that can be used in order

to fully benefit from the GPU capabilities [16]. A GPU implementation of the TLED algorithm can perform a brain shift simulation in less than 4 s for models having more than 50,000 degrees of freedom [17] on an NVIDIA Tesla C780 GPU, which is more than 20 times faster than a CPU implementation of the same algorithm.

The GPU is used as a coprocessor for CPU to perform operations that can be executed in parallel. The GPU performs best for algorithms that perform the same operations on multiple data structures. In the case of a finite element implementation, each element can be considered a data structure. When the algorithm has to handle different types of elements, the computations cannot be done in parallel, as the data structures and the operations required are different. In this chapter, we discuss and compare four approaches to the implementation of different finite elements on GPU. We use mixed meshes containing two types of elements (under-integrated hexahedral elements with hourglass control and linear tetrahedral elements) but the implementation approaches can be extended to other types of elements as well. The results can be used as a guideline for selecting the best GPU implementation approach for finite element algorithms which require mixed meshes or even for meshless methods.

The chapter is organized as follows: the four approaches to implementing different finite elements on GPU are presented in the next section, timing comparisons are presented in Sect. 3 and the last section contains discussions and conclusions.

2 GPU Implementation Approaches for Different Finite Elements

The GPU has a highly parallel, multithreaded, multicore processor architecture. This is well suited for problems that can be expressed as data-parallel computations with high arithmetic intensity, where the same program is executed on many data elements in parallel. CUDA is a general purpose parallel computing architecture that allows the development of application software that transparently scales with the number of processor cores in the GPU.

The code executed on GPU is called a kernel. When a kernel is invoked (from the CPU), it is executed N times in parallel by N different CUDA threads (N is specified during the kernel invocation). Threads are organized into a grid of blocks, with each block identified by a block index, while each thread within the block is identified by a thread index. Threads within a block can cooperate among themselves by sharing data through shared memory and synchronizing their execution to coordinate memory accesses. The number of threads per block is restricted by the limited memory and register resources of a processor core. Thread blocks are required to execute independently, therefore they cannot cooperate among themselves.

The CPU running the program that launches the kernels is called the *host*, while the GPU acts as a coprocessor running the CUDA threads, called the *device*.

The host and the device maintain their own DRAM, referred to as the host memory and the device memory (global, constant, and texture memory are implemented in the device memory).

For a finite element algorithm implementation on the GPU, each element can be considered as a data structure. When assembling global vectors (such as the nodal force vector), the contributions from each element in the mesh is required. In an explicit code the nodal force vector computation is the most computationally intensive part of the solution algorithm. While on the CPU the elements are treated sequentially (e.g., in a "for" loop), on the GPU all elements can be treated in parallel (each element is handled by a CUDA thread), as long as the same code is executed. If some elements require the execution of different code, this code must be handled by a different kernel.

Our first GPU finite element implementation, presented in [17], used a different kernel for implementing each element type (the "multiple kernels" approach). In this approach the elements are grouped based on their types, and the nodal force computation is organized as follows:

CPU	GPU
For each element type in the mesh:	
	Compute nodal forces for all elements belonging to this element type

Apart from this approach, we consider three other approaches that can be used for implementing different element types. The common characteristics of all these approaches is that they use the same code to handle different element types, therefore only one kernel is needed to handle all elements in the mesh, reducing the number of kernel invocations on CPU. The nodal force computation is then organized as follows:

CPU	GPU
Invoke kernel for nodal force computation:	
	Compute nodal forces for all elements in the mesh

(a) The "parametric elements" approach
This approach uses parameters to describe each element. These parameters have different values for different element types. Examples of such parameters are the number of nodes, whether or not hourglass control is used, the number of hourglass control shape vectors, etc. Therefore, the computations inside each kernel have different results for different element types because of the use of different parameters.

(b) The "degenerated elements" approach
In this approach, element degeneration is used to create elements with lower number of nodes from more complicated elements, by merging of nodes. For

example, all linear tetrahedral, pyramidal, and prismatic elements can be treated as linear hexahedral elements with merged nodes. The merging of nodes is easily done by pointing the location indexes for different nodes toward the same location. Using this technique, all elements in the mesh that can be obtained from a linear hexahedron can be treated as linear hexahedrons.

(c) The "fat kernel" approach
A "fat kernel" is a combination of multiple independent kernels that are executed in one invocation. For example, considering Kernel_1 that must be invoked with N_1 number of threads and Kernel_2 that must be invoked with N_2 number of threads, a "fat kernel" Kernel_1_2 that invokes both these kernels can be constructed as follows:

Kernel_1_2 (invoked with N_1 + N_2 threads):
// check to which kernel the current thread belongs to
if (thread_ID < N_1)
execute Kernel_1 for thread_ID;
else
execute Kernel_2 for (thread_ID – N_1);

In the case of finite element implementation, all kernels from the "different kernels" approach can be combined in a "fat kernel" – which can handle all elements in the mesh at once – because they are independent (they work on independent data – the elements). This reduces the hardware and software overhead associated with kernel invocations from the CPU, as only one kernel invocation is needed.

For all these approaches, it is important that the different type of elements are grouped together when assigned to GPU threads, so that threads which are handled concurrently on the same processor execute the same code most of the time (the code paths from these threads that diverge will be executed sequentially).

3 Timing Comparison

The different approaches presented above were implemented in our TLED algorithm [6, 12, 17]. We meshed a cylinder using hexahedral and tetrahedral elements in different proportions (as presented in Table 1 and Fig. 1) and performed compression experiments using the same number of explicit steps (4,000). The computations were performed on an Intel Core 2 Quad CPU at 2.83 GHz with an NVIDIA C1080 GPU. The computation times are presented in Table 2.

From Table 2, it is clear that the computation time increases as the proportion of tetrahedral elements in the mesh increases, irrespective of which approach is used for implementing the elements. This is expected, as one hexahedral element is replaced by at least five tetrahedral elements (for the same number of nodes in the mesh). Therefore, to minimize the computation time, it is advisable to have as many hexahedral elements in the mesh as possible.

Table 1 Meshes used for timing comparison

Mesh	Total elements	Hexas	Tetras
Mesh 1 (majority hexas)	54,050	46,800	7,250
Mesh 2 (hexas ≈ tetras)	96,400	38,400	58,000
Mesh 3 (majority tetras)	223,450	13,200	210,250

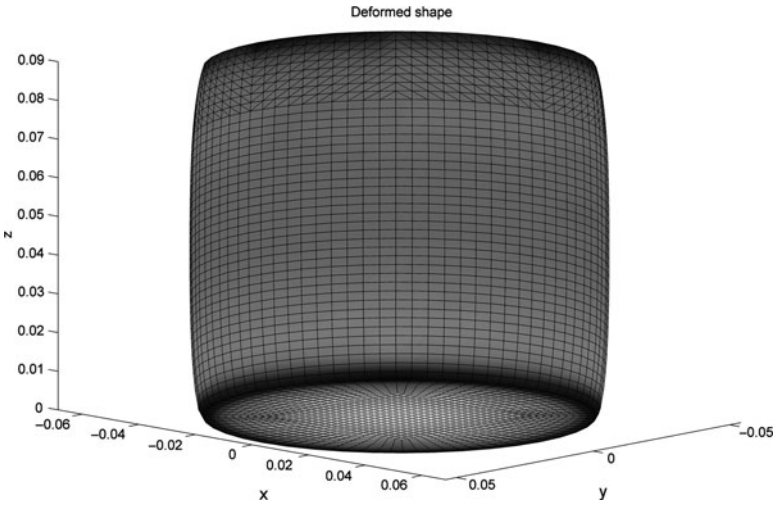

Fig. 1 Deformed cylinder shape for Mesh 2

Table 2 Computation times for the different element implementation approaches (4,000 explicit steps were executed, computation time is in seconds)

	Implementation approach			
Computation time (s)	Multiple kernels	Parametric elements	Degenerated elements	Fat kernel
Mesh 1 (majority hexas)	4.34	4.84	4.82	4.11
Mesh 2 (hexas ≈ tetras)	5.28	5.84	8.45	4.94
Mesh 3 (majority tetras)	7.5	10.07	20.36	7.34

The "multiple kernels" approach performed better than expected compared with the other approaches, demonstrating that the kernel invocation from the NVIDIA driver is very efficient. Nevertheless, the performances are expected to degrade as the number of kernel invocations increase (as the mesh contains more different types of elements), because each kernel invocation introduces a small hardware and software overhead.

The "fat kernel" approach outperformed all the other approaches in terms of computation time. This happens because the kernels for each element type can be written very efficiently and then combined in the "fat kernel," so that the GPU does not have to perform unnecessary operations. It is important to note that the kernels that are combined in a "fat kernel" should have similar needs in terms of shared memory and

registers, as this determines the number of threads that can be executed in parallel on a GPU multiprocessor. If one of the kernels requires a much higher number of registers or a lot of shared memory, it can reduce the number of threads that can be executed in parallel for all the other kernels, therefore degrading the performance.

The "degenerated elements" approach performed the worst, especially as the proportion of tetrahedral elements in the mesh increased. This is a consequence of treating all elements as hexahedral elements, which leads to a lot more supplementary operations that have to be executed for the tetrahedral elements.

The performance of the "parametric elements" approach is somewhere in the middle. The use of parameters to define each element leads to additional operations that the GPU has to perform. Nevertheless, if the number of different element types in the mesh is increased, this could become the preferred option. Looking beyond the finite element method, this could be especially the case for a meshless method implementation with variable number of nodes associated to each integration point, as it would be difficult to implement different kernels for each possible combination.

We performed the same tests on meshes with increased number of elements (about eight times more elements than the meshes presented in Table 1). The computation times increased linearly with the number of elements (around eight times), but the relative performances of the analyzed implementation methods were the same.

4 Discussion and Conclusions

GPUs are a cost effective and efficient method of accelerating code execution, especially for algorithms that are easily parallelizable, such as explicit finite element algorithms. Using such algorithms implemented on GPU, real time surgery simulations are possible using complex and accurate biomechanical models.

The GPU architecture and internal organization is relatively complex. When algorithms are developed for a GPU there are a number of rules that have to be observed in order to get the maximum performance [16,17]. Apart from these rules, the structuring of the software and the communication between CPU and GPU can have a great influence on the performance. In this chapter, we present four approaches that can be used to implement different finite element types on the GPU.

We implemented the presented approaches and performed timing measurements to compare their performances. The "fat kernel" approach, in which different kernels that can be executed in parallel are combined in a single kernel, provided the best performance.

There are cases when the number of different kernels that have to be implemented is too large, especially for meshless methods with variable number of nodes per integration points. In such cases, the "parametric elements" would be the best implementation approach.

Acknowledgments The financial support of the Australian Research Council (Grants DP0664534, DP1092893, and DP0770275) is gratefully acknowledged.

References

1. Christensen GE, Johnson HJ. *Consistent Image Registration*. IEEE Transactions on Medical Imaging. 2001; **20**(7): 568-582.
2. Clatz O, Delingette H, Bardinet E, Dormont D, Ayache N. *Patient Specific Biomechanical Model of the Brain: Application to Parkinson's disease procedure. in International Symposium on Surgery Simulation and Soft Tissue Modeling (IS4TM'03)*. 2003. Juan-les-Pins, France: Springer-Verlag.
3. Hagemann A, Rohr K, Stiehl HS. *Coupling of fluid and elastic models for biomechanical simulations of brain deformations using FEM*. Medical Image Analysis 2002; **6**(4): 375-388.
4. Martin HC, Carey GF. *Introduction to Finite Element Analysis: Theory and Application*. 1973, New York: McGraw-Hill Book Co.
5. Oden JT, Carey GF. *Finite Elements: Special Problems in Solid Mechanics*. 1983: Prentice-Hall.
6. Miller K, Joldes GR, Lance D, Wittek A. *Total Lagrangian Explicit Dynamics Finite Element Algorithm for Computing Soft Tissue Deformation*. Communications in Numerical Methods in Engineering 2007; **23**: 121-134.
7. Joldes GR, Wittek A, Miller K. *Suite of finite element algorithms for accurate computation of soft tissue deformation for surgical simulation*. Medical Image Analysis 2009; **13**(6): 912-919.
8. Miller K, Joldes GR, Wittek A. *New Finite Element Algorithm for Surgical Simulation*. in *2nd Workshop on Computer Assisted Diagnosis and Surgery*. 2006. Santiago de Chile.
9. Joldes GR, Wittek A, Miller K. *Towards Non-Linear Finite Element Computations In Real Time*. in *7th International Symposium On Computer Methods In Biomechanics And Biomedical Engineering (CMBBE2006)*. 2006. Antibes, Cote D'Azur, France.
10. Underwood P, *Dynamic Relaxation*, in *Computational Methods for Transient Analysis*, T. Belytschko and T.J.R. Hughes, Editors. 1983, New-Holland: Amsterdam. p. 245–265.
11. Joldes GR, Wittek A, Miller K. *Computation of intra-operative brain shift using dynamic relaxation*. Computer Methods in Applied Mechanics and Engineering 2009; **198**(41-44): 3313-3320.
12. Joldes GR, Wittek A, Miller K. *An adaptive Dynamic Relaxation method for solving nonlinear finite element problems. Application to brain shift estimation*. International Journal for Numerical Methods in Biomedical Engineering 2011; **27**(2): 173-185.
13. Miller K, Wittek A, Joldes GR, Horton A, Roy TD, Berger J, Morriss L. *Modelling brain deformations for computer-integrated neurosurgery*. Communications in Numerical Methods in Engineering 2009; **26**(1): 117-138.
14. Joldes GR, Wittek A, Couton M, Warfield SK, Miller K. *Real-Time Prediction of Brain Shift Using Nonlinear Finite Element Algorithms*. in *Proceedings of the 12th MICCAI Conference*. 2009. London, UK.
15. Viceconti M, Taddei F. *Automatic generation of finite element meshes from computed tomography data*. Critical Reviews in Biomedical Engineering 2003; **31**(1): 27-72.
16. NVIDIA, *CUDA Programming Guide Version 1.1*. 2007, NVIDIA Corporation: Santa Clara, CA 95050.
17. Joldes GR, Wittek A, Miller K. *Real-Time Nonlinear Finite Element Computations on GPU - Application to Neurosurgical Simulation*. Computer Methods in Applied Mechanics and Engineering 2010; **199**(49-52): 3305-3314.

Mapping Breast Cancer Between Clinical X-Ray and MR Images

Hayley M. Reynolds, Jaykumar Puthran, Anthony Doyle, Wayne Jones, Poul M.F. Nielsen, Martyn P. Nash, and Vijay Rajagopal

Abstract Characterizing a breast lesion can involve comparing X-ray and magnetic resonance (MR) images of a patient's breast. Tracking a lesion between these imaging modalities is nontrivial because of the different types of deformation the breast undergoes during these imaging procedures. We present a retrospective clinical validation study to assess the performance of a biomechanical modeling framework for mapping lesion locations between clinical MR images and cranio-caudal X-ray mammograms. MR images from four patients were used to create customized finite element models. The unloaded configuration of each breast was then determined, and mammographic compression was simulated using finite deformation elasticity coupled with contact mechanics. The predicted location of each patient's tumor(s) in the simulated compressed breast was compared with the true tumor locations on the mammogram as identified by clinicians. The degree of overlap between the true lesion area and the predicted lesion area, estimated using the Jaccard coefficient, ranged between 14 and 75%. The results indicate that biomechanical modeling can provide reliable co-location of lesions between MR images and mammograms.

Keywords Biomechanical modeling · Breast cancer · Contact mechanics · Finite deformation elasticity

1 Introduction

X-Ray mammography is the gold-standard imaging technique for early detection of breast cancer. Mammograms alone cannot be used to identify and characterize all cancers, partly because of their 2D representation of a 3D compressed breast, and also because of their limited applicability to women with dense breasts. Hence, mammography is often used in conjunction with other 3D imaging modalities such as ultrasound (US) and magnetic resonance (MR) imaging to reliably characterize

H.M. Reynolds (✉)
Auckland Bioengineering Institute, The University of Auckland, Auckland, New Zealand
e-mail: h.reynolds@auckland.ac.nz

A. Wittek et al. (eds.), *Computational Biomechanics for Medicine: Soft Tissues and the Musculoskeletal System*, DOI 10.1007/978-1-4419-9619-0_9,

the nature of a suspicious lesion. For example, contrast-enhanced MR imaging provides a 3D view of the blood supply to a suspicious region, which provides a measure of malignancy.

It is not always trivial, however, to match the location of lesions between X-ray mammograms and other imaging modalities. During MR imaging, the breasts typically hang prone under the effect of gravity in a breast coil, while during mammography the breast is forced into a highly compressed shape between two mammography plates to acquire an image with sufficient contrast at low X-ray dosage. As a result, these imaging procedures deform internal tissues significantly and in different ways, making point to point correspondence between images a nonlinear problem.

Biomechanical models have been investigated as a possible method to aid in reliable co-location of suspicious lesions between different imaging modalities [8]. Ruiter et al. [9] performed one of the first studies on the use of biomechanical models to map information between X-ray mammograms and MRI. The study used biomechanical models of six patients' breasts and incorporated details regarding the heterogeneity in tissue properties (e.g., skin, fat, and fibrous tissue) using estimates from published literature. The study showed promising results and concluded that a homogeneous model would be sufficient for the application. However, a number of assumptions in the models remain untested. Considering the significant variability in breast tissue properties across individuals, the validity of using estimates of tissue stiffness from ex vivo experimental studies must be examined. The simulations also used displacement boundary conditions on model surface nodes to match the mammogram skin contour. Such modeling assumptions are inappropriate, because it is not possible to determine displacement of the skin within its tangent plane from the images. Thus, these models may overconstrain the in-plane motion of the skin and produce unreliable results.

Hipwell et al. [3] also use a biomechanical model to map information from MR images onto 2D mammograms, but only used the model as a gold-standard to validate other nonrigid registration algorithms for this application. As such, the biomechanical model was not created with a specific case in mind, and thus did not require validation. It is also important to note that the use of nonrigid registration algorithms for MR to X-ray mapping can permit physically implausible transformations, which limit their reliability.

Recently, Rajagopal et al. [7] presented a method for determining the 3D location of microcalcifications from two X-ray mammograms using the modeling framework of Chung et al. [2]. This method did not make assumptions regarding the movement of the skin surface during compression and used patient-specific mechanical property estimates. The study validated the technique quantitatively on silicon gel phantoms, but only demonstrated its potential use for mapping mammography information onto a 3D MR dataset with one clinical case.

This chapter presents a quantitative assessment of the performance of the Chung et al. modeling framework for tracking breast tumor movement from clinical MR images to cranio-caudal X-ray mammograms. The study highlights how an individual-specific breast model can assist in performing the nonlinear mapping of information from MRI to X-ray mammograms. It demonstrates how the use of

realistic representations of loading and boundary conditions alone can simulate the significantly large compressions that the breast undergoes (over 50%) during mammography that has not been reported in the literature to date [10]. Limitations of the adoptability of these biomechanical modeling techniques within the clinical environment are discussed.

2 Methods

2.1 Clinical Data

Clinical data from four female patients treated at Auckland City Hospital, New Zealand, have been used in this study. Patients ranged in age from 33 to 57 years, and each had a visible cancerous lesion in their mammogram and MR images.

During MR imaging, patients were oriented in the prone position, with their breasts hanging under gravity in a breast coil. Axial MR images using a T1-weighted sequence were collected, where three patients were imaged using a 1.5T Siemens MRI scanner (Magnetom Avanto System), while the fourth patient was imaged using a Philips Intera Achieva 3.0T MRI scanner. Table 1 gives the MR image details for each patient. The digital mammography images were collected using a GE Healthcare Senograph mammography system. These images had pixel dimensions $1{,}914 \times 2{,}294$ which measured 180.09×215.84 mm.

2.2 Finite Element Modeling

A finite element (FE) model was created for each breast, by first segmenting the MR images to identify the skin, rib, and tumor boundaries (as shown in Fig. 1a) using CMGUI software[1]. The tumors were located by trained radiologists to ensure that the entire tumor was encircled.

A tricubic Hermite hexahedral FE mesh using 98 nodes and 36 elements (2352 geometric degrees of freedom) was created to represent the breast geometry for

Table 1 MR image dimensions for each patient

Patient	Resolution (pixels)	Field of view (mm)	# Slices	Slice thickness (mm)
1	512×512	340×340	192	0.75
2	512×512	360×360	208	0.75
3	448×448	340×340	104	1.5
4	560×560	330×330	50	3

[1] http://www.cmiss.org/cmgui

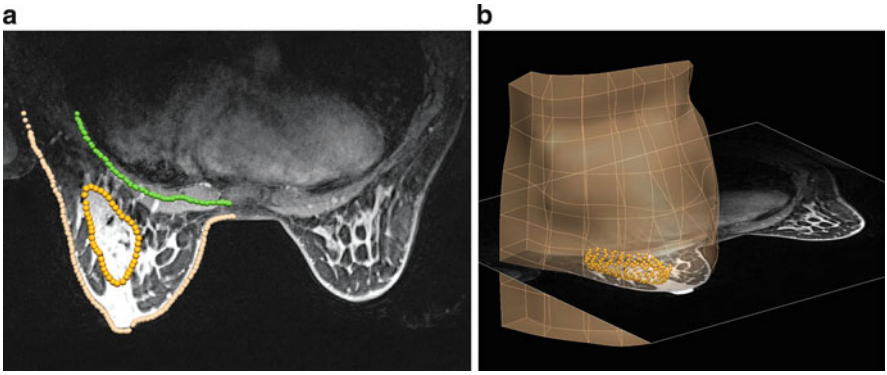

Fig. 1 Patient-specific breast models were created by (**a**) segmenting the MR images to identify tissue boundaries for the skin (*skin color*), rib (*green*) and tumor (*gold*), and (**b**) fitting a 3D finite element model to the skin and rib data

each patient. Six elements were defined in the mediolateral direction, six elements in the inferior-superior direction, and one element in the anteroposterior direction. The mesh extended in the mediolateral direction to the axilla to ensure adequate breast tissue was accounted for. A mesh node was positioned at the nipple to provide a landmark point to use for subsequent alignment with the mammogram.

The mesh was then fitted to the segmented data points using a nonlinear least-squares fitting process [1]. This process minimized the Euclidean distance between the skin and rib data points and their orthogonal projections onto the mesh. The fitted models (Fig. 1b) had root-mean-squared (RMS) errors between the fitted meshes and the segmented data that ranged from 1 to 2 mm. The tumor volumes for each patient were 13,040, 1,812, 1,468 and 8,210 mm^3, respectively.

2.3 Modeling Mammographic Compression

We then simulated mammographic compression for each breast model based on finite elasticity theory coupled with contact mechanics boundary constraints. Details of the techniques used in this study can be found in [2, 5]. All simulations were carried out using the software package CMISS[2].

The breast tissue was assumed to be incompressible, homogenous and isotropic, as described by the neo-Hookean constitutive relation $\Psi = c_1(I_1 - 3)$, where I_1 is the first principal invariant of the Lagrangian deformation tensor, and c_1 is the material stiffness parameter. Incompressibility was enforced by introducing kinematic constraints and defining a hydrostatic pressure field as a Lagrangian multiplier. Before applying compression, the unloaded configuration of the breast was determined (to remove the effect of gravity) using established methods [6].

[2] http://www.cmiss.org

In the absence of available data, the material stiffness of each breast was manually chosen; so the contour of the compressed breast model best matched the contour of the cranio-caudal mammogram.

The unloaded breast model was refined to ensure that adequate degrees of freedom were available to capture the breast deformation during compression, and also to ensure solution convergence of the model. The ribs and the compression pads were modeled using tricubic-Hermite elements, and the pads were curved at the edge that came into contact with the breast. Frictionless contact was applied between the breast and compression pads, while tied contact was used between the back of the breast model and the rib [5].

Nodes located at the sternum (i.e., the medial edge of the breast model) were fixed in the mediolateral direction during compression. The derivatives at the sternal face were fixed in the sagittal plane. Nodes at the axilla (i.e., the lateral edge of the breast model) were fixed in the anteroposterior direction to restrict the movement of breast tissue around the side of the body. The derivatives of the axillary nodes were also fixed in the anteroposterior plane. In addition, all patients had the inferior and superior nodal derivatives fixed in the axial plane.

The breasts were then compressed in the cranio-caudal direction until the thickness of the breast matched the breast thickness measurement given in the mammogram DICOM header (see Fig. 2). The compression pads were displaced simultaneously, giving two-sided compression. The compression pads were placed at an angle (rotated in the axial direction) to each of the patients, which was verified with clinicians, to ensure that all the breast tissue was captured between the pads.

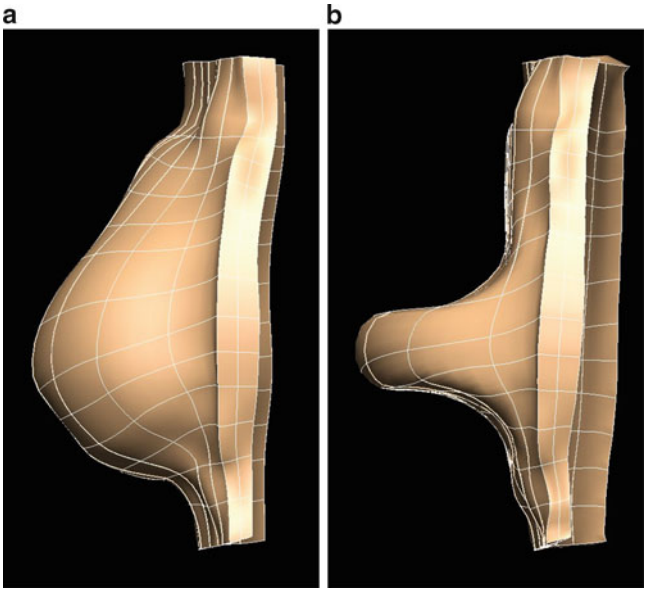

Fig. 2 Each patient's prone breast model (**a**) was compressed to match the breast thickness in the mammogram's DICOM header (**b**)

2.4 Mammogram Alignment and Model Validation

To evaluate the accuracy of our biomechanical modeling framework, the tumor locations in each breast model were compared with the actual tumor locations in the cranio-caudal mammograms. In order to test the tumor co-location accuracy, each mammogram image was aligned with each of the breast models.

As shown in Fig. 3, the nipple landmark on each breast model was first aligned with the nipple location on the mammogram. For each compressed breast model, the skin contour on the mammogram image was automatically segmented, and the RMS error calculated between these segmented data points and their orthogonal projections on the breast model surface. The RMS error was found for a range of mammogram image orientations by rotating the mammogram about the nipple landmark. The orientation that minimized the distance between the model and X-ray skin contours, from the nipple point to the sternum and the nipple point to the axilla, was taken as the optimal position.

The skin contour for the uncompressed prone models was visually aligned with the mammograms to best match the model and X-ray skin contour, reproducing what radiologists currently do in the clinic by eye.

Once the mammogram alignments were determined, the tumor locations in the breast models were quantitatively compared with the actual tumor locations in the mammogram images. This was done by calculating the Jaccard coefficient, which is the ratio of the area of intersection to the total area of the two overlapping areas [4], to give a similarity measure between the tumor areas in the models and the actual tumor areas given in the mammogram images.

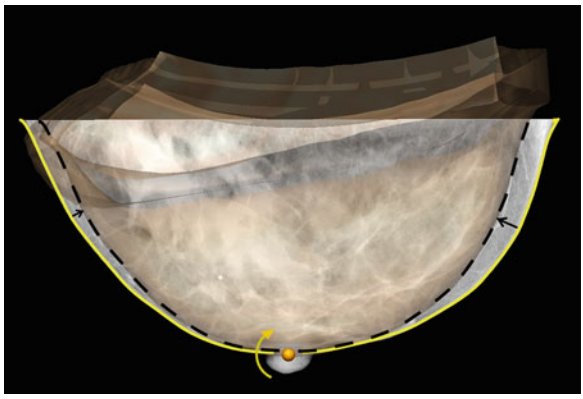

Fig. 3 The alignment of the cranio-caudal mammogram to the compressed breast model. The nipple landmark on the compressed model (*dot*) was first aligned with the nipple in the mammogram, and then rotated about the nipple point (*curved arrow*) to minimize the distance (*straight arrows*) between the mammogram skin contour and the compressed model skin contour

3 Results

Each patient's breast required a significant amount of compression to match the breast thickness in the mammogram, as detailed in Table 2. For the first patient, the distance between the compression pads reduced from 126.2 to 32.0 mm to give 75% compression. The other three patients required 52, 72%, and 57% compression to mimic the breast thickness during mammography. These significantly large compression simulations have not been possible before as noted by Tanner et al. [10], and is attributed to a more realistic representation of the boundary condition between the breast and rib surfaces.

Figure 4 shows the tumor location in the uncompressed prone model (Fig. 4a) and the compressed model (Fig. 4b) relative to the mammogram image. It is clear that even though the tumor location in the prone model overlays the tumor in the mammogram, the compressed model has provided a more reliable prediction of its location. For this model, the Jaccard coefficient increases from 43 to 75%.

The other three patients also showed an improvement in the tumor location predicted by the compressed models. Figure 5 shows the tumor locations in each model relative to that identified by clinicians in the mammograms. Table 3 details the tumor areas for each model and the corresponding Jaccard coefficients. Based on these similarity measures, it is evident that the compressed models provide a more reliable estimate of the tumor location.

Table 2 The amount of compression applied during mammography for each patient

Patient	1	2	3	4
Uncompressed dimension (mm)	126	133	88	111
Compressed dimension (mm)	32	64	25	48
% Compression	75	52	72	57

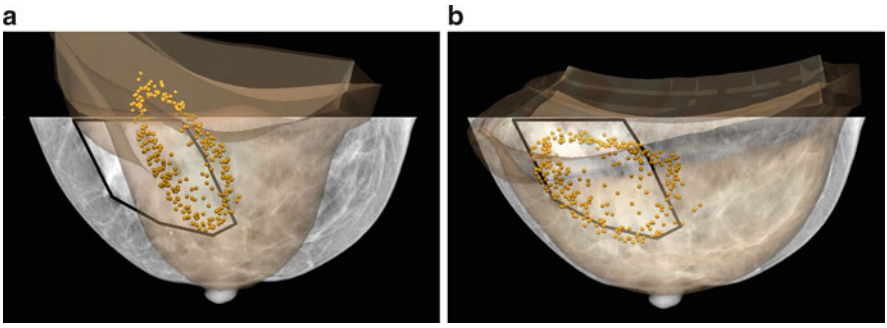

Fig. 4 The tumor locations (*dots*) (**a**) segmented from the uncompressed prone MR images and (**b**) predicted in the compressed breast compared with the tumor location identified by a clinician in the mammogram (*lines*)

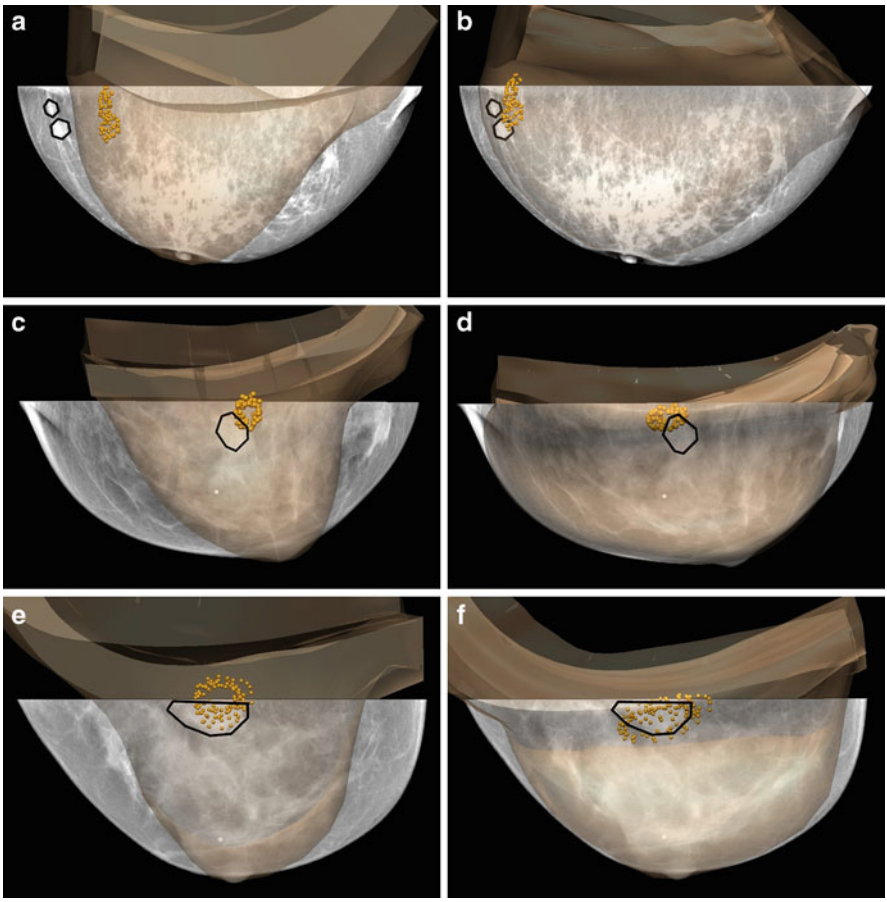

Fig. 5 Each patient's tumor location in the uncompressed prone model (*dots* in **a**, **c**, **e**) and the tumor location in the corresponding compressed model (*dots* in **b**, **d**, **f**), shown relative to the tumor locations in the corresponding cranio-caudal mammogram (*lines*)

Table 3 Tumor areas and Jaccard coefficients for each patient

Patient	1	2	3	4
Tumor area (mm^2)				
– Uncompressed prone model	2,230	245	108	342
– Compressed model	2,981	260	115	466
– Mammogram	2,569	126	118	286
Jaccard coefficient (%)				
– Before compression	43	0	5	40
– After compression	75	14	15	55

4 Discussion

This study quantitatively demonstrates the applicability of the modeling framework of Chung et al. for mapping tumor locations between clinical MR images and X-ray mammograms.

MR images obtained in the prone position were used to construct customized FE models of the patients' breasts, which simulated breast compression during cranio-caudal X-ray mammography. The models used realistic representations of the external loading conditions (i.e., plate-to-skin contact conditions, and lack of kinematic constraints at the skin surface) and the breast tissue interactions with the rib surface, and were able to simulate very high levels of compression (between 50 and 70%) as experienced by women during X-ray mammography. As such, this is the first demonstration in the literature of a modeling framework that has been able to simulate breast compression at these levels.

Comparison of the predicted region with the true location of the identified lesions in the MRI and mammograms has shown that the biomechanical models provided a better correspondence between the two images than a straight overlay of the uncompressed breast MRI on the X-ray mammogram. Although the increase in the Jaccard coefficient for the last three patients may be perceived as small, there was no overlap for the second patient before compression was applied, while after compression, it increased to 14%, which is a significant increase considering the two tumors were small. The last two patients had tumors near the center of the breast (close to the rib cage), thus the tumors did not move significantly during compression. Hence, even this modest increase in the Jaccard coefficient is also a marked improvement over the uncompressed images, which are what clinicians presently use for matching purposes.

While results are encouraging, there are a number of assumptions that require further investigation before the models can be used in a seamless fashion in the clinic. Since this is a retrospective study, we were limited to estimating the material stiffness parameter and the angle of the plates relative to the patient's body. We aim to develop techniques to more accurately estimate the angle of the plates during a mammography session using combinations of image processing and/or instrumentation. In future, we also aim to implement quantitative optimization methods to more accurately estimate the material stiffness parameter.

Another limitation is the assumption of a homogeneous, isotropic constitutive behavior of the internal breast tissues. We are currently developing techniques to estimate heterogeneous material properties in vivo in an effort to improve simulation predictions. In addition, we have recently developed techniques to combine nonrigid registration techniques to biomechanical model predictions of the breast [11]. In future, we intend to test this technique as a mammogram alignment method.

Nevertheless, despite current limitations, this study shows the use of an entirely biomechanical modeling approach (without assistance from nonrigid registration techniques or prescribed skin surface node displacements) to reliably map tumor locations. With additional developments to incorporate more anatomical detail, this modeling framework will be a useful tool in the clinic.

Acknowledgments We gratefully acknowledge financial support from the Foundation for Research Science & Technology. Martyn P. Nash is supported by a James Cook Fellowship administrated by the Royal Society of New Zealand on behalf of the New Zealand Government. Dr. Ralph Highnam provided valuable discussions.

References

1. Bradley, C.P., Pullan, A.J., Hunter, P.J.: Geometric modeling of the human torso using cubic Hermite elements. Annals of Biomedical Engineering, 25, 96–111 (1997)
2. Chung, J.H., Rajagopal, V., Nielsen, P.M., Nash, M.P.: Modelling Mammographic Compression of the Breast. MICCAI 11(2), 758–765 (2008)
3. Hipwell, J.H., Tanner, C., Crum, W.R., Schnabel, J.A., Hawkes, D.J.: A New Validation Method for X-ray Mammogram Registration Algorithms using a Projection Model of Breast X-ray Compression. IEEE Transactions on Medical Imaging, 26(9), 1190–1200 (2007)
4. Klein A., Andersson J., Ardekani B.A., Ashburner J., Avants B., Chiang M.C., Christensen G.E., Collins D.L., Gee J., Hellier P., Song J.H., Jenkinson M., Lepage C., Rueckert D., Thompson P., Vercauteren T., Woods R.P., Mann J.J., Parsey R.V.: Evaluation of 14 nonlinear deformation algorithms applied to human brain MRI registration. NeuroImage, 46(3), 786–802 (2009)
5. Laursen, T.A.: Computational Contact and Impact Mechanics. Springer, Berlin (2002)
6. Rajagopal, V., Chung, J.H., Bullivant, D., Nielsen, P.M., Nash, M.P.: Determining the finite elasticity reference state from a loaded configuration. International Journal for Numerical Methods in Engineering, 72(12), 1434–1451 (2007)
7. Rajagopal, V., Nielsen, P.M.F., Nash, M.P.: Modeling breast biomechanics for multi-modal image analysis - successes and challenges. WIRES Systems Biology and Medicine, 2(3), 293–304 (2009)
8. Rajagopal, V., Chung, J., Highnam, R.P., Warren, R., Nielsen, P.M.F., Nash, M.P.: Mapping Microcalcifications Between 2D Mammograms and 3D MRI Using a Biomechanical Model of the Breast. Computational Biomechanics for Medicine, Part 1, 17-28. Springer, New York (2010)
9. Ruiter, N.V., Stotzka, R., Müller, T., Gemmeke, H., Reichenbach, J.R., Kaiser, W.A.: Model-Based Registration of X-Ray Mammograms and MR Images of the Female Breast. IEEE Transactions on Nuclear Science, 53(1), 204–211 (2006)
10. Tanner, C., Hipwell, J.H., Hawkes, D.J.: Statistical Deformation Models of Breast Compressions from Biomechanical Simulations. In: Krupinski, E.A. (ed) Lecture Notes in Computer Science: IWDM, 5116, 426–432. Springer, Berlin (2008)
11. Lee, A., Schnabel, J.A., Rajagopal, V., Nielsen, P.M.F., Nash M.P.: Breast Image Registration by Combining Finite Elements and Free-Form Deformations. Lecture Notes in Computer Science, 6136, 736–743 (2010)

Cardiac Strain and Rotation Analysis Using Multi-scale Optical Flow

H.C. van Assen, L.M.J. Florack, F.F.J. Simonis, J.J.M. Westenberg, and G.J. Strijkers

Abstract Tagging MRI enables analysis of the local contractility of the cardiac left ventricle. It permits reliable assessment of local contractile dysfunction related to various cardiomyopathies. We present a multi-scale optical flow method, with Gabor filtering, for the extraction of dense motion fields from cardiac MR tagging. It is based on a multi-scale first order extension of the classical optical flow constraint equation enabling the extraction first order parameters like rotation and strain. A quantitative validation study based on the phantom proposed by Young et al. showed excellent performance. Furthermore, strain patterns are presented for one ischemic patient case with known wall motion abnormalities, and two volunteers. Patient circumferential strain abnormalities colocalize with enhanced areas in late-enhancement MRI. Rotation patterns are presented for the same patient and four volunteers. The rotation pattern described in the patient is strikingly different from that describing the volunteers.

Keywords Cardiac function · Strain · Optical flow · MR tagging · Medical image analysis

1 Introduction

Detailed analysis of regional left ventricular (LV) dynamic function is important in the diagnosis and characterization of various cardiomyopathies. In this chapter, we will focus on the analysis of LV strain and rotation from MR images with spatial modulation of magnetization (SPAMM, a.k.a. tagging) [2]. Tagging provides sufficient information to analyze disturbances in myocardial contractility, which have been identified as early signs in pathologies [7], and which remain hidden in

H.C. van Assen (✉)
Department of Biomedical Engineering, Eindhoven University of Technology, Eindhoven, The Netherlands
e-mail: h.c.v.assen@tue.nl

A. Wittek et al. (eds.), *Computational Biomechanics for Medicine: Soft Tissues and the Musculoskeletal System*, DOI 10.1007/978-1-4419-9619-0_10,

surface-based analysis techniques [5]. For tagging image analysis, we follow the rationale of [14] by the application of the optical flow constraint equation (OFCE), which was brought to the multi-scale framework by Florack et al. [10].

Since the OFCE assumes constant brightness of a pixel along its path, and SPAMM data typically suffer from tag fading due to the spin-lattice relaxation (expressed by T_1), our proposed method incorporates harmonic filtering in the Fourier domain using Gabor filters [12], similar to [6]. Thus, intrinsically conserved tag-phase information is used instead of brightness information. However, we take the sine of the tag-phase rather than the phase itself, to avoid spatial discontinuities in gray values.

Once the detailed motion information has been obtained, strain (Sect. 3.3) can be calculated. We use Stokes' theorem (Sect. 3.4) to calculate rotation in the cardiac slices robustly from dense first-order motion information.

This chapter is organized as follows. Section 2 briefly summarizes previous work. Section 3 explains our proposed method. Section 4 presents motion extraction evaluation based on a phantom data set, and strain and rotation results for a number of volunteers and a patient data set. Finally, Sect. 5 discusses the method and results and concludes the chapter.

2 Background

Tagging (SPAMM) patterns are inherent in the tissue, i.e., they deform along with the tissue, allowing analysis of the regional myocardial movement of the LV. This is to be contrasted to the imaging of the cardiac surfaces (e.g., with Cine MRI), which focuses mainly on global function (ejection fraction, cardiac output, etc.).

Suinesiaputra et al. [20] applied the multi-scale generalization [10] of the OFCE to track human hearts. Their method suffers from the fact that flow components tangential to iso-surfaces cannot be retrieved from data evidence, which was formalized in a "normal flow constraint." Dougherty et al. [8] also applied optical flow. They estimate global and local cardiac motion in a coarse-to-fine model-based technique. This technique encompasses a Laplacian filter to compensate for intensity and contrast loss in myocardial tags. Prince and McVeigh [17] developed an optical flow-based method that requires extensive prior knowledge of the relaxation times T_1, T_2, and the spin density D_0 of the myocardium. Sühling et al. [19] applied an optical flow-based technique to cardiac motion estimation from B-Mode echocardiograms. Their approach is moment-based and multi-resolution, and is similar to the one we propose algorithmically. However, their point of departure is the optical flow approach by Lucas and Kanade [15], while ours is [14].

For a review of MRI motion analysis protocols, the reader is referred to [3].

The HARP technique, which uses tagging combined with spectral filtering in Fourier space, overcomes tag fading by directly measuring *phase* information of the MR signal [16]. We choose to use a harmonic filtering method using Gabor filters [12] on *sinusoidal tag profiles*, and first-order Taylor expansion of multi-scale

optical flow. Thus, instead of tag-brightness information, tag-phase information is used which does not suffer from fading. We propose to extract the motion field by simultaneous analysis of perpendicularly encoded line tagged image sequences, assuming equal 2D motion in both.

3 Method

We aim for a regularization-free solution, but one that is not hampered by missing data evidence (i.e., the aperture problem of standard application of the optic flow constraint equation). The usual way to circumvent the aperture problem is to complement data evidence with prior knowledge, or by stipulating some smoothness hypothesis about the true motion field. However, there is no guarantee that a regularized solution is everywhere close to the physical motion field, and hypotheses are often unrealistic or not feasible.

It would be desirable if the tangential flow could be retrieved by adding further intrinsic evidence to the existing evidence. This is possible if one is in possession of a second independent recording of the same spatiotemporal region of interest. This can be achieved with the help of suitably chosen MR tagging patterns, i.e., with independent encoding directions.

3.1 Zeroth-Order Polynomial Expansion of the OFCE

Following this new rationale, we exploit the strength of the multi-scale OFCE by Florack et al. [10], while at the same time removing its shortcomings. The operational scheme for optical flow extraction makes use of a local polynomial expansion of the flow field (at each point).

Let f be shorthand for $f(x, y, t; \sigma, \tau)$, the scalar spatiotemporal image sequence as a function of position (x, y), time t, isotropic spatial scale $\sigma > 0$, and temporal scale $\tau > 0$. We denote its partial derivatives with respect to x, y, and t by self-explanatory subscripts. These are obtained by convolving the raw image sequence $f^0(x, y, t) = f(x, y, t; 0, 0)$ with a corresponding derivative of a normalized Gaussian,

$$\phi(x, y, t; \sigma, \tau) = \frac{1}{2\pi\sigma^2}\frac{1}{\sqrt{2\pi\tau^2}}\exp\left[-\frac{x^2+y^2}{2\sigma^2}-\frac{t^2}{2\tau^2}\right].$$

For a zeroth-order polynomial expansion scheme, and with f and g the independently encoded MR tagging image sequences, we must consider the following *single* system for *both* components of the physical motion field (u, v) simultaneously

$$\begin{cases} f_x u + f_y v + f_t = 0 \\ g_x u + g_y v + g_t = 0. \end{cases} \tag{1}$$

3.2 First-Order Polynomial Expansion of the OFCE

We propose to use a first order polynomial expansion scheme, where $U(x,y,t) = u + u_x x + u_y y + u_t t$, respectively, $V(x,y,t) = v + v_x x + v_y y + v_t t$, in which $u, u_x, u_y, u_t, v, v_x, v_y, v_t$ are eight local parameters (unknowns) of the horizontal, respectively, vertical *local* optical flow field approximation $U(x,y,t)$ and $V(x,y,t)$.

The relevant first order OFCE is then given by a nontrivial linear system (see [11] for details). Collsecting the unknowns in an 8-entry column vector **v**, and indicating the 8×8 coefficient matrix by **A**, and the inhomogeneous term by the 8-entry column vector **a**, we have

$$\mathbf{A}\,\mathbf{v} = \mathbf{a}\,. \tag{2}$$

For details of **A**, **v**, and **a**, see below. Optimal scales (σ, τ) are selected by minimizing w.r.t. the condition number for matrix **A**. Optimality should be interpreted in the sense of yielding maximally stable, not necessarily maximally accurate solutions; so experimental validation will be necessary (cf. Sect. 4).

$$\mathbf{A} = \begin{bmatrix}
f_x & f_y & f_{xt}\tau^2 & f_{yt}\tau^2 & f_{xx}\sigma^2 & f_{xy}\sigma^2 & f_{xy}\sigma^2 & f_{yy}\sigma^2 \\
f_{xt} & f_{yt} & f_x+f_{xtt}\tau^2 & f_y+f_{ytt}\tau^2 & f_{xxt}\sigma^2 & f_{xyt}\sigma^2 & f_{xyt}\sigma^2 & f_{yyt}\sigma^2 \\
f_{xx} & f_{xy} & f_{xxt}\tau^2 & f_{xyt}\tau^2 & f_x+f_{xxx}\sigma^2 & f_y+f_{xxy}\sigma^2 & f_{xxy}\sigma^2 & f_{xyy}\sigma^2 \\
f_{xy} & f_{yy} & f_{xyt}\tau^2 & f_{yyt}\tau^2 & f_{xxy}\sigma^2 & f_{xyy}\sigma^2 & f_x+f_{xyy}\sigma^2 & f_y+f_{yyy}\sigma^2 \\
g_x & g_y & g_{xt}\tau^2 & g_{yt}\tau^2 & g_{xx}\sigma^2 & g_{xy}\sigma^2 & g_{xy}\sigma^2 & g_{yy}\sigma^2 \\
g_{xt} & g_{yt} & g_x+g_{xtt}\tau^2 & g_y+g_{ytt}\tau^2 & g_{xxt}\sigma^2 & g_{xyt}\sigma^2 & g_{xyt}\sigma^2 & g_{yyt}\sigma^2 \\
g_{xx} & g_{xy} & g_{xxt}\tau^2 & g_{xyt}\tau^2 & g_x+g_{xxx}\sigma^2 & g_y+g_{xxy}\sigma^2 & g_{xxy}\sigma^2 & g_{xyy}\sigma^2 \\
g_{xy} & g_{yy} & g_{xyt}\tau^2 & g_{yyt}\tau^2 & g_{xxy}\sigma^2 & g_{xyy}\sigma^2 & g_{xyy}\sigma^2 & g_y+g_{yyy}\sigma^2
\end{bmatrix},$$

$$\mathbf{v} = \begin{bmatrix} u & v & u_t & v_t & u_x & v_x & u_y & v_y \end{bmatrix}^T \quad \text{and} \quad \mathbf{a} = -\begin{bmatrix} f_t & f_{tt} & f_{xt} & f_{yt} & g_t & g_{tt} & g_{xt} & g_{yt} \end{bmatrix}^T.$$

3.3 Calculation of Strain from a Flow Field

To calculate strain (a 2×2 tensor) as a measure of tissue deformation, we start with the construction of the velocity gradient tensor, using the first-order derivative structure of the motion field (u, v)

$$\mathbf{L} = \begin{bmatrix} u_x & u_y \\ v_x & v_y \end{bmatrix}. \tag{3}$$

By virtue of the chain rule, the relation between deformation and velocity gradient tensors is given by a first-order ODE

$$\dot{\mathbf{F}} = \mathbf{L}\,\mathbf{F}\,, \tag{4}$$

subject to an initial condition, viz. $\mathbf{F}(t = t_0, t_0) = \mathbf{I}$. The solution to (4) induces an expansion known as the matricant [9, 13]:

$$\mathbf{F}(t,t_0) = \mathbf{I} + \int_{t_0}^{t} \mathbf{L}(\xi)\mathrm{d}\xi + \int_{t_0}^{t} \mathbf{L}(\xi) \int_{t_0}^{\xi} \mathbf{L}(\sigma)\mathrm{d}\sigma d\xi + \cdots \tag{5}$$

Splitting the interval $[t_0, t]$ into n parts (frames in the MRI sequence), and using the property that

$$\mathbf{F}(t,t_0) = \mathbf{F}(t,t_1)\mathbf{F}(t_1,t_0) \qquad (t_0 < t_1 < t)\,, \tag{6}$$

for an infinitesimally narrow interval $[t_{k-1}, t_k]$ yields the following approximation

$$\mathbf{F}(t_k,t_{k-1}) = \mathbf{I} + \mathbf{L}(t_k^*)\Delta t_k + \text{h.o.t.}(\Delta t_k) \qquad t_{k-1} \le t_k^* \le t_k, \tag{7}$$

where "h.o.t." means *higher order terms*. Equations (6) and (7) lead to a representation in terms of a so-called multiplicative integral [13]:

$$\mathbf{F}(t,t_0) = \prod_{t_0}^{t} (\mathbf{I} + \mathbf{L}(\xi)\mathrm{d}\xi) \stackrel{\text{def}}{=} \tag{8}$$

$$\lim_{\Delta t_k \to 0} (\mathbf{I} + \mathbf{L}(t_n^*)\,\Delta t_n) \ldots (\mathbf{I} + \mathbf{L}(t_1^*)\,\Delta t_1)\,. \tag{9}$$

Finally, given the deformation tensor $\mathbf{F}$ obtained pointwise via the discretization scheme outlined above, we construct the Lagrange strain tensor:

$$\mathbf{E} = \frac{1}{2}(\mathbf{F}^{\dagger}\mathbf{F} - \mathbf{I}). \tag{10}$$

For rigid deformations we have $\mathbf{F}^{\dagger}\mathbf{F} = \mathbf{I}$, yielding $\mathbf{E} = 0$; thus, $\mathbf{E}$ captures the non-rigid part of tissue deformation. By pre- and postmultiplication of $\mathbf{E}$ with the unit vector $\hat{e}_{\mathrm{r}}$ in the radial or $\hat{e}_{\mathrm{c}}$ in the circumferential direction, or using both, one can extract the radial (E_{rr}), circumferential (E_{cc}), and shear (E_{cr}) strain components:

$$\begin{aligned} E_{\mathrm{rr}} &= \hat{\mathbf{e}}_{\mathrm{r}}^{\mathrm{T}}\,\mathbf{E}\,\hat{\mathbf{e}}_{\mathrm{r}}\,, \\ E_{\mathrm{cc}} &= \hat{\mathbf{e}}_{\mathrm{c}}^{\mathrm{T}}\,\mathbf{E}\,\hat{\mathbf{e}}_{\mathrm{c}}\,, \\ E_{\mathrm{cr}} &= \hat{\mathbf{e}}_{\mathrm{c}}^{\mathrm{T}}\,\mathbf{E}\,\hat{\mathbf{e}}_{\mathrm{r}}\,. \end{aligned} \tag{11}$$

To analyze part of the rigid motion, myocardial rotation may be calculated [1], as will be described in the next subsection.

3.4 Calculation of Rotation from a Flow Field

We invoke the generalized Stokes' theorem [18]: If R is an oriented piecewise smooth n-dimensional manifold (in our case $n = 2$), with oriented boundary ∂R, and ω is a smooth $(n-1)$-form on R, then

$$\int_R \mathrm{d}\omega = \oint_{\partial R} \omega\,. \tag{12}$$

Take $\omega = u\mathrm{d}x + v\mathrm{d}y$, with (u, v) the motion field, i.e., $\mathrm{d}\omega = (v_x - u_y)\,\mathrm{d}x \wedge \mathrm{d}y$ ($\wedge$ being the wedge product). Take R to be a ring, i.e., the interior of two concentric circles $\partial R = \partial R_{\mathrm{int}} \cup \partial R_{\mathrm{ext}}$, the orientation of which is deduced from the outward normal of the region R. Stokes' theorem then reduces to the so-called Green's theorem:

$$\int_R (v_x - u_y)\,\mathrm{d}x\mathrm{d}y = \oint_{\partial R} u\mathrm{d}x + v\mathrm{d}y\,. \tag{13}$$

For our disconnected boundary parts, this yields:

$$\int_R (v_x - u_y)\,\mathrm{d}x\mathrm{d}y = \oint_{\partial R_{\mathrm{ext}}} u\mathrm{d}x + v\mathrm{d}y - \oint_{\partial R_{\mathrm{int}}} u\mathrm{d}x + v\mathrm{d}y\,. \tag{14}$$

The interpretation of this result is net *rotation* of the vector field (u, v) inside region R, or equivalently net *circulation* of the vector field along its boundary. It can easily be shown that this yields twice the average rotation angle of the region R, which was also noted in [19]. The advantage of using Stokes' theorem is that boundary integrals (r.h.s. of 12–14) are computed in terms of more robust volume integrals (l.h.s. of 12–14).

4 Experiments and Results

4.1 Image Data

In order to evaluate the proposed method, a phantom inspired by Young et al. [21] was used, which consists of two concentric cylinders with gel in between. The inner cylinder is rotated in a controlled fashion (max. approximately 20°), and it describes a back and forth going sinusoidal rotation due to a crank in the set up. The outer cylinder is fixed (see Fig. 1). Gelatin was used as the medium between cylinders, 5.7 wt% standard cooking gelatin in water was used, which sticks to both cylinders, and thus deforms elastically. Phantom images were made on a 6.3T Bruker scanner using a C-SPAMM sequence, resulting in 12 frames describing a complete cycle. Scan parameters were: TE 2.4 ms, TR 40 ms, flip angle 15°, field-of-view 40 mm, slice thickness 1 mm, number of averages 4, tag distance 2 mm.

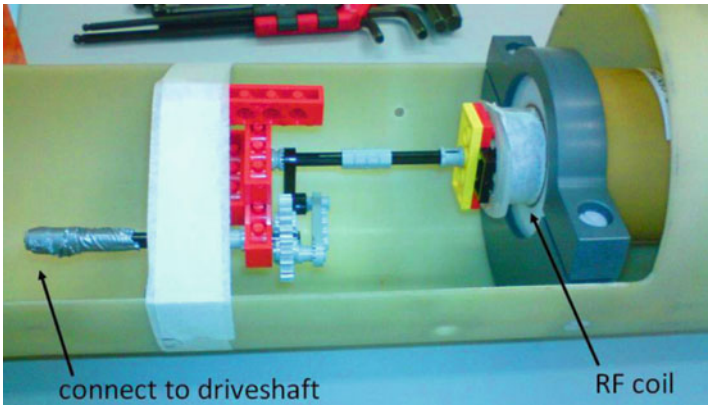

Fig. 1 Phantom imaging setup

Short-axis MR tagging data were acquired with a Philips Intera 1.5T scanner (Philips Healthcare, Best, Netherlands) from four healthy volunteers and one patient in a basal slice. The patient had a history of severe stenoses, and small infarction areas confirmed with late-enhancement MRI. A 2D multi-shot gradient-echo with Echo Planar Imaging (EPI factor 9) with breath-holding in end-expiration was used. Scan parameters were: TE 4.4 ms, TR 19 ms, flip angle 10°, field-of-view: 300 mm, scan matrix 128, acquisition voxel size $2.34 \times 2.68 \times 8\,\text{mm}^3$ reconstructed into $1.17 \times 1.17 \times 8\,\text{mm}^3$. Tagline spacing was 8 mm.

4.2 Results

For both the phantom and in vivo data, motion was extracted using (2). A rectangular grid was put on top of the undeformed phantom data, and lines were drawn on the undeformed in vivo data. Both the grid and the lines were automatically deformed along the extracted motion fields (see Figs. 2a and 3). From the phantom results, errors were quantified as angular error ε_ϕ and norm error $\varepsilon_\|$:

$$\varepsilon_\phi = \arccos\left(\frac{\mathbf{v}_{\text{est}} \cdot \mathbf{v}_{\text{true}}}{\|\mathbf{v}_{\text{est}}\|\|\mathbf{v}_{\text{true}}\|}\right), \tag{15}$$

$$\varepsilon_\| = \left(\frac{\|\mathbf{v}_{\text{est}}\|}{\|\mathbf{v}_{\text{true}}\|} - 1\right) \times 100\%, \tag{16}$$

where $\mathbf{v}_{\text{true}}$ is the known true velocity and $\mathbf{v}_{\text{est}}$ the estimated velocity resulting from our method. Errors were calculated per pixel of the phantom and the quantitative values were color-coded in Fig. 2b.

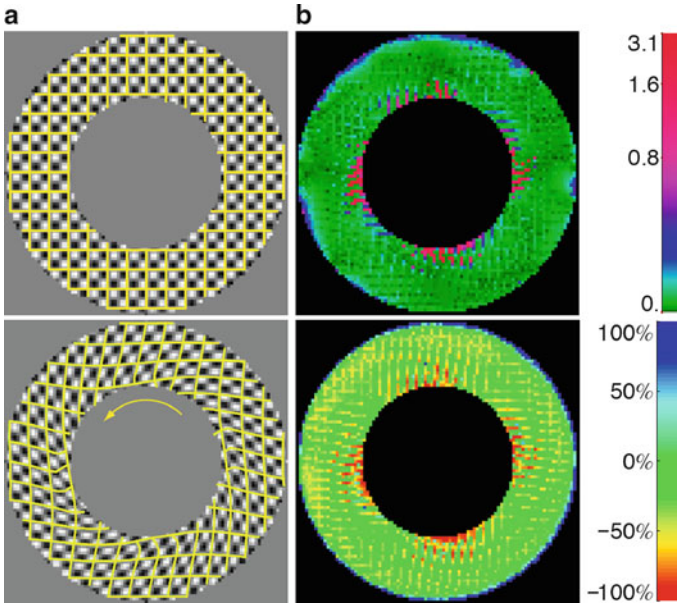

Fig. 2 (**a**) Overlay of rectangular grid on the first frame (*top*) and the grid deformed with the motion field on the eighth frame (*bottom*) of the gelatin phantom. (**b**) Angle error (radians, *top*) and norm error (%, *bottom*) distributions of a frame close to maximal deformation

Figure 3 shows the motion fields applied to straight lines (defined on the first frame) during systole for all subjects. Consequently, these lines move according to the extracted motion fields. This allows a visual assessment of the quality of the motion fields found. The lines in all frames show a good agreement with the underlying tagging patterns.

From the in vivo data, strain and rotation as a function of cardiac phase were calculated. Circumferential and radial strains are presented in Fig. 4 and rotation plots in Fig. 5. Both figures show a lack of rotation in the early systolic phase for the patient. The circumferential strain pattern of the patient exhibited abnormalities that strongly correlated with enhanced areas in late-enhancement MRI.

5 Discussion and Conclusion

Cardiac motion and myocardial deformation analysis is a promising method by which abnormalities in both active and passive tissue function can be found. We presented a novel multi-scale first-order optical flow method for detailed cardiac motion extraction. We have shown that with the generalized Stokes' theorem, one can robustly calculate myocardial rotation, an important parameter for early diagnosis of ischemic heart disease. Furthermore, our method was able to show a difference

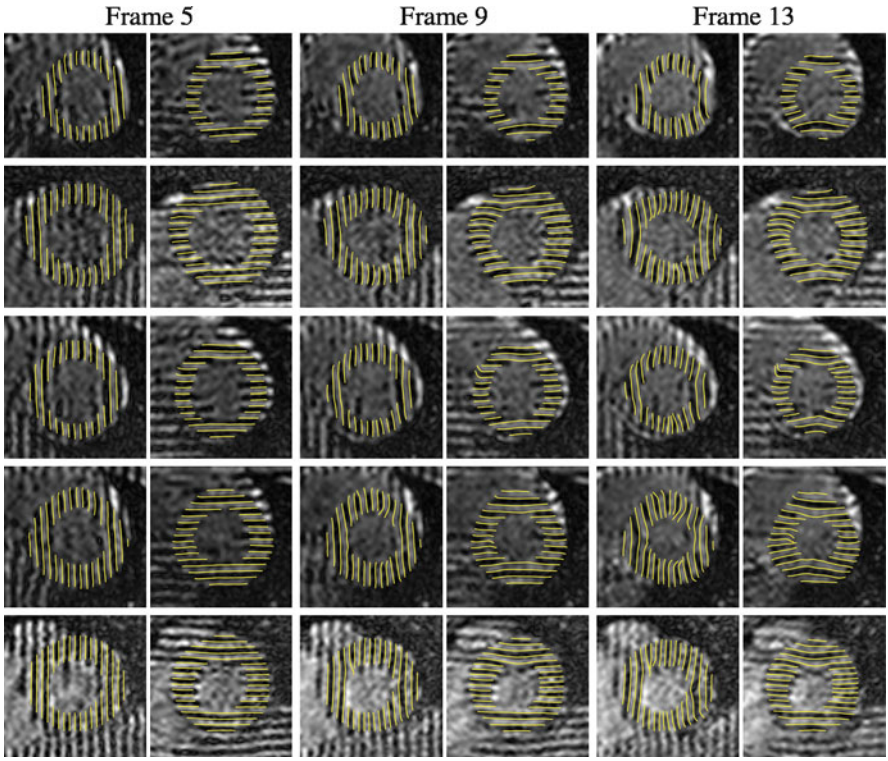

Fig. 3 Motion extraction results. *Lines* indicate myocardial deformation. *Straight lines* are defined on the first frame of five different subjects (*rows*). Next, the lines are deformed with the motion field of each subject extracted using (2). This allows visual assessment of the quality of (a sparse subset within) the (dense) motion field. *Rows 1–4*: Four different volunteers. *Row 5*: Patient data. Phases shown are {5, 9, 13} (systole), basal slice

in rotation between a healthy heart and one with a history of small infarction areas and suffering from ischemia. Finally, it showed abnormal locations in strain patterns corresponding to bright areas in late-enhancement MRI. Therefore, our method is a promising step toward cardiac function analysis without the use of contrast agents, currently used for, e.g., delayed-enhancement imaging of infarction areas.

From the quantitative evaluation with the phantom setup (see Fig. 2b), it can be seen that both ε_{ϕ} and $\varepsilon_{\|}$ under 0°, 90°, 180°, and 270° are larger at the endocardial border than at other locations. This is possibly due to the discontinuity in the tags (transition from gel to air) and due to the fact that in those locations motion is parallel to one of the tag directions, making the system $\mathbf{A}$ in 2 conditioned worse. A solution to this may be incorporation of more image sequences with more independent tag directions, e.g., separated by only 45° instead of 90°. The results shown in Fig. 3 show minor errors at a few locations at the endo- and/or epicardial border. This is due to the discontinuity in the tags at the myocardial borders. Tagging data are less reliable at these borders. A solution could be the combination of tagging

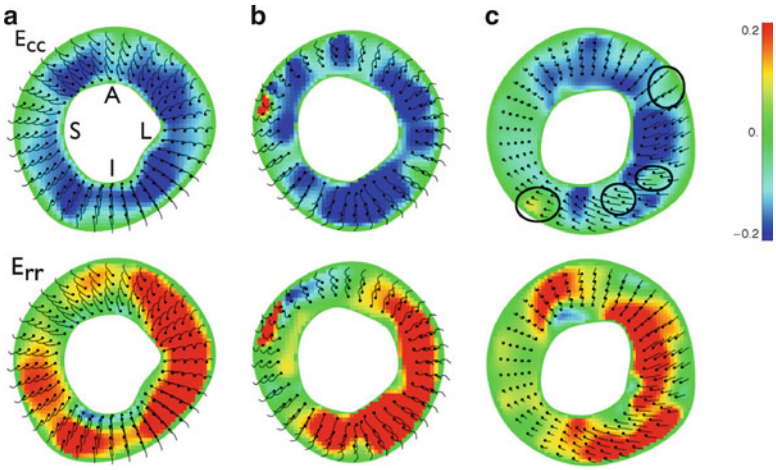

Fig. 4 Circumferential strains (E_{cc}) and radial strains (E_{rr}) of two volunteers (**a**, **b**) and the patient (**c**) of a frame close to end systole. Overlays are trajectories of the points since end diastole. These clearly show presence of rotation in the volunteers and lack of rotational motion in the patient data (see also Fig. 5). Ellipses (**c**, *top*) indicate locations with both enhancement in late-enhancement MRI and deviations in circumferential strain. The septum of the patient remains stationary, which was confirmed by a cardiologist (*A* anterior; *S* septal; *L* lateral; *I* inferior)

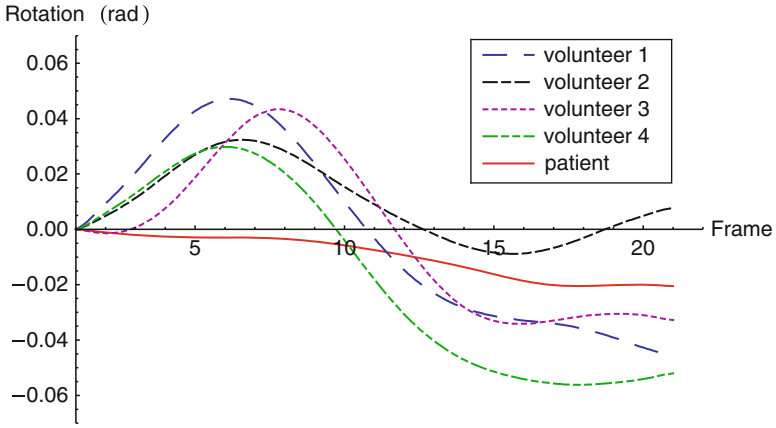

Fig. 5 Rotation (rad) of the basal slices for four healthy volunteers (*dashed/dotted*) and a patient (*solid*). As can be seen in Fig. 4, the patient heart lacks rotation in the early contraction phase

analysis for internal myocardial motion and deformation, and cine analysis (segmentation) for the assessment of myocardial surface motion.

Cardiac LV motion is complex and intrinsically 3D. By analyzing 2D short-axis images, the through-plane motion component cannot be determined. Taking into account the third dimension will lead to more reliable results. However, true 3D

MR tagging acquisition is a topic of ongoing research itself, and not widely available yet. From an implementation point of view, the extension of our method to 3D is straightforward. However, this would result in a system of 15 equations, and the unknowns would span a 15-entry column vector. Computationally this would become much more expensive though, as extra scale parameters would enter the system, resulting in many more combinations of spatial and temporal scales to be explored for an optimal set, and a series of much larger data *volumes* would form the input instead of the series of frames used now. Parallelization and possibly implementation on dedicated hardware may become mandatory to limit computation time. This is a current topic of further research. In earlier work though, we presented the analysis of 3D MR tagging using *sparse sets* of multi-scale feature points [4].

References

1. van Assen HC, Florack LMJ, Westenberg JJM, ter Haar Romeny BM (2008) Tuple image multi-scale optical flow for detailed cardiac motion extraction: application to left ventricle rotation analysis. In: Hamarneh G, Abugharbieh R (eds) Proc. MICCAI 2008 workshop on Analysis of functional Medical Images, pp 73–80, URL bisicl.ece.ubc.ca/functional2008/
2. Axel L, Dougherty L (1989) MR imaging of motion with spatial modulation of magnetization. Radiology 171(3):841–845
3. Axel L, Montillo A, Kim D (2005) Tagged magnetic resonance imaging of the heart: a survey. Medical Image Analysis 9(4):376–393
4. Becciu A, van Assen H, Florack L, Kozerke S, Roode V, ter Haar Romeny B (2009) A multi-scale feature based optic flow method for 3D cardiac motion estimation. In: Tai XC, Morken K, Lysaker M, Lie KA (eds) SSVM 2009, Springer Verlag, Berlin, Lecture Notes in Computer Science, vol 5567, pp 588–599
5. Chandrashekara R, Mohiaddin R, Rueckert D (2005) Comparison of cardiac motion fields from tagged and untagged mr images using nonrigid registration. In: Frangi AF, Radeva P, Santos A, Hernandez M (eds) FIMH 2005, Springer Verlag, Berlin, Lecture Notes in Computer Science, vol 3504, pp 425–433
6. Chen T, Chung S, Axel L (2007) Automated tag tracking using gabor filter bank, robust point matching, and deformable models. In: Sachse FB, G S (eds) FIMH 2007, Springer Verlag, Berlin, Lecture Notes in Computer Science, vol 4466, pp 22–31
7. Delhaas T, Kotte J, van der Toorn A, Snoep G, Prinzen FW, Arts T (2004) Increase in left ventricular torsion-to-shortening ratio in children with valvular aorta stenosis. Magnetic Resonance in Medicine 51:135–139
8. Dougherty L, Asmuth JC, Blom AS, Axel L, Kumar R (1999) Validation of an optical flow method for tag displacement estimation. IEEE Transactions on Medical Imaging 18(4):359–363
9. Florack L, van Assen H (2010) A new methodology for multiscale myocardial deformation and strain analysis based on tagging mri. International Journal of Biomedical Imaging Art. no. 341242
10. Florack L, Niessen W, Nielsen M (1998) The intrinsic structure of optic flow incorporating measurement duality. International Journal of Computer Vision 27(3):263–286
11. Florack LMJ, van Assen HC, Suinesiaputra A (2007) Dense multiscale motion extraction from cardiac cine MR tagging using harp technology. In: Niessen WJ, Nielsen M (eds) Proc. Mathematical Methods in Biomedical Image Analysis. Proceedings of the Eleventh IEEE International Conference on Computer Vision
12. Gabor D (1946) Theory of communication. J IEE 93(26):429–457

13. Gantmacher FR (2001) The Theory of Matrices. American Mathematical Society
14. Horn BKP, Schunk BG (1981) Determining optical flow. Artificial Intelligence 17:185–203
15. Lucas BD, Kanade T (1981) An iterative image registration technique with an application to stereo vision (darpa). In: Proceedings of the 1981 DARPA Image Understanding Workshop, pp 121–130
16. Osman NF, Kerwin WS, McVeigh ER, Prince JL (1999) Cardiac motion tracking using cine harmonic phase (harp) magnetic resonance imaging. Magnetic Resonance in Medicine 42(6):1048–1060
17. Prince JL, McVeigh ER (1992) Motion estimation from tagged MR image sequences. IEEE Transactions on Medical Imaging 11(2):238–249
18. Spivak M (1965) Calculus on Manifolds. W. A. Benjamin, New York
19. Sühling M, Arigovindan M, Jansen C, Hunziker P, Unser M (2005) Myocardial motion analysis from b-mode echocardiograms. IEEE Transactions on Image Processing 14(4):525–536
20. Suinesiaputra A, Florack LMJ, Westenberg JJM, ter Haar Romeny BM, Reiber JHC, Lelieveldt BPF (2003) Optic flow computation from cardiac MR tagging using a multiscale differential method: a comparative study with velocity–encoded MRI. In: Ellis R, Peters T (eds) Proc MICCAI, Springer Verlag, Berlin, Lecture Notes in Computer Science, vol 2878, pp 483–490
21. Young AA, Axel L, Dougherty L, Bogen DK, Parenteau CS (1993) Validation of tagging with MR imaging to estimate material deformation. Radiology 188(1):101–108

Part II
Computational Biomechanics of Musculoskeletal System and Its Tissues. Generation of Patient-Specific Finite Element Meshes

Computational Foot–Ankle–Knee Models for Joint Biomechanics and Footwear Design

Ming Zhang

Abstract Understanding complex human musculoskeletal systems requires an enormous amount of experimental and computational studies. The computational modeling combining anatomic, physiologic and engineering analyses can create a virtual human body to study various activities in a normal and pathological condition. Combining the virtual human body with some kinds of mechanical analyses showed strong potentials in understanding of musculoskeletal biomechanics.

Modeling of human joints, such as foot–ankle–knee are most challenging, due to very complex structures. Information on the internal structures as well as foot-support interfacial load transfer during various activities is useful in enhancing our biomechanical knowledge for foot support design and surgical planning. We develop computational models as a digital foot-ankle, which can be used to understand joint biomechanics and design proper foot supports and implant. Three-dimensional geometrically accurate finite element (FE) models of the human foot–ankle–knee structures were developed from 3D reconstruction of MR images of subjects. The foot FE model consists of 28 separate bones, 72 ligaments and the plantar fascia, embedded in a volume of encapsulated soft tissue. The main bone interactions were simulated as contact deformable bodies. The analyses took into consideration the nonlinearities from material properties, large deformations, and interfacial slip/friction conditions. A series of experiments on human subjects and cadavers were conducted to validate the model measurements on in terms of plantar pressure distribution, foot arch and joint motion, plantar fascia strain under different simulated weight-bearing, and orthotic conditions of the foot. The validated models can be used for parametrical studies to investigate the biomechanical effects of tissue stiffness, muscular reaction, surgical and orthotic performances on the foot–ankle complex.

M. Zhang (✉)
Department of Health Technology and Informatics, The Hong Kong Polytechnic University, Hong Kong, China
e-mail: htmzhang@inet.polyu.edu.hk

A. Wittek et al. (eds.), *Computational Biomechanics for Medicine: Soft Tissues and the Musculoskeletal System*, DOI 10.1007/978-1-4419-9619-0_11,

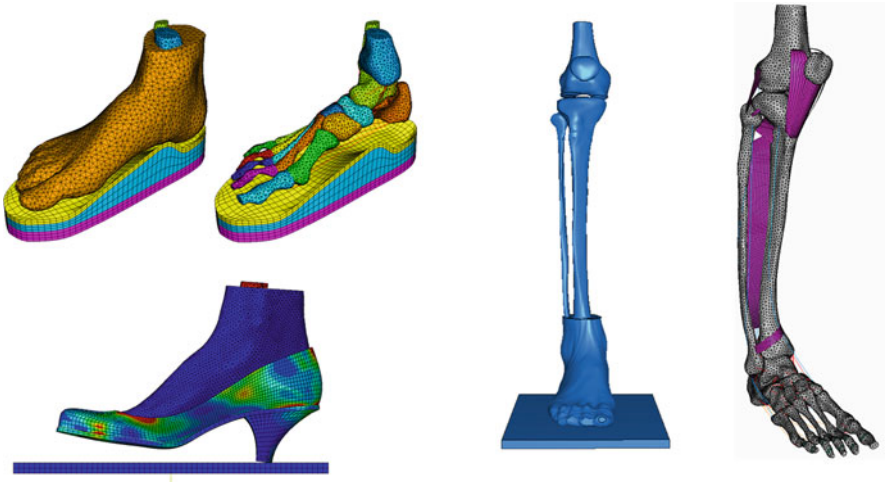

Acknowledgments This project is supported by Research Grant Council of Hong Kong (GRF Project nos. PolyU5331/07E, PolyU5352/08E).

Segmentation of Skeletal Muscle Fibres for Applications in Computational Skeletal Muscle Mechanics

O. Röhrle, H. Köstler, and M. Loch

Abstract We present a semi-automatic method to segment single muscle fibres from skeletal muscle cross-section images. As a pre-processing step we apply different filters depending on the type of the manually selected image region to obtain an edge image. Then we detect circles within the image by a circular Hough transform as initial rough approximation to the muscle fibre slices. This approximation is improved by active contours, where the circles are deformed to fit to the specific shape of the muscle fibres. The implementation of the segmentation method was done in Matlab. We show qualitative and quantitative results for different image regions and also outline a straight-forward method to combine several slices to obtain a 3D piece of a muscle fibre, which forms the input to an electro-mechanical skeletal muscle model.

Keywords Skeletal muscle · High-resolution imaging · Segmentation of skeletal muscle fibres · Active contour

1 Introduction and Motivation

A skeletal muscle is a complex and hierarchical construct of connective tissue and muscle fibres. Each of the muscle fibres consists of sarcomeres connected in series, which are the contractile machinery of a skeletal muscle. Further, each muscle fibre is surrounded by a thin layer of connective tissue called endomysium. Groups of muscle fibres (sometimes thousands – depending on size and function of the muscle) are wrapped within a thin layer of connective tissue called the perimysium to form a muscle bundle, or fascicle. One skeletal muscle can then be defined as the amalgamation of fascicles joining into a tendon at each end. There have been many mathematical models developed for skeletal muscles in the past. Mathematical

O. Röhrle (✉)
Institut für Mechanik (Bauwesen), Universität Stuttgart, Pfaffenwaldring 7,
70569 Stuttgart, Germany
e-mail: roehrle@simtech.uni-stuttgart.de

A. Wittek et al. (eds.), *Computational Biomechanics for Medicine: Soft Tissues and the Musculoskeletal System*, DOI 10.1007/978-1-4419-9619-0_12,

models of skeletal muscles can generally be categorised into models (a) that were specifically developed to represent and investigate electro-physiological cellular properties, e.g. [1, 2], (b) task-specific models that aim to represent mechanical function based on generalised parameters, e.g. [3], (c) and models that focus on the kinematics and the mechanical aspects of the musculoskeletal system, e.g. 1D models Hill-type models, e.g. [4], or continuum-based three-dimensional models, e.g. [5–10]. The model proposed by Röhrle et al. [9, 10] captures the electro-mechanical principles of skeletal muscle tissue and is currently the most advanced 3D continuum-mechanical skeletal muscle model. This model couples a detailed biophysically based electro-physiological cell model, [2], with a 3D continuum-based FE model of muscle mechanics and accounts for the unique manner in which skeletal muscles are activated, specifically the fact that neighbouring fibres are electrically isolated and can act independently of each other.

As the fibre distribution and the knowledge gain based on a skeletal muscles micro-mechanical structure and function (on the level of a few interconnected fibres) have many implications for the overall mechanical behaviour of skeletal muscle tissue, there is a great need for building up a detailed and anatomically accurate micro-structural FE model. The great challenge is to perform a segmentation process that would allow obtaining the skeletal muscle fibres from high-resolution images. The data of such a segmentation process leads to many seminal applications in the field of skeletal muscle mechanics.

For example, generating a full 3D FE model of a part of the muscle tissue allows one to perform a detailed FE analysis in order to investigate the mechanisms of inter-force transduction and its implication on macroscopic constitutive behaviour on the scale of the entire muscle or musculoskeletal systems. This is of particular importance as 3D continuum-based FE skeletal muscle models have many advantages as they can include complex anatomical or physiological properties like the muscle fibre distribution. One of the drawbacks of 3D (continuum-mechanical) models is the lack of research on proper constitutive laws. This applies likewise to the passive (inactive) and contractile (active) components describing the overall material behaviour of skeletal muscles. While the passive constitutive laws can be improved by fitting its parameters to data obtained, e.g. from indention or shear tests, experiments aiming to obtain experimental data for the active component are much more challenging, if feasible at all. This is mainly due to a skeletal muscle's complex way of independently activating single fibres and its ability to fatigue. Therefore, the active component in state-of-the-art continuum-mechanical-based skeletal muscle models is achieved by adding an additional active stress component just to the along-the-fibre component of the passive stress tensor (e.g. [7–10]). This modelling limitation applies for the mechanical and electro-mechanical models likewise. Further, extracting the midlines of the segmented muscle fibres provides muscle fibre distribution data of a specific muscle that can then be used, in a straight-forward manner, as anatomically realistic input to electro-mechanical frameworks of skeletal muscle modelling, e.g. the one proposed in [9] and [10].

This chapter focuses on the creation of a detailed skeletal muscle replication. The main task consists of reliable and automatic segmentation using circular Hough transformation and active contours for detecting muscle fibres. A very important

aspect is hereby to recognise fibres, which are placed very close to each other, based on a sequence of cross-sectional images of a skeletal muscle. Therefore, various filter methods and suitable segmentation processes are used in order to depict the contours of the muscle fibre contours and to prepare them for further computational procedures. The results of such a segmentation processes are analysed for practical exertion, quality, error ratio and computational time, as well as its potential to extend it to the third dimension. The chapter concludes with future prospect, limits and improvements of the proposed segmentation method.

2 Extended Volume Imaging

To obtain accurate fibre distributions and to build up a detailed micro-mechanical model, high-resolution micro-structural images of an entire extensor digitorum longus (EDL) of a mouse were obtained. After dissecting the EDL and stretching it to its optimal length, the entire muscle was embedded within resin before it was imaged using the Welcome Trust extended-volume imaging system developed at the Auckland Bioengineering Institute at The University of Auckland, New Zealand. The imaging process resulted in high-quality cross-sectional images of the entire muscle (see Fig. 1 for an example of a representative cross-sectional image). The images have a 1-µm in-plane resolution. In the longitudinal direction, cross-sectional images have been taken at least every 50 µm. In the middle section of the muscle, cross-sectional images were obtained at a much higher density, viz. a 1-µm

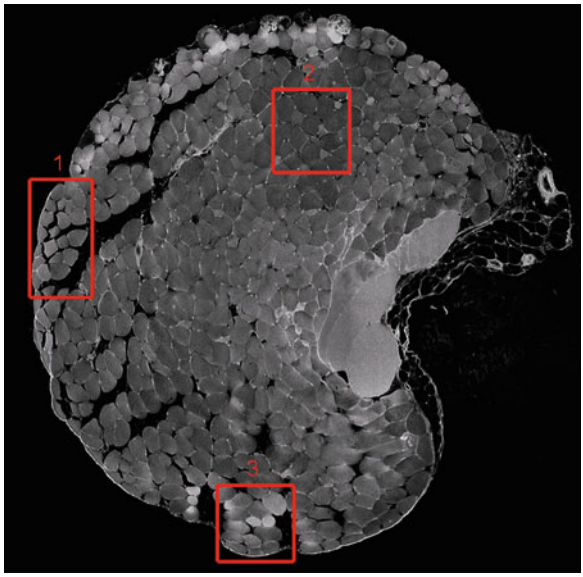

Fig. 1 Muscle slice with marked regions

slice distance. This was achieved over a length of 350 µm. Hence, one obtains for the middle section a 1-μm^3 voxel resolution (compared to about 2.4 µm sarcomere length and a 10–100-µm fibre diameter) while still obtaining enough information to structurally reconstruct the remaining parts of the entire muscle. The imaging protocol and the extended-volume imaging setup is essentially the same as it has previously been used by Sands et al. [11] for cardiac muscle tissue.

3 Segmentation Process

The segmentation of biological tissue is especially difficult, because most standard segmentation methods rely on sharp contrasts at the edges of objects which are often not present in micro-structural images. In our context, a clear boundary between neighbouring muscle fibres is, at times, not visible. There are several ways to circumvent this problem. Either one improves the images/imaging, e.g. by colouring the cells or by increasing the resolution during image acquisition, or one pre-processes the images to enhance its quality and include additional a priori knowledge on size and shape of objects. We will follow the latter approach and apply a semi-automatic method to segment the skeletal muscle fibres within cross-sectional images.

The three main steps of our segmentation process are pre-filtering (Sect. 3.1), circle detection as initial rough approximation to the shape of a fibre (Sect. 3.2), and finding the final contours of the muscle fibres by the method of active contours (Sect. 3.3). We demonstrate this segmentation method in three representative regions exhibiting different image quality.

3.1 Pre-Filtering

In the first step, pre-filtering is used to reduce noise and to produce a gradient image required to control the active contours. The quality of the pre-filtering is therefore essential for the next steps. While for Region 1 a standard Sobel-filter [12] and thresholding is enough for an acceptable result, we need to apply an additional dilatation, Canny Edge Filter, and a median filter to the other two regions. The results of the pre-filtering process are depicted in Fig. 2. While Region 1 gives very good results, Region 2 presents a greater challenge as one can hardly separate different cells due to their weak boundaries.

3.2 Hough Transform

The circle detection is done by a circular Hough transform [13]. Figure 3 shows the circles detected by this method. They serve as input for the initialisation step of the

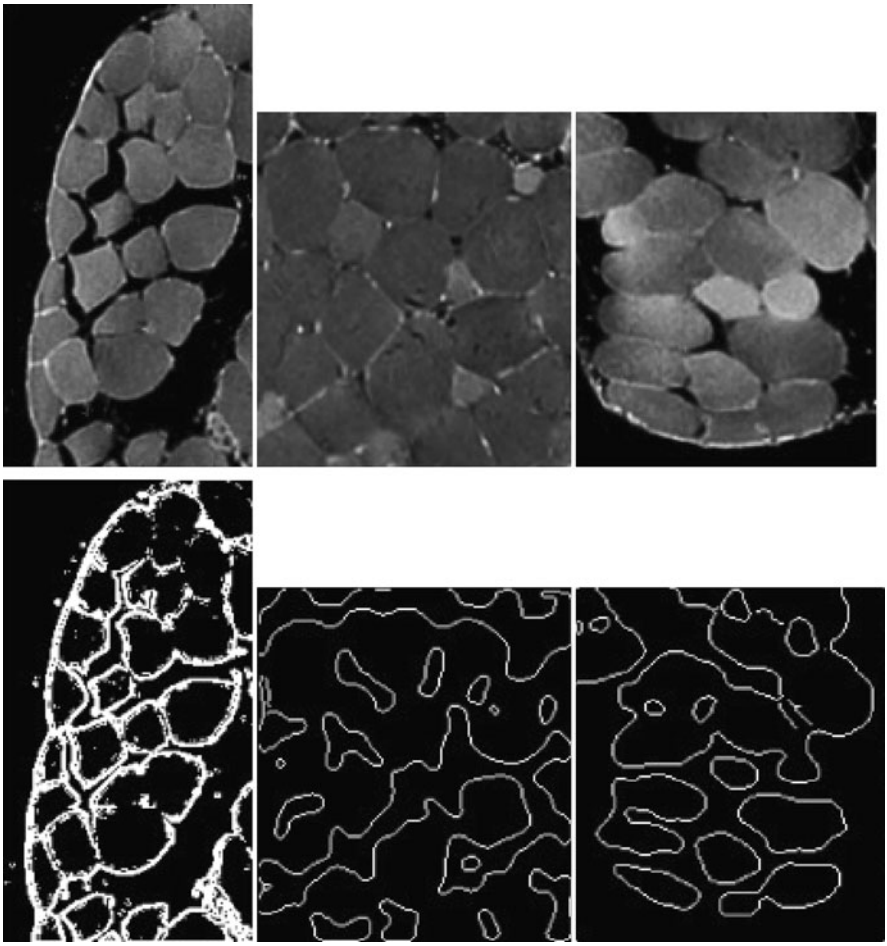

Fig. 2 Pre-filtering results for the three marked regions from Fig. 1

active contours method. Ideally, the number of circles should be equivalent to the number of cells and the center of the circles should approximately correspond to the center of the cells. Again, good results are obtained for Region 1, while the results in the other two regions are not fully satisfying.

3.3 Active Contours

Active contours [14] or snakes describe the contour of an object by an explicit deformable curve c. In an iterative process, the initial curve, in our case the detected

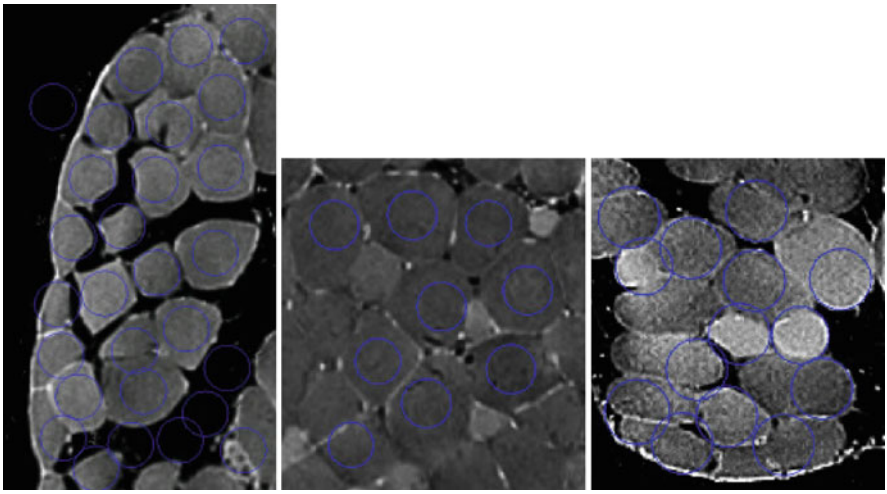

Fig. 3 Results of circle detection for the three marked regions from Fig. 1

circle, is deformed until a certain stopping criterion is reached. Mathematically, this can be formulated as a minimisation problem that minimises the energy term

$$E(c) = \underbrace{\frac{1}{2}\int_0^1 w_1 \left|\frac{\partial c}{\partial s}\right|^2 + w_2 \left|\frac{\partial^2 c}{\partial s^2}\right|^2 \mathrm{d}s}_{S(c)} + \underbrace{\int_0^1 P(c(s))\mathrm{d}s}_{P(c)}$$

consisting of an inner energy $S(c)$ and an outer energy $P(c)$ [15]. The inner energy, $S(c)$, describes the shape of the active contour using information on the contour's length and curvature, the positive coefficients w_1 and w_2 control the elasticity and stiffness of the snake. $P(c)$ holds a priori information about the image itself, e.g. image edges. In order to compute the deformation corresponding to the minimal energy, we compute the Euler–Lagrange equations corresponding to E by variational calculus, which are then discretised by finite volumes and solved numerically [16, 17].

Figure 4 visualises the computed contours for the three marked regions from Fig. 1. Since the deformation process of the initial circles stops at image edges, the quality of the segmentation highly depends on the quality of the gradient images as previously mentioned.

3.4 Post-Processing

In a post-processing step, we apply an additional thresholding to the detected muscle fibres. This enables us to remove detected non-fibre cells like the black areas in the lower right of Region 1 (Fig. 5).

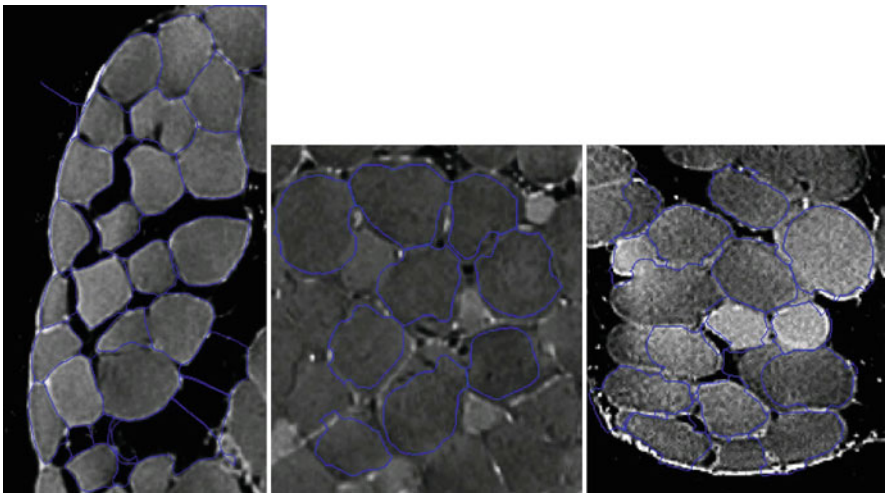

Fig. 4 Segmented muscle fibres after applying active contours for the three marked regions from Fig. 1

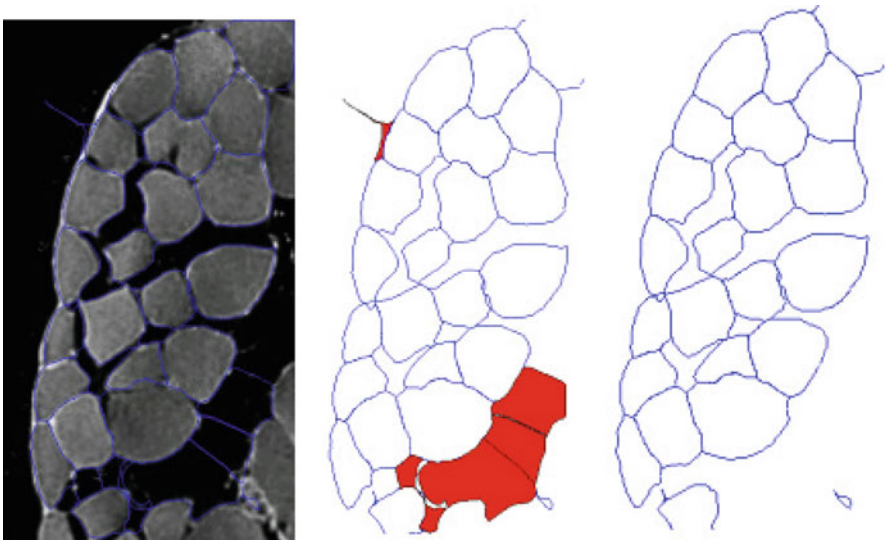

Fig. 5 (*Left*) Result mapped to original image; (*middle*) result with marked non-fibre regions; (*right*) result after removing non-fibre regions

4 Results and Discussion

4.1 Quantitative Segmentation Error

During the segmentation process several error types occur. The different filters lead to a loss of information, the centres of the circles are not detected without a certain error and also the active contours only approximate the real contour. To obtain a quantitative measure for the segmentation error, we select in Fig. 6 one single muscle fibre and compute its area by manually segmenting it and counting the number of pixels within it (1,304 pixels). After pre-filtering, the same fibre consists of 1,050 pixels in the gradient image resulting in a loss of 19.5% of the area. The contour found by the active contours method has 1,273 pixels. This equals to 97.6% of its initial area. This result of course differs for other fibres, but provides a certain measure and confidence for the applicability of our proposed segmentation process.

4.2 Runtime of the Algorithm

All algorithms within the segmentation process have linear complexity, i.e. the algorithm requires a constant number of operations per pixel (also the active contours if one uses a suitable multigrid solver). Due to our MATLAB implementation of the entire segmentation process, we do expect a significant speed-up once this algorithm is implemented using a parallel and optimised C or C++ code. Nevertheless, the MATLAB runtimes are measured on an Intel Core2Duo processor with

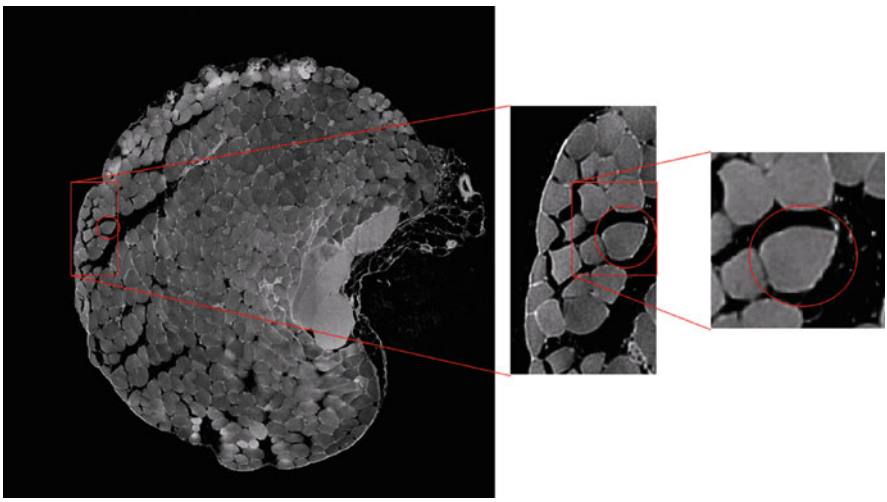

Fig. 6 Marked fibre for measurement of segmentation error

2.1 GHz and 2 GB RAM. The whole segmentation took for Region 1 (263 × 143 pixels) 12.76 s. Hereby, 95% of the total time was spent on computing the active contour. The pre-filtering process took 0.36 s and the circle detection 0.27 s. Similar results are obtained for the other two regions (Region 2: 181 × 161 pixels, 8.22 s; Region 3: 180 × 154 pixels, 6.24 s, respectively). If one assumes an optimised implementation on current hardware then it is surely possible to segment an image in less than 1 s.

4.3 Extension to 3D

To extract the 3D muscle fibre contour we simply run our algorithm on several 2D cross-section images and then merge the results. The whole process took 36.7 s for a total of ten images. A cut-out of three of the ten images showing the initial circle and the final contour for the muscle fibre can be seen for each of the respective cross-sectional images in Fig. 7.

4.4 Discussion

As previously mentioned, the quality of the segmentation process depends on several factors. Currently, the user has to adapt parameters for each of the steps (pre-filtering, circle detection, and active contours) in order to achieve the best possible result. However, the problem of low contrast at edges remains in certain regions and prevents a proper segmentation of the corresponding muscle fibres.

Nevertheless, the data obtained through the segmentation process can have a seminal impact on skeletal muscle modelling. For example, based on the midpoints of the segmented cells in a sequence of images, one is able to construct a detailed and anatomically accurate description of the skeletal muscle fibre distribution within

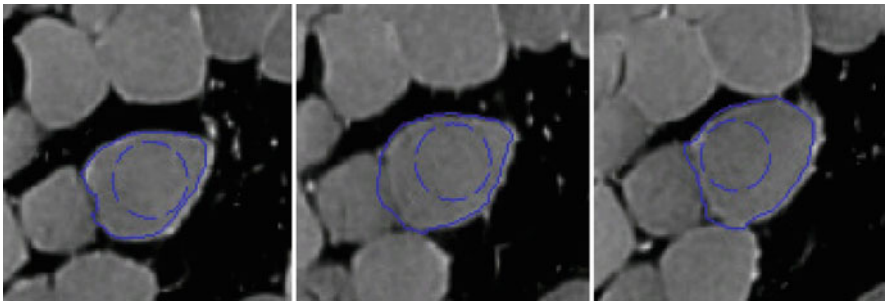

Fig. 7 Initial and final contours for three of the ten cross-sections used to segment a 3D muscle fibre

the EDL. This combined with an electro-mechanical framework of skeletal muscle modelling and principles of muscle fibre recruitment, provides a unique important set of data to carry out basic research on many application-driven problems, e.g. applications in the field of functional electrical stimulation.

Moreover, the segmentation provides the necessary data for computational models using micro-structurally based models on the skeletal muscle fibre scale. Such models could be used to generate in silico data or to provide a deeper understanding of mechanical properties of inter-fibre force transmission during contraction. These would be a first model that could take into account micro-structural arrangements in order to investigate the well-accepted hypothesis that muscle fibres are a 3D mechanical constructs transferring forces in longitudinal and transverse directions (see, e.g. [18, 19]). This is of particular interest as current (continuum) mechanical skeletal muscle models do only consider the (active) force transmission in the along-the-fibre direction. The goal of micro-mechanical models, which are based on segmented data, is to gain new insights of micro-mechanical structure and function and their implication on the whole muscle or organ level.

5 Conclusions and Future Work

This work is only a first step towards the fully automatic segmentation of muscle fibres. The results are promising, but have to be further improved. Besides a straightforward extension of the whole method to 3D, one could also guide, e.g. the active contours result by interacting with the algorithm manually and adding constraints during segmentation. Another way would be to apply statistical methods based on learning algorithms.

Acknowledgements The authors thank Dane Gerneke from the Auckland Bioengineering Institute (ABI) at the University of Auckland, New Zealand, for his tremendous effort, help, and expertise in preparing and imaging the skeletal muscle sample. The authors also thank A/Prof. Ian LeGrice from the ABI for providing the necessary lab space and access to the Welcome Trust extended-volume imaging system.

References

1. Hodgkin, A. L., Huxley, A. F., 1952. A quantitative description of membrane current and its application to conduction and excitation in nerve. J Physiol 117 (4), 500–44.
2. Shorten, P., O'Callaghan, P., Davidson, J., Soboleva, T., 2007. *A mathematical model of fatigue in skeletal muscle force contraction.* J Muscle Res. Cell Motil. 28 (6), 293–313.
3. Ding, J., Wexler, A. S., Binder-Macleod, S. A., 2000. *Development of a mathematical model that predicts optimal muscle activation patterns by using brief trains.* J of Appl. Physiol. 88 (3), 917–925.
4. Zajac, F. E., 1989. Muscle and tendon: properties, models, scaling, and application to biomechanics and motor control. Crit Rev Biomed Eng 17 (4), 359–411.

5. Johansson, T., Meier, P., Blickhan, R., 2000. A finite-element model for the mechanical analysis of skeletal muscles. J Theor Biol 206 (1), 131–49.
6. Oomens, C. W. J., Maenhout, M., van Oijen, C. H., Drost, M. R., Baaijens, F. P., 2003. Finite element modelling of contracting skeletal muscle. Philos. Trans. R. Soc. London, Ser. B, 358 (1437), 1453–1460.
7. Blemker, S. S., Pinsky, P. M., Delp, S. L., 2005. A 3d model of muscle reveals the causes of nonuniform strains in the biceps brachii, J. Biomech. 38 (4), 657–665.
8. Böl, M., Reese, S., 2007. A new approach for the simulation of skeletal muscles using the tool of statistical mechanics. Materialwiss. Werkstofftech. 38 (12), 955–964.
9. Röhrle, O., Davidson, J., Pullan, A., 2008. Bridging scales: a three-dimensional electromechanical finite element model of skeletal muscle. SIAM J. Sci. Comput. 30 (6), 2882–2904.
10. Röhrle, O., 2010. Simulating the electro-mechanical behavior of skeletal muscles. IEEE CiSE, DOI 10.1109/MCSE.2010.30.
11. Sands, G.B., Gerneke, D.A., Hooks, D.A., Green, C.R., Smaill, B.H., LeGrice, I.J., 2005. Automated imaging of extended tissue volumes using confocal microscopy. Microsc Res Tech 67 (5), 227–39.
12. Jähne, B., 2005. Digitale Bildverarbeitung, Springer-Verlag.
13. Ballard, D.H., 1981. Generalizing the Hough transform to detect arbitrary shapes, Pattern Recognit., 13, 111–122.
14. Kass M., Witkin, A., Terzopoulos, D., 1988. Snakes-active contour models, Int. J. Comput. Vision 1, pp. 321–331.
15. Osher, S., Fedkiw, R.P., 2002. Level set methods and dynamic implicit surfaces, Springer Verlag.
16. Osher, S., Paragios, N., 2003. Geometric level set methods in imaging, vision and graphics, Springer Verlag.
17. Li, B., Acton, S.T., 2007. Active Contour External Force Using Vector Field Convolution For Image Segmentation, IEEE Trans. Image Process. 16 (6), 2096–2106.
18. Maas, H., Baan, G. C., Huijing, P. A., 2001. Intermuscular interaction via myofascial force transmission: effects of tibialis anterior and extensor hallucis longus length on force transmission from rat extensor digitorum longus muscle. J Biomech 34 (7), 927–940.
19. Bloch, R., Gonzalez-Serratos, H., 2003. Lateral force transmission across costameres in skeletal muscle. Exercise Sport Sci R 31 (2), 73–78.

A Quantitative Description of Pelvic Floor Muscle Fibre Organisation

Xiani Yan, Jennifer A. Kruger, Martyn P. Nash, and Poul M.F. Nielsen

Abstract The levator ani (LA) muscles play an important role in pelvic floor function. With the aid of computer models and mechanics simulations, the injury mechanism of LA muscles can be better understood to prevent pelvic floor dysfunction. However, the lack of quantitative description of pelvic floor muscle organisation may compromise the accuracy of the models and simulations. The aim of this work was to establish a quantitative model of the pelvic floor muscle fibre organisation utilising the Visible Human Project® dataset. An anatomical finite element model of the pelvic floor muscles (levator ani and external sphincter) was constructed from the Visible Woman (VW) dataset. Fibre orientations were detected from the VW images using a structure tensor method and principal component analysis. Fibre orientation data were embedded within the geometric model using nonlinear finite element fitting. The fitted fibre field was qualitatively compared with the literature. Future work will include cadaver dissections for clearer classification of different muscles, and the creation of a generic pelvic floor fibre organisation model using DT-MRI data from living subjects and cadavers. The models will be used for pelvic floor mechanics studies such as modelling the second stage of labour during vaginal delivery.

Keywords Pelvic floor anatomy · Image processing · Structure tensor method · Finite element modelling · Vaginal delivery

1 Introduction

The levator ani (LA) is a dome-shaped muscular sheet that plays an important role in pelvic floor muscle function. It maintains urinary and anal continence, generates intra-abdominal pressure, and participates in the second stage of labour [1, 2]. The LA is subdivided into three muscles of various thicknesses: the pubococcygeus and

X. Yan (✉)
Auckland Bioengineering Institute, The University of Auckland, Auckland, New Zealand
e-mail: xyan075@aucklanduni.ac.nz

A. Wittek et al. (eds.), *Computational Biomechanics for Medicine: Soft Tissues and the Musculoskeletal System*, DOI 10.1007/978-1-4419-9619-0_13,

iliococcygeus in the posterior compartment, and the puborectalis at the inferior of the pelvic floor [3]. These muscles are attached to the inner surface of the pelvis and close off the bony pelvis, forming a large portion of the pelvic floor [2,4].

Previous studies have demonstrated a clear association between LA muscle trauma and a difficult vaginal childbirth, although the exact mechanism of this trauma is not clear [5, 6]. The damage often manifests as a complete or partial detachment of the LA muscle from the pubic bone, resulting in pelvic floor dysfunction with an associated increase in pelvic organ prolapse and urinary stress incontinence [6–8]. In light of this, it is clear that methods need to be developed to assess those women most at risk in order to prevent possible subsequent pelvic floor disorders [9].

Over the last two decades, there has been significant improvement in the understanding of the LA muscles in terms of their anatomy and physiology. With the aid of modern imaging modalities including ultrasound, computer-aided tomography (CAT) scanning, and magnetic resonance imaging (MRI), researchers and engineers have been able to create computer models of LA muscles to better visualise their 3D morphology, and to conduct mechanics simulations. However, there is a lack of quantitative data on the fibre architecture of the LA muscles, due to their relative inaccessibility and limitations in the in vivo resolution that can be achieved by the available imaging modalities. Janda et al. [10] qualitatively described the arrangement of the major LA muscle bundles from an embalmed cadaver, measured with a palpator and strings. However, these data are not available in a quantitative form and information on the muscle contractility and fibre-related material anisotropy, required for mechanical analysis (e.g. injury mechanism), remains unknown.

The majority of studies that have conducted childbirth simulations have made assumptions about the fibre organisation of the LA muscles. In these studies, muscle fibre bundles were either assumed to align with the directions of origin-insertion pairs established in the literature [11], or simplified so that the muscles' mechanical properties were considered to be passive and isotropic [12]. These simplifying assumptions are likely to impact on the accuracy of the models and simulations. A quantitative description of the fibre architecture is crucial to establish a more reliable anatomical model of the LA muscles during childbirth simulations. This will ultimately provide a better understanding of the mechanical response of the muscles and the possible mechanism of birth-induced trauma that result in pelvic floor dysfunction.

To construct models on muscle fibre organisation, researchers have recently used data from either high-resolution anatomical images with clearly distinguishable muscle bundles, or diffusion tensor MRI. Two studies in the past used the Visible Human Project® dataset to retrieve information on skeletal muscle fibre orientations of limbs, using a range of image processing techniques [13–15]. This study utilises the anatomical images of the pelvic floor region from the Visible Woman dataset to generate a quantitative description on the pelvic floor muscle fibre architecture, using a structure tensor method.

2 Method

The analysis was performed using the Visible Human Project® dataset provided by the National Library of Medicine, Bethesda, ML, USA (Fig. 1). The dataset includes 250 anatomical cross-section images of the Visible Woman (VW) in the pelvic floor region. The resolution of the images is 0.33 × 0.33 mm per pixel in-plane, with a 0.33-mm interval between two successive images [15].

On the VW images, the muscles (red) could be distinguished from the surrounding adipose (cream) and connective (white) tissues; the anisotropic information of the spatial distribution of colour and texture within the images could therefore be used to infer fibre orientations. Since the fibre orientations of LA muscles do not necessarily run in plane with the images, a three-dimensional structure tensor method was used to capture both in-plane and out-of-plane variations of fibre orientation. The images were converted into grey-scale intensity maps for ease of computation.

In addition to quantifying the fibre architecture of the LA muscles, the superior part of the external sphincter (ES) muscle was also analysed for fibre orientations, due to its close association with the LA muscles [4].

2.1 Computation of Colour Gradients

A structure tensor approach and principal component analysis were used to extract the 3D fibre organisation [16]. To do this, colour gradients were computed in three fundamental directions along the width (**Gx**), length (**Gy**) and thickness (**Gz**) of the image stack, by applying the derivative of Gaussian low-pass filter. To improve computational efficiency, the Fourier transform was used to convert both the image stack and the filter kernel into their frequency space representations, so that the

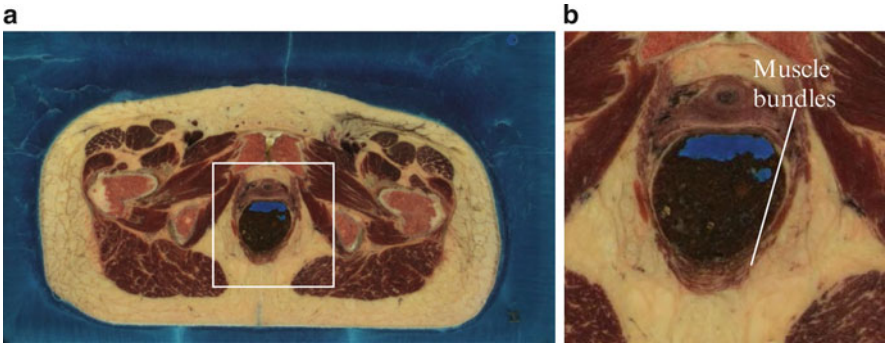

Fig. 1 Anatomical cross-sectional image (2,619th slice) of visible woman (**a**) and an enlarged region of the pelvic floor muscles (**b**)

convolution between them could be performed as a set of simple multiplications. As a result, three smoothed gradients ($\mathbf{Gx}_s$, $\mathbf{Gy}_s$ and $\mathbf{Gz}_s$) were obtained at each voxel, and these gradients were subsequently used for construction of the structure tensors.

2.2 Structure Tensors

The structure tensor is a measure of local coherence of structures [17]. The symmetric 3 × 3 structure tensor at each voxel was constructed as:

$$\mathbf{T} = \nabla \mathbf{U}_\sigma \otimes \nabla \mathbf{U}_\sigma = \nabla \mathbf{U}_\sigma \nabla \mathbf{U}_\sigma^{\mathbf{T}} \tag{1}$$

where $\nabla \mathbf{U}_\sigma$is the texture field. Hence,

$$\mathbf{T} = \begin{bmatrix} \mathbf{Gx}_s^2 & \mathbf{Gx}_s\mathbf{Gy}_s & \mathbf{Gx}_s\mathbf{Gz}_s \\ \mathbf{Gy}_s\mathbf{Gx}_s & \mathbf{Gy}_s^2 & \mathbf{Gy}_s\mathbf{Gz}_s \\ \mathbf{Gz}_s\mathbf{Gx}_s & \mathbf{Gz}_s\mathbf{Gy}_s & \mathbf{Gz}_s^2 \end{bmatrix} \tag{2}$$

where $\mathbf{Gx}_s$, $\mathbf{Gy}_s$ and $\mathbf{Gz}_s$ are the smoothed gradients in three fundamental directions at a voxel.

2.3 Principal Component Analysis

Eigen-analysis on each structure tensor was used to extract the direction in which least colour change took place, which was assumed to align with the fibre orientation. For each voxel, eigen-decomposition was performed on the structure tensor, and the eigen-vector with the smallest corresponding eigen-value was taken as the fibre direction (associated with the least colour change). As a result, a volume of fibre orientations was obtained from the image stack, with one orientation vector for each voxel. Figure 2c shows the fibre orientation results, for clarity, in 2D and at a low-spatial frequency.

To eliminate irrelevant information from the surrounding tissues and structures, a 3D mask, created by manual segmentation of the same image stack, was imposed on the results to only highlight the pelvic floor muscles (Fig. 2a, b). As a result, the continuous dark-red muscle bundles together with their orientations could be extracted from the VW images. For the segmentation, the LA muscles were treated as a single entity and only the outermost boundary with the connective tissues was outlined. This is because the LA exists as a continuous composite muscle, and the boundaries were not clearly identifiable on the VW images due to their limited resolution [2, 3, 18].

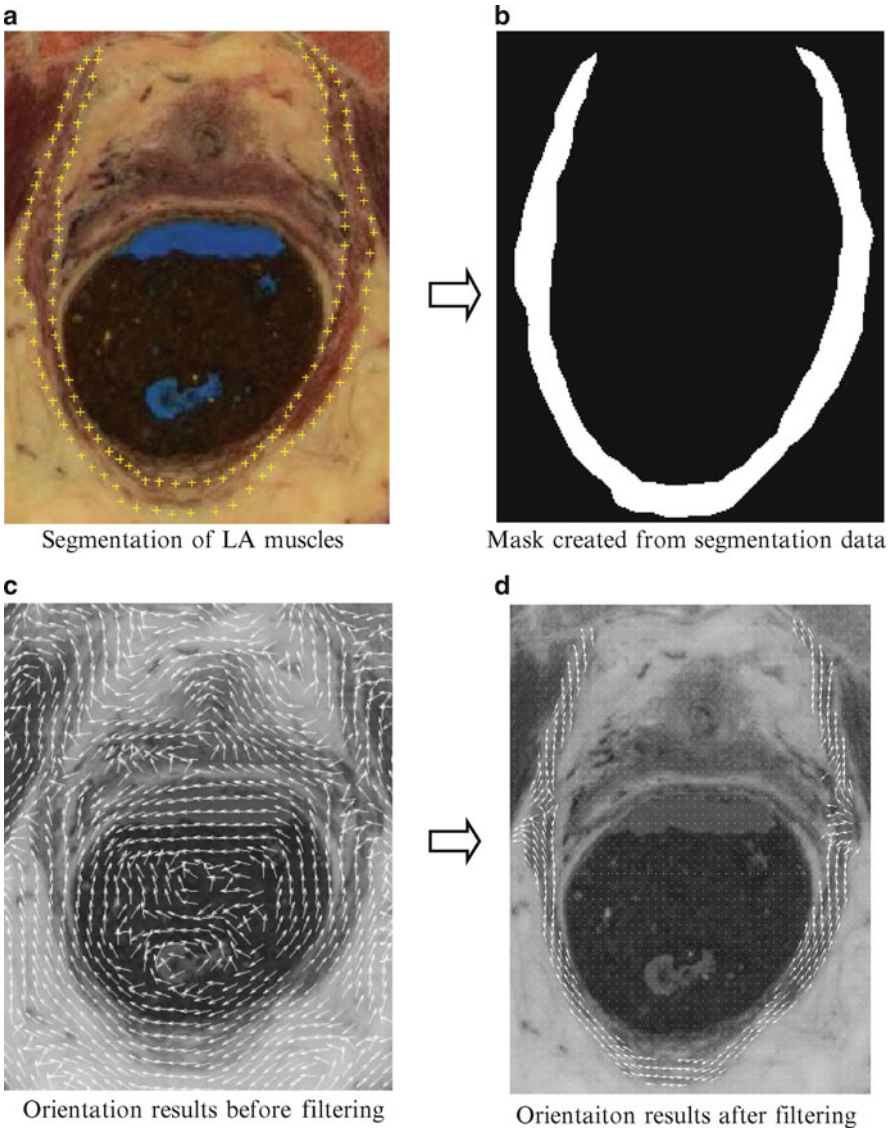

Fig. 2 A mask was created from manual segmentation data, which was imposed on the orientation results to highlight only the muscles

2.4 Post-Processing of Orientation Results

In order to fit the orientation results appropriately into a geometric model, the orientations needed to be directed in consistent directions since they were only unique within a principal angle range of π. Since the muscles approximately adopted a circumferential shape, the orientation results were converted from Cartesian

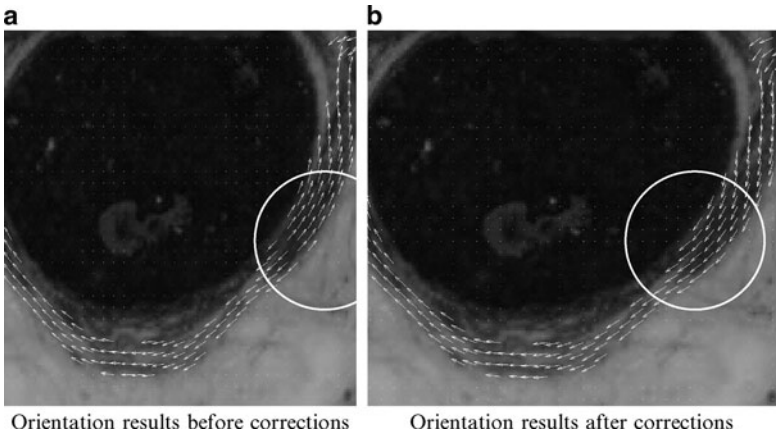

Fig. 3 Fibre orientation results were corrected according to their polar coordinates, so that discrepancy in orientations was removed

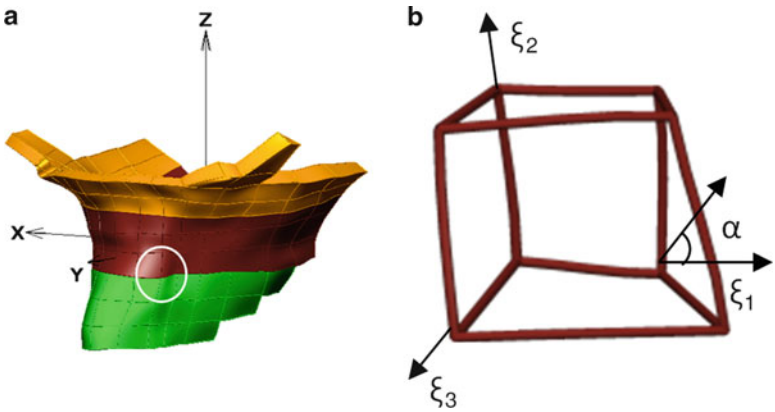

Fig. 4 Geometric model of the levator ani and external sphincter muscles. The encircled element is enlarged in (**b**) to illustrate the element coordinates and the fibre angle. Gold, coccygeus and iliococcygeus; dark-red, pubococcygeus and puborectalis; green, external sphincter

coordinates (x, y, z) into polar coordinates (r, θ, z), and corrections were made so that $-\frac{\pi}{2} < \theta \leq \frac{\pi}{2}$ was satisfied for each computed direction. Figure 3 illustrates the difference that this correction process made to the results. The discrepancy in fibre orientations, as highlighted in the white circle in Fig. 3a, was eliminated by the correction process as shown in Fig. 3b.

2.5 Fitting of Fibre Orientations

A finite element model (Fig. 4a) of the LA and ES muscles, interpolated by a tricubic Hermite scheme, was created by fitting surface data of the muscles from the

segmentation to a modified existing trilinear mesh constructed by Noakes [19]. Fitting of the geometry and the fibre angles were both performed using a nonlinear least-squares optimisation algorithm, which was implemented in the CMISS software [20]. In the finite element geometric model, in addition to the spatial coordinates (x, y, z), finite element coordinates (ξ_1, ξ_2, ξ_3) were defined that moved with the deforming elements. The orientation results were embedded into the geometric model, quantified using a fibre angle α with respect to the axial anatomical plane and interpolated trilinearly with respect to the element coordinates.

3 Results and Discussion

3.1 Muscle Geometry

The LA and ES muscles were collectively represented using a single continuous finite element model, since their fibre architectures were not visibly distinct on the VW dataset. Moreover, some fibres of the puborectalis blend into that of the ES muscle, thus their boundaries were difficult to locate. The relative positions of the muscles could only be approximately differentiated as shown in Figs. 4 and 5, due to the finite discretisation of the model. Muscles in relative proximity (e.g. the pubococcygeus and puborectalis) are represented by the same colour. The anatomical position of the LA and ES with respect to the pubic bone and coccyx is illustrated in Fig. 5.

A small amount of Sobelov smoothing was applied during the geometric fitting procedure, so that excessive curves due to the scattered data were penalised and a geometric model with smooth surfaces was obtained. The root mean square error (RMSE), a measure of accuracy of the fitting, was 0.86 mm and sufficiently small for the fitted model to represent the variations of the model surface morphology. The accuracy of the fitting was comparable with that in another study using finite element

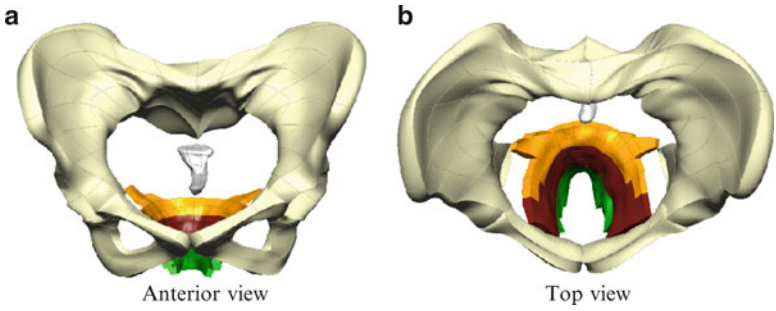

Fig. 5 The pelvic floor muscle finite element geometric model in a global perspective. Bone Pubic bone; silver, coccyx; gold, coccygeus and iliococcygeus; dark-red, pubococcygeus and puborectalis; green, external sphincter

modelling of the pelvic floor (RMSE = 0.939 mm for the LA muscle model) [19]. The spatial resolution of the model is 16 elements in the ξ_1 direction and 8 elements in ξ_2 direction, with 7,152 degrees of freedom.

Since the VW dataset was obtained post-mortem, there was a loss in muscle tone, which likely resulted in a difference in muscle morphology compared to that of a living woman. Such differences may be corrected by 3D registration with images captured from living subjects, where landmark points on a mesh created from in vivo data are mapped with the target point at the same anatomical positions on the mesh with the lost muscle tone [21].

3.2 Muscle Fibre Field

The fibre organisation of the LA and ES muscles are shown in Fig. 6. The orientation vectors are plotted for a mid-line across the muscle wall thickness, with spatial distributions illustrated on the external surfaces of the model for ease of visualisation. Only one layer of fibre orientations are shown, since the transmural variation of fibre orientations across the muscle walls is relatively small compared to the longitudinal variation, whilst most muscle fibres lie in the surface tangent plane.

The overall RMSE of the fibre angle fitting was approximately 40°, indicating that the orientation results used for fitting were somewhat scattered. The dispersion of orientation results was due to the low level of smoothing applied during the image colour gradient computation, which aims to retain maximal information on texture anisotropy. In addition, since the geometry and fibre organisation of the muscles were very irregular, the finite discretisation of the geometric model imposed restrictions on the details and variations that could be captured by the model, which in turn contributed to the large fitting errors.

Due to a lack of quantitative studies of the fibre organisation in the pelvic floor muscles, the orientation results obtained here could only be compared with literature on LA muscle anatomy. Superiorly in the pelvic floor, the iliococcygeus is described to arise from a reinforced facial band attached to the inner surface of the ischial spines and inserts into the coccyx [2,4,22]. The fibres of iliococcygeus in the model run from the point lateral to ischial spine to the point of coccyx in a descending course (Fig. 6a), which is consistent with the description in the literature.

The pubococcygeus, connected to the iliococcygeus anteriorly in the model, originates from the inner surface of superior pubic ramus and inserted into the coccyx (Fig. 6a, c), which is also consistent with the muscle architecture described by Carrière et al. [4]. However, the fact that some fibres of the iliococcygeus blend into that of pubococcygeus made it difficult to identify muscles on the VW dataset. Therefore, the boundary between the iliococcygeus and pubococcygeus was only approximated in the model [2,4,23]. Dissections of pelvic floors of human cadavers would help with the muscle identification and construction of a generic pelvic floor muscle model. Our group is presently piloting such research.

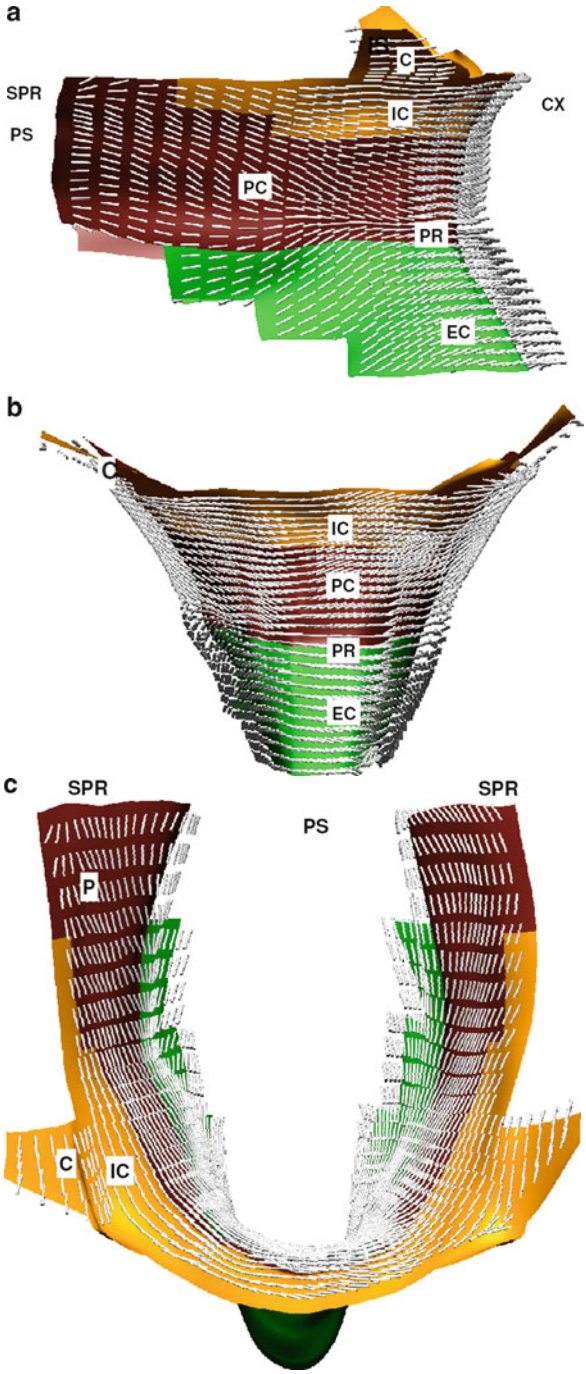

Fig. 6 Fibre orientation distribution of the levator ani and external sphincter muscles in side view (**a**), posterior view (**b**) and top view (c). *C* coccygeus, *IC* iliococcygeus, *PC* pubococcygeus, *PR* puborectalis, *ES* external sphincter, *IS* ischial spine, *CX* coccyx, *SPR* superior pubic ramus, *PS* pubic symphysis

Table 1 Means and standard deviations of fibre angles in the different muscle groups of the pelvic floor

Fibre angle (°)	Left lateral	Central	Right lateral
Coccygeus and iliococcygeus	-8 ± 27	-3 ± 27	10 ± 32
Pubococcygeus and puborectalis	-6 ± 25	2 ± 20	7 ± 43
External sphincter (ES)	23 ± 15	-7 ± 15	-25 ± 25

The puborectalis is continuous with the pubococcygeus caudally and arises on the inner surface of the pubic bone, forming a sling around the vagina. It connects the ES muscle that anchors in the connective tissue of the perineal body [3, 4]. Our results show that the fibres of the puborectalis originate from the position of the pubic bone and run almost horizontally to form a semicircle (Fig. 6b). These fibres can be distinguished from those of the ES, which insert into the anococcygeal body in an ascending course in the model (Fig. 6a) [4].

A statistical analysis was performed on the fitted fibre fields for the different muscle groups (Table 1). It is clear that the fibres of iliococcygeus run in a descending manner, since the position of their origin (lateral to the ischial spines) is slightly more superior to that of their insertion (coccyx). In contrast, the fibres of the ES insert superiorly into the coccyx by the anococcygeal body and therefore they follow an ascending course. In addition, the fibres in the central-anterior region seem to run more horizontally than they do in the lateral-posterior region, since medially almost all muscles insert into the coccyx and the anococcygeal body [4, 22].

3.3 Model limitations

First, the resolution of VW dataset imposes restrictions on the level of detail that could be captured by the model. Second, since the structure tensor method is based on image analysis, the anisotropy of the colour texture field in the VW dataset was assumed to represent the fibre architecture. Whilst this approach has been validated for determining the fibre architecture of cardiac muscle, this method is not based on intrinsic properties of muscles [24]. On the other hand, diffusion tensor MRI constructs a tensor based on the dominant molecule diffusions in the direction of continuous fibres. In the future, we plan to use DT-MRI data from cadavers' pelvises and living volunteers to investigate the spatial organisation of fibre structure in the pelvic floor muscles.

4 Conclusions

A fitted finite element model of the pelvic floor muscles, with embedded fibre field, was obtained from the cross-sectional anatomical images of the VW dataset, using the structure tensor approach and principal component analysis. The model can be

directly used for biomechanical modelling, such as simulations of the second stage of labour. With quantitative knowledge of the muscle fibre organisation, the contractility of the pelvic floor muscles as well as their injury mechanism during vaginal delivery can be further explored and better understood. The model has the potential to be customised specifically to individual patients and help with prediction and prevention of possible childbirth-induced pelvic floor trauma.

Acknowledgements The authors acknowledge the National Library of Medicine of the US Department of Health and Human Services for permission to use the visible woman dataset. X. Yan is financially supported by the University of Auckland Doctoral Scholarship. J. A. Kruger is supported by a Rutherford Foundation Postdoctoral Fellowship funded by the Royal Society of New Zealand. M. P. Nash and P. M. F. Nielsen are supported by a James Cook Research Fellowship administered by the Royal Society of New Zealand on behalf of the New Zealand Government.

References

1. Bharucha, A.E., Pelvic floor: anatomy and function. Neurogastroenterol Motil, 2006. 18(7): p. 507–19.
2. Standring, S. and H.A. Gray, Gray's anatomy: the anatomical basis of clinical practice. 40th ed. 2008, Edinburgh: Churchill Livingstone. xxiv, 1551 p.
3. Fritsch, H., et al., Clinical Anatomy of the Pelvic Floor. Clinical Anatomy of the Pelvic Floor, 2004. 175: p. 1–64.
4. Carrière, B., C. Markel Feldt, and K. Bø, The pelvic floor. 2006, Stuttgart; New York, N.Y.: Thieme. xii, 476 p. ill.
5. DeLancey, J., et al., The appearance of levator ani muscle abnormalities in magnetic resonance images after vaginal delivery. Obstetrics and gynecology, 2003. 101(1): p. 46.
6. Dietz, H. and V. Lanzarone, Levator trauma after vaginal delivery. Obstetrics & Gynecology, 2005. 106(4): p. 707.
7. Dietz, H. and J. Simpson, Levator trauma is associated with pelvic organ prolapse. British Journal of Obstetrics and Gynaecology, 2008. 115(8): p. 979–84.
8. Patel, D., et al., Childbirth and pelvic floor dysfunction: an epidemiologic approach to the assessment of prevention opportunities at delivery. American journal of obstetrics and gynecology, 2006. 195(1): p. 23–28.
9. Nygaard, I., Should women be offered elective cesarean section in the hope of preserving pelvic floor function? International Urogynecology Journal, 2005. 16(4): p. 253–254.
10. Janda, T., F.C.T. van der Helm, and S.B. de Blok, Measuring morphological parameters of the pelvic floor for finite element modelling purposes. Journal of Biomechanics, 2003. 36(6): p. 749–757.
11. Lien, K.C., et al., Levator ani muscle stretch induced by simulated vaginal birth. Obstetrics & Gynecology, 2004. 103(1): p. 31–40.
12. Li, X., et al. Effects of Fetal Head Motion on Pelvic Floor Mechanics. in MICCAI. 2009. London: Springer.
13. Dong, F., et al., An anatomy-based approach to human muscle modeling and deformation. IEEE Transactions on Visualization and Computer Graphics, 2002. 8(2): p. 154–170.
14. Sachse, F., et al., Extension of anatomical models of the human body: Three-dimensional interpolation of muscle fiber orientation based on restrictions. CIT. Journal of computing and information technology, 1998. 6(1): p. 95–101.
15. Waldby, C., The Visible Human Project: informatic bodies and posthuman medicine. Biofutures, biocultures. 2000, London: Routledge. xii, 184 p.
16. Bigun, J. and G.H. Granlund. Optimal Orientation Detection of Linear Symmetry. in IEEE First International Conference on Computer Vision 1987.

17. Weickert, J., Anisotropic diffusion in image processing. 1998, Stuttgart: Teubner. xii,170 p.
18. Bishop, M.J., et al., Development of an anatomically detailed MRI-derived rabbit ventricular model and assessment of its impact on simulations of electrophysiological function. American Journal of Physiology-Heart and Circulatory Physiology, 2010. 298(2): p. H699-H718.
19. Noakes, K., Anatomically realistic finite element models of the pelvic floor & anal canal: towards understanding the mechanisms of defaecation. 2007, Bioengineering, University of Auckland, 2007. p. xvi, 176 p.
20. Continuum Mechanics, Image analysis, Signal processing and System Identification. Available from: www.cmiss.org.
21. Suri, J.S., D.L. Wilson, and S. Laxminarayan, Handbook of biomedical image analysis. Biomedical engineering international book series. 2005, New York: Kluwer Academic/Plenum Publishers.
22. Wolff, B., J. Fleshman, and D. Beck, The ASCRS textbook of colon and rectal surgery. 2007: Springer Verlag.
23. Lawson, J.O., Pelvic anatomy. I. Pelvic floor muscles. Annals of The Royal College of Surgeons of England, 1974. 54(5): p. 244–52.
24. Hooks, D.A., et al., Laminar arrangement of ventricular myocytes influences electrical behavior of the heart. Circulation Research, 2007. 101(10): p. e103–12.

An Evaluation of Tetrahedral Mesh Generation for Nonrigid Registration of Brain MRI

Panagiotis A. Foteinos, Yixun Liu, Andrey N. Chernikov, and Nikos P. Chrisochoides

Abstract In this chapter, we assess the impact of mesh generation on nonrigid registration of brain MR images. The solution accuracy and the speed of finite element solvers depend on how well the underlying mesh approximates the surface of the biological object (fidelity), and how well the elements of this mesh are shaped (quality). Fidelity and quality, however, are two contradicting requirements, as increased fidelity usually implies poor quality and vice versa.

In this chapter, we evaluate three public mesh generators and examine how this quality-fidelity trade-off affects the accuracy and the speed of nonrigid registration solvers for brain images.

Keywords Mesh generation · Finite element method · Non-rigid registration

1 Introduction

In computer-aided surgery (CAS) and specifically in image-guided neurosurgery, magnetic resonance images (MRI) obtained before the procedure (preoperative) provide extensive information which can help surgeons to plan a resection path. Careful planning is important to achieve the maximal removal of malignant tissue from a patient's brain, while incurring the minimal damage to healthy structures and regions of the brain. However, current practices of neurosurgical resection involve the opening of the scull and the dura. This results in a deformation of the brain (known as the brain shift problem), which creates discrepancies between the preoperative imaging data and the reality during the operation. A correction is possible using nonrigid registration (NRR) of intraoperative MRI with preoperative data.

In this chapter, we target finite element (FE)-based approaches for the nonrigid registration [6]. These methods use real-time landmark tracking across the

P.A. Foteinos (✉)
Computer Science Department, College of William and Mary, Williamsburg, VA, 23187, USA
and
Computer Science Department, Old Dominion University, Norfolk, VA, 23529, USA
e-mail: pafotein@gmail.com

A. Wittek et al. (eds.), *Computational Biomechanics for Medicine: Soft Tissues and the Musculoskeletal System*, DOI 10.1007/978-1-4419-9619-0_14,

entire image volume, which makes the nonrigid registration more accurate but computationally expensive, as compared to similar methods that use surface tracking [8]. The nonrigid registration problem should be solved fast enough, so that it can be usable in clinical studies [2, 3].

Real-time Image-to-Mesh (I2M) conversion is a critical component of FE-based nonrigid registration of brain images. Moreover, its solution in N dimensions (with $N \geq 4$) is important for handling geometric uncertainties caused by respiratory motion, which complicates planning and treatment.

A mesh is characterized by its *fidelity* and *quality*. Fidelity measures how well the mesh boundary resembles the surface of the biological object. Quality assesses the shape of mesh elements; the higher the minimum dihedral angle of the mesh elements is, the higher the quality.

It is well known that the quality of the mesh affects both the accuracy and the speed of the solver [14], because the angles of the elements influence the condition number of the stiffness matrix. In the literature, a good deal of effort has been put toward high-quality mesh generation [5, 9, 10, 16].

It is not clear, however, what the impact of fidelity on the accuracy and speed of the solver is. The reason is because there is a complicated trade-off between quality and fidelity. The need for a better surface approximation always implies a deterioration of mesh quality, simply because well-shaped elements cannot fill the space formed by sharp surface creases or by surface parts of high curvature. Also, higher fidelity usually results in an increase in the number of mesh elements which in turn affects both the mesher's and the solver's speed.

In this chapter, we evaluated the impact of three public mesh generators [9,11,15] on the accuracy and speed of NRR. The meshers were chosen carefully to cover a wide range of mesh generation approaches. The Delaunay mesh algorithm in [9] offers simultaneous meshing of the surface and the volume of the object. The algorithm in [15] is Delaunay but requires the surface of the object as input. Finally, the algorithm in [11] is an optimization-based technique which compresses an initial body-centered cubic lattice (BCC) to the surface (see Sect. 3 for more details). For each mesher, we conducted an extensive series of experiments controlling the fidelity of the output mesh used for the subsequent NRR [6].

We concluded that meshes with very bad fidelity do not affect the accuracy drastically. On the contrary, meshes with very good fidelity hurt the speed of the mesher due to the poor quality they exhibit. We also observed that the speed of the solver is very sensitive to mesh quality rather than to fidelity. For these reasons, we think that mesh generation should first try to produce high quality meshes, possibly sacrificing fidelity.

2 Registration

As our target application, we used the nonrigid registration method described by Clatz et al. [6] which is shown to be robust enough to be usable to clinical studies. Below, we outline the main aspects of this NRR method.

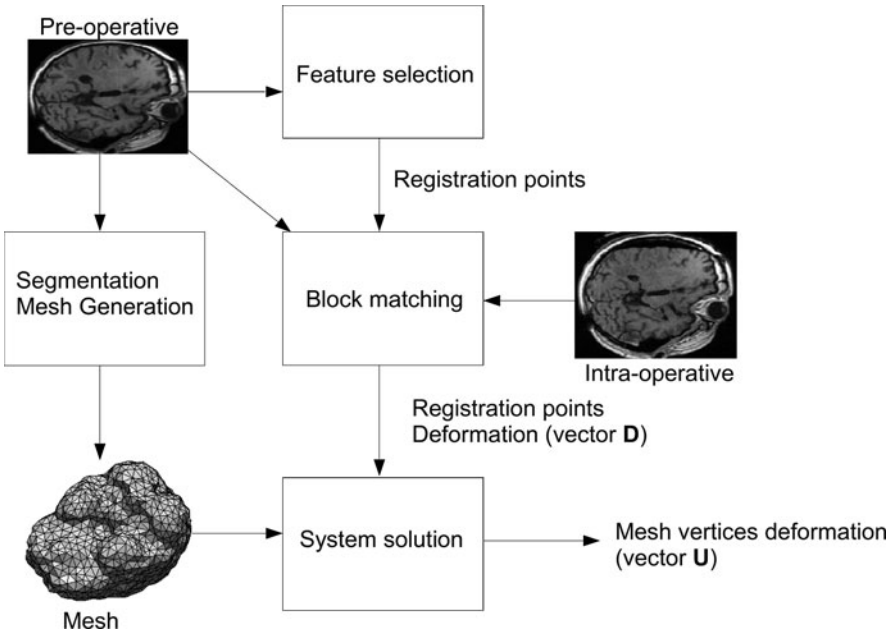

Fig. 1 The nonrigid registration procedure

The method consists of three steps, namely, *feature points selection*, *block matching*, and *system solution*. See Fig. 1 for an illustration. During feature points selection, a sparse set of points is chosen from the preoperative image. These points are called *registration* points. Then, the correspondence of these points into the intraoperative image is found via a block matching scheme. Specifically, for a given registration point r, a small window around it in the intraoperative image is searched; the corresponding point r' reported is the one that maximizes the correlation coefficient between r' and r.

Having computed the deformation vector $\mathbf{D}$ on the registration points (as a result of the block matching step), the deformation vector on the mesh vertices $\mathbf{U}$ (the unknowns) is calculated so that the following energy is minimized:

$$W = \underbrace{(\mathbf{HU}-\mathbf{D})^{\top}(\mathbf{HU}-\mathbf{D})}_{\text{Error energy}} + \underbrace{\mathbf{U}^{\top}\mathbf{KU}}_{\text{Mechanical energy}} \tag{1}$$

In the above equation, $\mathbf{K}$ is the $|U| \times |U|$ mechanical stiffness matrix. $\mathbf{H}$ is the linear interpolating matrix of size $|D| \times |U|$; this matrix contains the measurements of the linear shape functions on every registration point. The contributing shape functions for each registration point r_i are those defined over the mesh nodes whose forming mesh element includes r_i.

The block matching deformation d_i of a registration point r_i affects the deformation of a mesh node v_j, only if v_j is incident upon a mesh element e that contains r_j. In fact, if the minimization of the error energy (also known as matching energy) in (1) was perfect (i.e., if it vanished), then the linear interpolation (of the solution of the mesh nodes of e) on r_i would give the value d_i. As Clatz shows in [6] (and as we can see from (1)), this method tries to minimize this exact error energy E:

$$E = \sqrt{(\mathbf{HU}-\mathbf{D})^{\top}(\mathbf{HU}-\mathbf{D})} = ||\mathbf{HU}-\mathbf{D}|| \tag{2}$$

which is the interpolation error on the registration points $r_1, r_2, \ldots, r_{|D|}$.

The mechanical energy in (1) is used to model the deformation of the brain as a physical body based on FEM. This, in turn, is used to discover and discard the outlier registration points, i.e., points whose deformation estimation from block matching contradicts the physical properties of the brain. For information about the construction of the mechanical stiffness matrix $\mathbf{K}$, see Delingette and Ayache [7].

The deformation vector $\mathbf{U}$, over which energy W is minimized, is computed through the following iterative equations:

$$\begin{aligned} \mathbf{F}_0 &= 0\,, \\ \left(\mathbf{K}+\mathbf{H}^{\top}\mathbf{H}\right)\mathbf{U}_i &= \mathbf{H}^{\top}\mathbf{D}+\mathbf{F}_{i-1}, i = 1,2,\ldots, \\ \mathbf{F}_i &= \mathbf{K}\mathbf{U}_i, i = 1,2,\ldots \end{aligned}$$

In [6], it is proved that the system above converges. Also, observe that $\mathbf{K}+\mathbf{H}^{\top}\mathbf{H}$ is the matrix responsible for the robustness of NRR; its condition number affects both the accuracy and the speed of the solution.

3 Mesh Generation

In this chapter, we tested the influence of three meshers on NRR, namely, *High Quality Delaunay* mesher (HQD) [9], *Tetgen* [15], and *Point-Based Matching* mesher (PBM) [11]. Below, we briefly describe each of them.

HQD meshes both the surface and the volume of the object at the same time without an initial dense sampling of the object surface, as is the case in other Delaunay volume techniques [12, 13]. As a result, the number of elements of the output mesh is small.

Tetgen is a Delaunay mesh generator as well. However, it assumes that the surface of the object is already meshed and represented as a polyhedron. This polyhedron is also known as a *Piecewise Linear Complex* (PLC). Tetgen requires a PLC of the object surface as its input. We used the algorithm in [4] for the PLC generation, implemented in the *Computational Geometry Algorithms Library* (CGAL) [1].

PBM is an optimization-based approach. It starts with a triangulation of a regular grid, i.e., a body-centered cubic lattice (BCC), and then it compresses the outer nodes closer to the object surface as a result of energy minimization. In fact, the smaller the energy achieved, the better the fidelity of the output mesh. This method is able to recover the surface of multi-tissue objects. In this chapter, only the single-tissue version of PBM is considered.

4 Evaluation

4.1 Methodology

As mentioned in Sect. 2, registration computes the deformation on the mesh nodes, so that the error energy $E = ||\mathbf{HU} - \mathbf{D}||$ is minimized. Mesh generation affects how accurately the error energy is minimized. Therefore, we assess the accuracy of registration by keeping track of this error E. For every run, we let the system iterate for ten times.

Observe, however, that the outcome of the registration depends on the accuracy of the block matching step (vector $\mathbf{D}$). Also, note that the mesh does not affect the result of block matching (see Fig. 1). Since we are interested in evaluating the impact of mesh generation on registration, we wanted to make registration independent of block matching. For this reason, we synthetically deformed the preoperative image according to the biomechanical properties of the brain. More specifically, we initially ran the registration procedure to register the preoperative with the intraoperative image as shown in Fig. 1, but at that time we did not focus on the behavior of the mesh. We just wanted the solution on the mesh nodes. Then, by (linearly) interpolating the solution of the mesh nodes on any point of the image, we obtained a synthetically deformed (intraoperative) image. After this initial registration, all the other registrations (aiming at evaluating mesh generation) are performed between the preoperative and the synthetically deformed image; that is, the real intraoperative image is replaced by the deformed one. In this way, we achieve two things:

- We know the "true" deformation on any point, and therefore we know the "true" block matching result on any set of registration points
- We do not simulate an arbitrary deformation, but rather a realistic one, because the deformed image was obtained taking into account the elasticity properties of the brain through the stiffness matrix $\mathbf{K}$ of 1

For the initial registration procedure used to synthetically deform the preoperative image, we set the parameters to the same values as described in [6] with parameter λ assigned to 1.0. In this way, we obtained a set of 4,000 registration points.

Since we want to measure the influence of mesh generation, only the mesh changes in every experiment. That is, for all the various meshes, the preoperative

image and the set of registration points (together with their deformation **D** of course) remain fixed. Note that for these subsequent registration procedures, we do not reject registration points as potential outliers, simply because the synthetic deformation implies that there are no outliers (this is not the case for the initial registration). For the same reason, we do not weight vector **D** according to the confidence of the registration points deformation. For all the experiments, parameter λ was set to 1.0.

4.2 Measuring and Varying Fidelity

As mentioned above, we wish to have control over the fidelity of the output mesh produced by the different meshers. In this chapter, we use the *two-sided Hausdorff distance H* to measure fidelity.

In our case, metric H is defined upon two finite sets A, B as follows:

$$H(A,B) = \max\{h(A,B), h(B,A)\}, \text{ where}$$
$$h(A,B) = \max_{a \in A} \min_{b \in B} ||a - b||$$

The lower the value of $H(A,B)$, the more similar sets A, B are. In fact, $H(A,B)$ is equal to 0 if and only if sets A, B are identical.

Fidelity of a mesh is measured as the two-sided Hausdorff distance H of the following sets:

- set A: a densely sampled point set on the surface of the biological object
- set B: a densely sampled point set on the boundary facets of the mesh

Note that the mesh boundary point set B does not consist of only boundary mesh vertices. The reason is because otherwise, at least one side of the Hausdorff distance of the meshes produced by HQD would always be 0 (or very close to 0), since this method guarantees that the boundary mesh vertices lie precisely on the object surface.

Having defined fidelity, we proceed by explaining how we control fidelity for each mesher.

For HQD, this is possible through the parameter δ (see [9] for a more detailed explanation). Low values of δ increase the sampling on the object surface which yields better fidelity. High values of δ produce meshes whose boundary crudely approximates the real surface.

For Tetgen, we had to change the fidelity of the PLC given by CGAL. We, therefore, had to adjust two parameters responsible for the PLC's fidelity. The first imposes an upper bound on the circumradius of the *Delaunay balls*, and the second forces an upper bound on the distance between the circumcenter of the boundary facets and the corresponding center of their Delaunay balls. More information can be found in [4].

For PBM, controlling fidelity is accomplished by adjusting the parameter λ. This parameter defines the trade-off between quality and fidelity: high values of λ make

the optimization more sensitive to good fidelity, while low values do not change a lot the position of the initial (high-quality) BCC. However, we observed that λ does not offer a very flexible control over flexibility. Therefore, to get meshes of substantially different fidelity, we had to change not only λ but also the density of the initial BCC.

4.3 Results

Table 1 presents the results obtained by various meshes produced by HQD. Each row corresponds to a singe mesh. Column H contains the Hausdorff distance between the mesh and the object surface. The table illustrates meshes ordered in increasing fidelity (i.e., in decreasing Hausdorff distance). It also shows the minimum and the average minimum dihedral angle of the mesh, as well as the total number of tetrahedra and vertices of the mesh. The condition number depicted is of the matrix $\mathbf{K} + \mathbf{H}^\top \mathbf{H}$ which is responsible for the accuracy and speed of the NRR solver (see Sect. 2). Finally, the last column reports the NRR error – as defined in (2) – obtained after the end of the registration process.

We observe that the error does not fluctuate considerably. All the errors are about less than half the size of a voxel (the size of the voxel is $1 \times 1 \times 1$), even when the H distance is very large. Figure 2 illustrates the meshes obtained by HQD for the best and the worst fidelity.

Table 2 shows the results for Tetgen. Similarly, fidelity does not seem to affect the error considerably. Also, although the minimum dihedral angles are larger than those

Table 1 Meshes with varying fidelity obtained by HQD

H	Minimum dihedral angle	Average minimum dihedral angle	#Tetrahedra	#Vertices	Condition number	Error
22.81	8.68	39.92	40	23	35,205.00	0.40
20.22	5.86	35.73	52	27	37,988.00	0.36
19.94	2.73	30.99	96	41	93,179.00	0.47
17.92	4.10	31.81	89	38	62,404.00	0.52
17.52	5.46	33.74	61	30	31,352.00	0.49
16.57	4.10	31.39	77	34	24,984.00	0.32
16.15	6.17	31.83	148	61	99,449.00	0.30
15.28	7.70	37.53	168	71	40,350.00	0.27
13.49	4.08	33.39	297	113	46,260.00	0.40
9.86	2.46	34.05	228	89	26,399.00	0.38
9.23	3.61	36.15	425	157	51,487.00	0.25
9.09	6.01	35.95	578	200	37,427.00	0.26
8.72	2.36	33.63	385	137	53,977.00	0.28
8.47	4.07	36.10	771	261	292,370.00	0.21
7.11	1.27	36.18	1,157	367	319,850.00	0.27
6.24	0.34	35.71	1,681	521	594,820.00	0.24
5.84	0.92	35.93	2,746	814	1,559,500.00	0.25

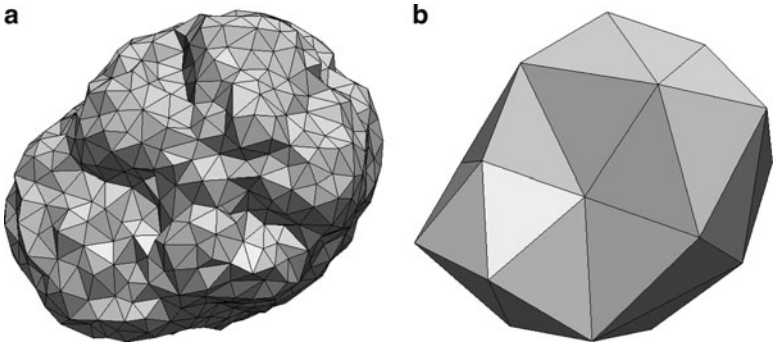

Fig. 2 Meshes produced by HQD. (**a**) H equal to 5.84 (best fidelity). (**b**) H equal to 22.81 (worst fidelity)

Table 2 Meshes with varying fidelity obtained by Tetgen and CGAL

H	Minimum dihedral angle	Average minimum dihedral angle	#Tetrahedra	#Vertices	Condition number	Error
23.23	5.60	24.09	262	104	292,820.00	0.25
20.03	5.60	24.21	264	105	92,234.00	0.41
18.84	3.61	20.51	371	142	4,175,200.00	0.36
17.33	7.36	24.51	207	82	123,670.00	0.41
16.25	4.92	28.11	179	148	211,360.00	0.40
14.98	6.97	26.84	141	59	17,882.00	0.50
14.36	4.02	22.16	609	224	1,098,800.00	0.33
13.53	4.92	28.49	156	143	298,850.00	0.36
12.43	6.88	26.72	320	185	1,209,500.00	0.39
11.47	5.77	25.83	227	88	58,552.00	0.42
10.22	3.76	21.82	1,052	377	1,715,700.00	0.46
9.74	4.51	21.11	946	337	4,400,400.00	0.37
8.54	2.20	21.58	1,500	531	2,418,900.00	0.41
7.92	2.29	21.54	2,010	710	28,992,000.00	0.45
7.35	1.88	20.77	2,539	878	6,459,100.00	0.43
6.02	1.52	21.17	7,006	2424	1,941,500,000.00	n/a
5.88	1.33	20.65	4,547	1585	205,230,000.00	n/a

in HQD, the average minimum dihedral angles are 10–15° less than those in HQD. This results in generally higher error than the error in HQD, but still the differences in accuracy are not very obvious. However, the much larger condition numbers affect the speed of the solver a lot. Actually, for the bottom two runs (corresponding to the meshes with the two best fidelity values and with the two higher condition numbers), the solver could not even converge. Figure 3 illustrates the meshes obtained by Tetgen for the best and the worst fidelity.

Table 3 presents the results for the PBM mesh. We observe that the quality is very good: the minimum and the average minimum dihedral angles reach perfection. This results in much lower condition numbers and generally lower error than HQD

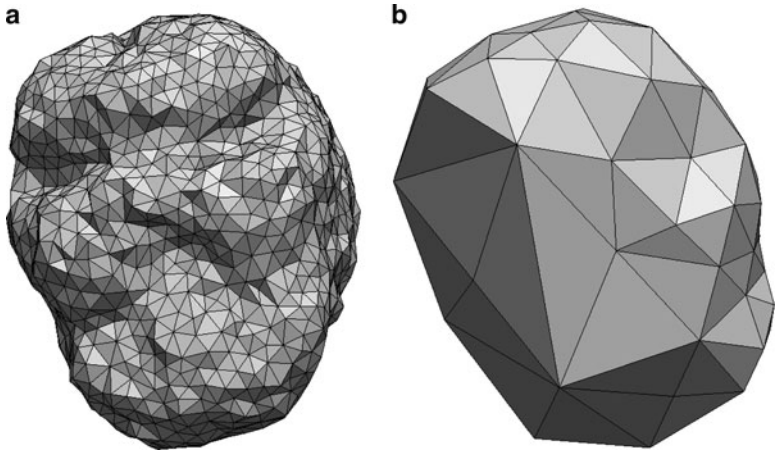

Fig. 3 Meshes produced by Tetgen and CGAL. (**a**) H equal to 5.88 (best fidelity). (**b**) H equal to 23.23 (worst fidelity)

Table 3 Meshes with varying fidelity obtained by PBM

H	Minimum dihedral angle	Average minimum dihedral angle	#Tetrahedra	#Vertices	Condition number	Error
21.02	60.00	60.00	465	139	122,470.00	0.19
19.56	60.00	60.00	1,144	303	203,230.00	0.53
18.30	60.00	60.00	2,126	519	223,540.00	0.50
15.39	41.21	54.43	465	139	19,711.00	0.17
14.25	35.54	54.48	1,144	303	23,405.00	0.35
13.94	31.68	53.83	1,144	303	21,213.00	0.29
13.58	19.41	53.09	1,144	303	18,980.00	0.27
12.61	39.27	53.81	465	139	16,897.00	0.18
12.02	35.77	53.55	465	139	15,978.00	0.19
10.39	34.13	54.78	2,126	519	29,397.00	0.17
9.88	31.92	54.22	2,126	519	25,926.00	0.17
9.39	30.04	53.63	2,126	519	23,485.00	0.17
7.01	59.99	60.00	18,780	3811	367,690.00	0.06
6.42	14.28	55.15	5,764	1277	21,300.00	0.15
5.25	35.61	56.83	18,780	3811	101,700.00	0.09
4.99	31.92	56.47	18,780	3811	78,449.00	0.09
4.94	27.50	56.13	18,780	3811	76,065.00	0.09

and Tetgen. Again, we observe that fidelity does not play that important role in the accuracy of the NRR. Even meshes with very bad fidelity yield an error less than half the size of the voxel. Figure 4 illustrates the meshes obtained by PBM for the best and the worst fidelity.

As you can see in the last two rows of Table 2 (where the error is n/a), the low average minimum dihedral angles seem to substantially affect the speed of the solver:

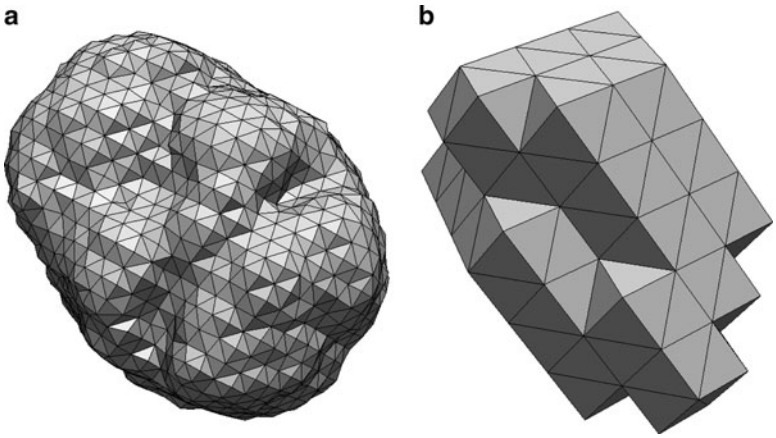

Fig. 4 Meshes produced by PBM. (**a**) H equal to 4.94 (best fidelity). (**b**) H equal to 21.02 (worst fidelity)

Table 4 Timings (in seconds) for various meshes obtained by different methods. Both the mesh and the solver execution times are reported

	HQD			Tetgen			PBM		
H	Mesher	Solver	Total	Mesher	Solver	Total	Mesher	Solver	Total
15–16.5	6.89	0.04	6.93	0.01	0.06	0.07	132.34	0.05	132.39
14–15.5	6.4	0.05	6.45	0.01	0.17	0.18	165.02	0.06	165.08
13–14.5	10.23	0.06	10.29	0.02	0.16	0.18	164.93	0.06	164.99
8.5–9.5	21.57	0.08	21.65	0.09	4.88	4.97	189.19	0.09	189.28
7–8	17.62	0.46	18.08	0.13	**45**	**45.13**	263.39	0.19	263.58

in these two specific runs the solver did not even converge. Also, see that in these two rows the condition number is extremely large. We wanted to look into the timings of both the meshers and the solver in more depth, and see what the merit of fidelity to speed is.

We selected five meshes from each method of approximately the same fidelity and measured the time for meshing and the time for solving the registration problem. For each case, the solver has been running until the error becomes less than 0.5 (half the size of the voxel). Table 4 summarizes the results.

We observe that the meshing time of PBM is extremely large: more than 2 min in all cases. Actually, most of this time is spent for the initial BCC creation. On the other hand, the CGAL+Tetgen scheme is very fast: less than 2 s in all cases, even for the bottom mesh that consists of 2,539 elements.

As far as the solver's time is concerned, PBM yields the best meshes. Overall, however, the registration process is much slower than the other methods due to the time consuming mesh generation time. For Tetgen, the solver took much time, when the Hausdorff distance dropped below 8.5 (see bold entries). As Table 2 shows, the minimum dihedral angle for this fidelity is more than 1°, but the very low

average minimum dihedral angle (the lowest among all the methods) seems to affect the condition number a lot and consequently the speed of the solver. Although the HQD meshes have elements with very small angles, the average minimum angle is much better than Tetgen (10–15° larger). This is why when the solver ran on HQD's meshes, its execution time was less than 2 s in all cases, yielding a good overall execution time, even when the H distance drops below 8.5.

5 Conclusions

In this section, we summarize our findings. The two Delaunay meshes (i.e., HQD and Tetgen) exhibit low quality when the fidelity increases substantially (when the Hausdorff distance drops below 8 units approximately, in our case studies). As Tables 1 and 2 show, this quality deterioration yields a very large condition number which affects the execution time of the solver (see Table 4). We also observe that not only the minimum but also the average minimum dihedral angle plays an important role to the solver's speed. To see it, compare the solver's speed of HQD to the solver's speed of Tetgen when the Hausdorff distance of the meshes is between 7 and 8 units. When Tetgen's mesh was used, the solver was 45 times slower. For these values of fidelity, Tetgen meshes have better minimum dihedral angles than HQD meshes, but they also have much lower average minimum dihedral angles (15° smaller), which is likely to be the reason for a much worse condition number and the consequent large execution time of the solver.

The accuracy of the solver on the meshes produced by the two Delaunay meshers does not fluctuate significantly by the different fidelity values (see Tables 1 and 2). That means that the need for good surface approximation does not seem to affect the accuracy of the solver. Meshes approximating very crudely the object surface (see Figs. 2b and 3b for an illustration) yielded an error less than half the voxel size.

The main characteristic of the optimization-based mesher (i.e., PBM) is the high minimum and average dihedral angles, even in the case of very good fidelity. The reason is because relatively dense initial BCCs can easily capture the object surface without so much compression, thus preserving the good angles of the BCC triangulation. Of course, the number of elements increases significantly, which makes the mesh generation time extremely slow (see Table 4). We also observe that the solver on PBM's meshes exhibits the least error, which in fact is achieved when fidelity is very good (less than 5 units approximately). This is reasonable because, as Table 3 suggests, good fidelity does not deteriorate the quality as much as is the case for the two Delaunay meshes. Note, however, that even when the PBM meshes have very bad fidelity (see Fig. 4b, the error does not increase significantly.

Acknowledgments This work was supported (in part) by the NSF grants CCF-0916526, CCF-0833081, and CSI-719929 and by the John Simon Guggenheim Foundation.

References

1. CGAL, Computational Geometry Algorithms Library. http://www.cgal.org
2. Archip, N., Clatz, O., Fedorov, A., Kot, A., Whalen, S., Kacher, D., Chrisochoides, N., Jolesz, F., Golby, A., Black, P., Warfield, S.K.: Non-rigid alignment of preoperative MRI, fMRI, DT-MRI, with intra-operative MRI for enhanced visualization and navigation in image-guided neurosurgery. Neuroimage **35**(2), 609–624 (2007)
3. Bajaj, C.L., Oden, J.T., Diller, K.R., Browne, J.C., Hazle, J., Babuska, I., Bass, J., Bidaut, L., Demkowicz, L.F., Elliott, A., Feng, Y., Fuentes, D., Kwon, B., Prudhomme, S., Stafford, R.J., Zhang, Y.: Using Cyber-Infrastructure for Dynamic Data Driven Laser Treatment of Cancer. In: International Conference on Computational Science, pp. 972–979 (2007)
4. Boissonnat, J.D., Oudot, S.: Provably good sampling and meshing of surfaces. Graphical Models **67**(5), 405–451 (2005)
5. Cheng, S.W., Dey, T.K., Edelsbrunner, H., Facello, M.A., Teng, S.H.: Sliver exudation. Journal of the ACM **47**(5), 883–904 (2000)
6. Clatz, O., Delingette, H., Talos, I.F., Golby, A.J., Kikinis, R., Jolesz, F., Ayache, N., Warfield, S.: Robust non-rigid registration to capture brain shift from intra-operative MRI. IEEE Transactions on Medical Imaging **24**(11), 1417–1427 (2005)
7. Delingette, H., Ayache, N.: Soft tissue modeling for surgery simulation. Handbook of Numerical Analysis, Computational Models for the Human Body **XII**, 453–550 (2004)
8. Ferrant, M.: Physics-based deformable modeling of volumes and surfaces for medical image registration, segmentation and visualization. Ph.D. thesis, Universite Catholique de Louvain (2001). http://spl.harvard.edu:8000/pages/papers/ferrant/thesis/ferrant.pdf
9. Foteinos, P., Chernikov, A., Chrisochoides, N.: Guaranteed Quality Tetrahedral Delaunay Meshing for Medical Images. In: Proceedings of the 7th International Symposium on Voronoi Diagrams in Science and Engineering, pp. 215–223. Quebec City, Canada (2010)
10. Labelle, F., Shewchuk, J.R.: Isosurface stuffing: fast tetrahedral meshes with good dihedral angles. ACM Transactions on Graphics **26**(3), 57 (2007)
11. Liu, Y., Foteinos, P., Chernikov, A., Chrisochoides, N.: Multi-tissue mesh generation for brain images. In: Proceedings of the 19th International Meshing Roundtable. Chattanooga, Tennessee, USA (2010). To appear
12. Oudot, S., Rineau, L., Yvinec, M.: Meshing Volumes Bounded by Smooth Surfaces. In: International Meshing Roundtable, pp. 203–219. Springer-Verlag, San Diego, California, USA (2005)
13. Rineau, L., Yvinec, M.: Meshing 3D Domains Bounded by Piecewise Smooth Surfaces. In: International Meshing Roundtable, pp. 443–460 (2007)
14. Shewchuk, J.R.: What is a Good Linear Element? - Interpolation, Conditioning, and Quality Measures. In: Proceedings of the 11th International Meshing Roundtable, pp. 115–126. Sandia National Laboratories (2002)
15. Si, H.: Tetgen version 1.4.3. http://tetgen.berlios.de/
16. Jane Tournois, Rahul Srinivasan, Pierre Alliez: Perturbing Slivers in 3D Delaunay Meshes. In: Proceedings of the 18th International Meshing Roundtable, pp. 157–173. Sandia Labs, Salt Lake City, Utah, USA (2009)

Incompressible Biventricular Model Construction and Heart Segmentation of 4D Tagged MRI

Albert Montillo, Dimitris Metaxas, and Leon Axel

Abstract Most automated methods for cardiac segmentation are not directly applicable to tagged MRI (tMRI) because they do not handle all of the analysis challenges: tags obscure heart boundaries, low contrast, image artifacts, and radial image planes. Other methods do not process all acquired tMRI data or do not ensure tissue incompressibility. In this chapter, we present a cardiac segmentation method for tMRI which requires no user input, suppresses image artifacts, extracts heart features using 3D grayscale morphology, and constructs a biventricular model from the data that ensures the near incompressibility of heart tissue. We project landmarks of 3D features along curves in the solution to a PDE, and embed biomechanical constraints using the finite element method. Testing on normal and diseased subjects yields an RMS segmentation accuracy of $\sim$2 mm, comparing favorably with manual segmentation, interexpert variability and segmentation methods for nontagged cine MRI.

Keywords Incompressible biventricular model · Mesh construction · FEM · tMRI

1 Introduction

In most developed countries, cardiovascular disease kills more men and women than any other disease. An automated characterization of myocardial deformation may lead to improved patient diagnosis and treatment. Tagged MRI (tMRI) [1,2] induces an intramyocardial magnetic tag (line) pattern throughout the heart and can image the tagged soft heart tissue through bone noninvasively, making it a gold standard for measuring regional myocardial deformation abnormalities. However, tracking the deformation requires the dynamic segmentation of the outer (epicardial) and inner (endocardial) heart boundary surfaces, and tracking the tags.

A. Montillo (✉)
GE Global Research Center, Niskayuna, NY, USA
and
Department of Computer Science, Rutgers University, Piscataway, NJ, USA
e-mail: montillo@ge.com

A. Wittek et al. (eds.), *Computational Biomechanics for Medicine: Soft Tissues and the Musculoskeletal System*, DOI 10.1007/978-1-4419-9619-0_15,

Dynamic segmentation of these boundary surfaces is important for many reasons. First, it can facilitate a wide variety of tag tracking methods. Tag tracking methods based on tag sheet tracking, including [3–5] optical flow and HARP [3], rely upon manually segmented boundaries to improve performance by restricting the tags tracked to just those within the myocardium. This manual segmentation is tedious and operator dependent. Second, if the boundaries can be segmented, interpolating the 3D motion throughout the myocardium with a finite element method (FEM) model becomes possible, even in thin-walled structures, such as the right ventricle (RV) [3, 7], where there is a sparsity of tags. Third, segmenting the walls also provides a necessary boundary condition to study the distribution of myocardial stress [8]. The fourth reason is that the heart boundaries from tMRI can be used to calculate classical descriptors of heart function at the same accuracy as those obtained through nontagged MRI [9].

The most desirable tMRI segmentation must not only handle the arduous processing challenges specific to tMRI, but also be fully automated, perform 3D biventricular segmentation, and impose the near incompressibility constraint of real myocardial tissue. Full automation is essential to provide the response time and objectivity necessary for routine clinical use. Most previous tMRI segmentation methods are either manually driven or tend to require manual editing, e.g. [4, 10]. More recent methods, e.g. [11–16], have one or more of these limitations: they provide only a 2D analysis [12], segment only one surface of one ventricle [13], or only segment one ventricle and require manually drawn initial contours or landmarks [14–16], or do not impose incompressibility [11]. 3D analysis is required to handle cases in which the heart appears to change topology as portions of the heart move into and out of the 2D image planes. Incompressibility should be imposed to ensure physiologically sound segmentation throughout systole.

Many segmentation methods have been proposed for imaging modalities *other* than tMRI such as cardiac ultrasound, CT, and nontagged cine MRI, including [17–20]. However, segmentation results are *not* shown for tagged MRI, primarily due to the arduous processing challenges of tMRI: (1) image artifacts including intensity inhomogeneity and intersubject intensity variation must be suppressed, (2) tag lines that obscure heart boundaries must be removed, (3) boundary-delineating features must be extracted despite low image contrast, and (4) the inherently 5D data (3D + time + tag line orientations) must be fused into a single coherent interpretation.

Our objective is to develop a method that segments the 3D biventricular myocardium in tMRI throughout the heart's contraction without requiring user input. We construct a *volumetric* biomechanical model with the near incompressibility constraint of real myocardial tissue in order to (1) yield physiologically sound segmentation and (2) so that epicardial (epi) and endocardial (endo) walls do not merge together, a common failure mode that plagues many *surface*-based segmentation methods.

In Sect. 2, we present four steps of our method: (1) image artifact suppression, (2) feature extraction, (3) volumetric biomechanical model construction, and (4) model fitting. We present our segmentation results in Sect. 3 and provide discussion and conclusions in the final section.

2 Methods

Each time frame of our tMRI consists of three sets of image planes: two short axis (SA) sets and one long axis (LA) set. The SA sets differ with tags running in vertical or horizontal directions (Fig. 1a). Several challenges we face are also illustrated: in Fig. 1a, the use of surface coils can cause intrasubject intensity inhomogeneity; in Fig. 1b, images with 1 mm^2 in-plane resolution come in sparse parallel planes with 8 mm spacing and sparse radially planes with 20° separation; and in Fig. 1c, the lack of intrinsic baseline for MR, can cause intersubject intensity variation at the same windowing level.

2.1 Artifact Suppression

Previous intensity inhomogeneity correction methods assume a priori segmentation, intensity distribution, or are not suited for radially arranged images. To solve, we iterate the following steps (Fig. 2) until the set of sampling points is constant: (1) compute scale at every pixel, where scale is defined as the radius of the largest ball, centered at the pixel, for which pixel intensity homogeneity measures are preserved including the pixel intensities and the gradient magnitude of the intensities in the neighborhood around the pixel, (2) find largest connected component with maximum scale, (3) fit a Gaussian to its intensity distribution, and define field sampling points as those with intensities within 1σ of the mean of this Gaussian, (4) estimate inhomogeneity by fitting second degree polynomial to sampling point intensities, and (5) divide current image intensities pixel-wise by inhomogeneity estimate. Step 2 estimates a region likely to belong to the same tissue. To better sample the inhomogeneity, step 3 extends this region to include nonconnected points which have similar intensities. For further details and performance on noncardiac images see [21].

To suppress intersubject variations, previous methods, such as [22] map zero crossings (zc) in a test image to those in a high contrast reference standard image, I_{HC}. However, in tMRI, zero crossings are unreliable, as foreground and background histogram peaks tend to merge (Fig. 3a). To solve, we characterize the cumulative

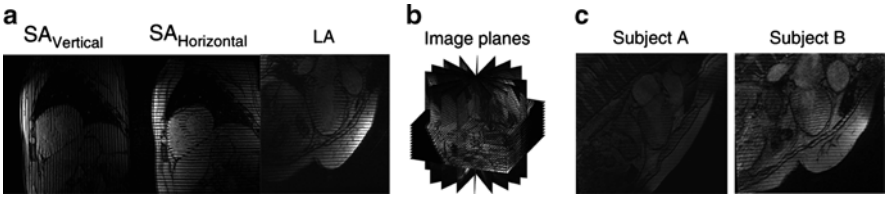

Fig. 1 Raw tMRI: (**a**) 3-tag orientations, (**b**) sparse images, (**c**) intersubject variation

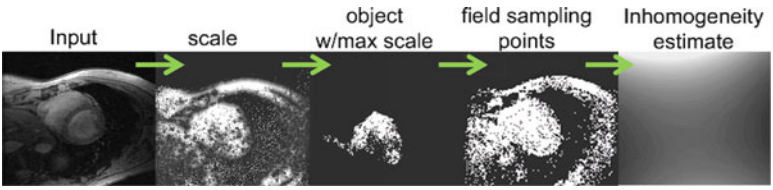

Fig. 2 From left to right, the iterative intensity inhomogeneity correction steps

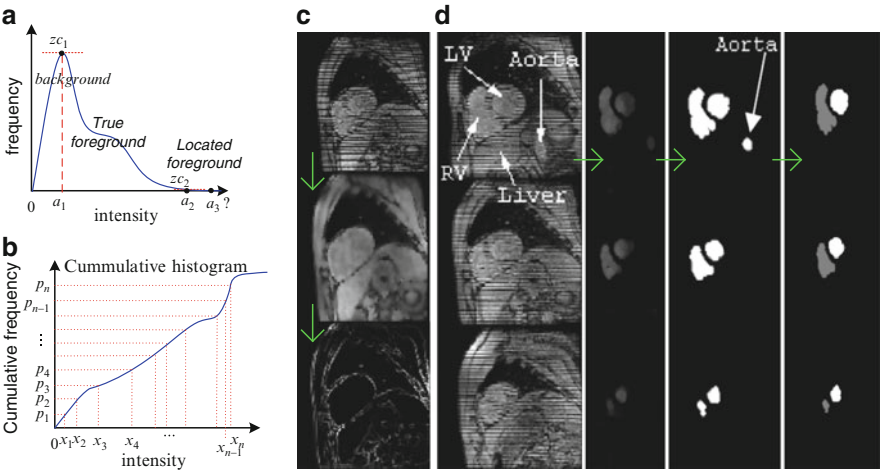

Fig. 3 (**a**, **b**) Intersubject variation suppresion. (**c**, **d**) Features for epi and endo surfaces

tMRI histogram by its intensities $\widetilde{x}_1, \ldots, \widetilde{x}_{16}$ at a uniform distribution of percentiles, $p_1, \ldots, p_{16}$ (Fig. 3b). We then map original intensities to those of I_{HC} using linear interpolation to make all images have the high contrast of I_{HC}.

2.2 *Feature Extraction*

Segmenting the biventricular myocardium requires locating the heart and delineating the boundaries of the epicardial surface and the RV and LV endocardial surfaces. To find epicardial boundary features, we perform a grayscale morphological closing with a linear structuring element whose length is equal to tag separation distance, d_{sep} (a known MR pulse sequence parameter), noise suppress, and then perform edge detection (Fig. 3c). To find endocardial boundary features, we observe that the whole image is tagged except for blood because the motion of the blood washes away the tags (Fig. 3d).

Therefore, to isolate blood regions, we apply a 3D grayscale opening operation with a cylinder-shaped structuring element whose radius is $2d_{\mathrm{sep}}$ and whose height

spans four parallel image planes. We threshold the output to form blood regions and prune them to just the ventricular blood regions (Fig. 3d, third and fourth columns). We do this by finding the regions with highest spatial–temporal consistency score. This score is measured by the overlap with regions in the same frame but in different image planes through the heart, and in the same image plane but over time. The LV and RV blood is the pair of regions that appears most consistently over space and time.

2.3 Model Construction

2.3.1 Early Systolic Heart Shape Estimate

We form an estimate of the pose, size, and shape of the heart's ventricles by combining the blood region features from the early part of systole, i.e., from the first 1/3 of time frames. In the images of this early part of systole, we automatically determine the most superior SA image to use to form our model, by identifying the most superior SA image for which the RV blood region features found in Sect. 2.2 have not bifurcated into inflow and outflow tracks. We include this image and all inferior images in the following model construction step. For these early systolic images, we interpolate each stack of region features over space using 2.5D shape interpolation [23] which forms a 2.5D distance transform (DT). This is the same pixel from which each SA image is spline interpolated to form intensities between our sparse image planes. We then compute true 3D DTs representing the blood shapes (denoted $\mathbb{D}_{\text{RVB}}, \mathbb{D}_{\text{LVB}}$) by the Euclidian distance to the zero surface (Fig. 4, step 1). Then we form a robust estimate of the early systolic ventricles by averaging the 3D DTs from both SA tag orientations and all early systolic frames (Fig. 4, step 2).

We form the epicardial surface from two components. The first component, the LV epi surface (zero surface of $\mathbb{D}_{\text{LVEpi}}$), is formed by dilating the LV endocardial surface by an estimate of the LV thickness, $\alpha_{\text{LVThickness}}$ by subtracting a fixed distance from its 3D (signed) DT representation.This is estimated from the separation of LV and RV endo features. The 2nd component, the RV epi surface, is the zero

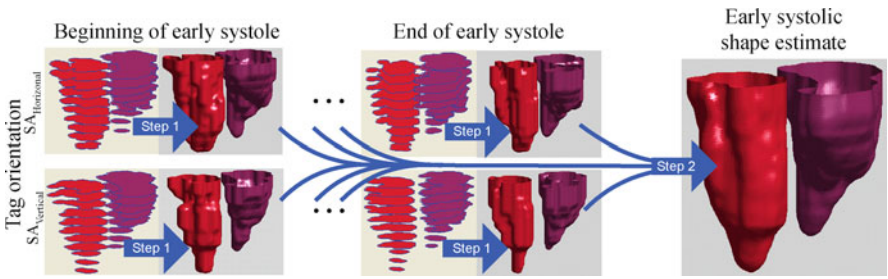

Fig. 4 Region features are fused to form early systolic estimate of endo surface shape

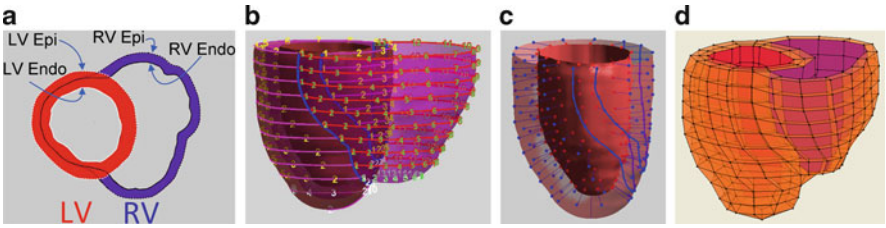

Fig. 5 (**a**) Blood surfaces are joined to form epi surface. Circumferential and longitudinal (**b**) and transmural (**c**) coordinate curves enable mesh construction (**d**)

surface of $\mathbb{D}_{\text{RVEpi}}$ which is formed by combining the dilated RV blood shape, $\mathbb{D}_{\text{RVB}}$, and the LV blood shape, $\mathbb{D}_{\text{LVB}}$, using an energy representation with exponentiation operator:

$$\mathbb{D}_{\text{RVEpi}} = \exp\left(-\frac{\mathbb{D}_{\text{RVB}} - \alpha_{\text{RVThickness}}}{\alpha_{\text{RVThickness}}}\right) + \exp\left(-\frac{\mathbb{D}_{\text{LVB}} - 0.5(\alpha_{\text{LVThickness}})}{1.5(\alpha_{\text{LVThickness}})}\right) \quad (1)$$

where $\alpha_{\text{RVThickness}} = (1/2)\alpha_{\text{LVThickness}}$. This forms a surface surrounding the RV endo as shown in 2D cross-sectional view in Fig. 5a. The portion of this implicit surface outside the LV epi (i.e., $\mathbb{D}_{\text{LVEpi}} > 0$) is retained as RV epi and joined to the LV epi.

2.3.2 Mesh Construction

Constructing a finite element model requires a mesh for the volume between the epicardial surface and endocardial surfaces. To form the mesh we create coordinate curves that map where mesh element vertices will be. Circumferential coordinates are evenly distributed on the combined epi surface according to arc length, starting at the line of insertion (blue) of the RV epi into LV epi as shown in Fig. 5b. Longitudinal coordinates are distributed evenly from apex to base. Transmural coordinates are distributed along curves running from outer to inner wall which are formed by computing the characteristic curves through the solution, $\bar{v}^*$, that minimizes the 3D version of gradient vector flow (GVF) [24] equation:

$$\begin{aligned}\bar{v}^* &= \arg\min_{\bar{v}} E(\bar{v}) \\ &= \arg\min_{\bar{v}} \iiint \mu\left(u_x^2 + u_y^2 + u_z^2 + v_x^2 + v_y^2 + v_z^2 + w_x^2 + w_y^2 + w_z^2\right) \\ &\quad + |\nabla f|^2 |(\bar{v} - \nabla f)|^2 \, \mathrm{d}x\mathrm{d}y\mathrm{d}z \end{aligned} \quad (2)$$

where μ balances smoothing and data fidelity. The gradient is taken on the function f which is a discrete grayscale labeled volume with dark intensity pixels outside the heart, medium gray between the walls, and bright white ventricular blood pixels.

For all our subjects, $\mu = 0.15$. To minimize this functional, we use the calculus of variations to derive the necessary condition: $\bar{v}_t = \mu\nabla^2\bar{v} - |\nabla f|^2(\bar{v} - \nabla f)$ and iterate until the equilibrium solution, $\bar{v}^*$. Starting from each epicardial node formed along the circumferential directions, we traverse the characteristic curve in $\bar{v}^*$ until we reach an endocardial surface. We then evenly divide each projection curve by arc length. Example characteristic curves are shown as thin blue lines in Fig. 5c for the LV. We also apply this for transmural RV curves. Connecting neighboring points along the coordinate curves forms mesh elements (Fig. 5d).

2.3.3 Biomechanical Model

For segmentation, we model the myocardial tissue as an elastic material characterized by Young's modulus E, and Poisson ratio, ν. We denote the strain-displacement matrix as $\mathbf{B}$ and the material property matrix as $\mathbf{P}$, and use: $\mathbf{K}_{\text{el}}(\mathbf{P}(E,\nu)) = \iiint \mathbf{B}^{\mathrm{T}}\mathbf{P}\mathbf{B}\,dV$ [25] as the formulation of the stiffness matrix for each mesh element. We assemble the global stiffness matrix $\mathbf{K}$ from K_{el} [26] using the finite element method. Our model's internal forces are then $\mathbf{Kq}$ where $\mathbf{q}$ is the vector of mesh nodes positions. As the myocardium is nearly incompressible, we use $\nu = 0.4$ while we empirically choose $E = 0.1$ megapascals (MPa), a value that provides realistic smoothness for the quality of the images we acquired. The value of $E$is less critical and can be varied while still producing similar overall segmentation results.

2.4 Fit Model to Dynamically Segment Patient-Specific Anatomy

Image forces guide the fitting of our model to patient anatomy for each frame. Inner walls are attracted to forces from blood features and the outer wall to the edge features that we extracted in Sect. 2.2 for each image plane. We compute the gradient of these feature images and employ GVF to increase their capture range. We do not apply a 3D gradient operator to an interpolated isotropic voxel volume because the widely spaced image planes make isotropic voxel volumes less representative of anatomy. Instead, we compute the intersection of our model's edges with the image planes. The 2D image force acting on each edge intersection point is affine distributed to the edge's two endpoints (i.e. the model's nodes) based on the distance of the intersection point to each endpoint. This forms our model's external forces, f_{ext}.

We formulate model fitting as force balance equation in which internal and external forces compete to explain the data. The motion of model's nodes is governed by a second order Lagrangian equation: $\mathbf{M}\ddot{\mathbf{q}} + \mathbf{D}\dot{\mathbf{q}} + \mathbf{Kq} = f_{\text{ext}}$. Setting $\mathbf{M} = 0$ and $\mathbf{D} =$ identity leaves $\dot{\mathbf{q}} + \mathbf{Kq} = f_{\text{ext}}$. We solve this with numeric integration, which we iterate until the forces equilibrate or vanish.

To track the heart's shape change throughout systole, we begin by fitting the model to the first frame, t_n, in which the motion of the blood has washed away the

tags. To fit subsequent time frames ($t > t_n$) we propagate the previous frame solution and fit the model in the new frame. To fit earlier time frames, (e.g. t_{n-1}), we propagate the solution from t_n and fit the model but we do not apply forces to the endocardial walls because the insufficient blood–myocardium contrast yields unreliable blood regions features, however, both the epicardial and endocardial surfaces are recovered because of (1) the incompressibility constraint, (2) the equilibrium model fit at t_n, and (3) reliable epicardial features at t_n and t_{n-1}.

3 Results

We acquired tMRI data from ten subjects: eight normal and two with right ventricular hypertrophy. Each sequence contains 12–15 frames; each frame contains three volumes (2D img. sets) with one set in each of three orthogonal tag orientations. In total, we collected 1,160 2D images. Two (2) expert physicians segmented the LV and RV endocardial boundaries, and the epicardial boundary providing the ground truth for evaluation purposes. We form expert surfaces from expert contours using a process similar to the one described in Sect. 2.3 for converting 2D blood region features into 3D surfaces, only now we form 3D distance transforms from stacked expert contoured regions. For each expert, this produces one 3D DT for each of feature (i.e., LV endo, RV endo, and combined LV and RV epi) whose zero isosurface defines an expert surface.

3.1 Artifact Suppression Results

During acquisition, surface coils are placed on the subject's chest, S_c, and back, S_b (Fig. 6a). Coils improve SNR but cause pixels in coil vicinity to be brighter than those in the deep thoracic region, labeled DpTh. When we suppress the intensity inhomogeneity artifact in the raw input tMRI (Fig. 6a, first column) it causes

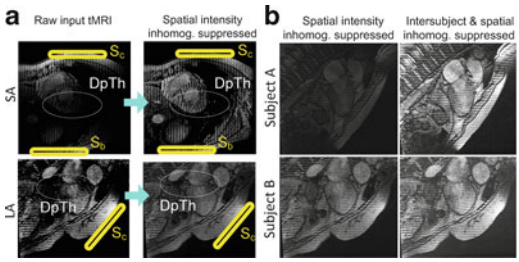

c

	NSD of myocardium	$\sigma_{intersubj}$
% reduced	33.0%	13.5%
p-value	p<0.0001	p<0.0001

d

	Epi	RV endo	LV endo
% increase	75.0%	68.0%	92.8%
p-value	P<0.0001	p<0.0001	p<0.0001

Fig. 6 Examples of intrasubject (**a**) and intersubject (**b**) intensity variation suppression. Database-wide reduction in intensity variations (**c**) also increases (**d**) boundary edge strength

DpTh region contrast to be visibly increased (Fig. 6a, second column). Additionally, MR lacks an intrinsic baseline signal level causing intersubject intensity variations shown in Fig. 6b first column (also Fig. 1c). Our histogram standardization creates more consistent image contrast across subjects (Fig. 6b, second column). Statistical analysis of the 1,160 images (Fig. 6c) shows our intrasubject intensity inhomogeneity suppression yields 33.0% reduction in the normalized standard deviation (NSD) of the (tag removed) myocardial pixel intensities. The intersubject intensity variation suppression yields a 13.5% reduction in the standard deviation of the mean myocardial pixel intensity ($\sigma_{\text{intersubj}}$) across the subjects in our database.

We measured the cumulative effect of our artifact suppression methods by computing the mean magnitude of the image gradient orthogonal to the expert boundaries at points distributed evenly on the boundary. Figure 6d shows our artifact suppression caused all-boundary edge strengths to increase. The epicardial boundary edge strength increased by 75.0%, RV endo by 68%, and LV endo by 92.8%.

3.2 Segmentation Results

Figure 7 is representative of the physiologically sound segmentation from our method. The model's outer surface is transparent here to view the mesh and inner surfaces. The 3D model is intersected by a 2D LA image. From this perspective, we can see (1) the model's near incompressibility constraint maintains sound surface-to-surface separation even of the intervening septal wall and (2) the contraction of the LV endocardial surface from early to end systole (left to right).

Figure 8 shows solid curves for the intersection of our 3D model with an image plane, and dashed curves for the expert's boundaries. Representative results from one subject are shown in (a) and from another subject in (b). High correspondence between segmented and expert boundaries is evident throughout contraction in both the SA and LA images, the latter of which is not handled by other methods such as [12, 27].

We also perform a quantitative validation of our method to measure its accuracy. Specifically, we compute the distance between points on each model surface, (denoted by A), and points on the corresponding expert surface, (denoted by B)

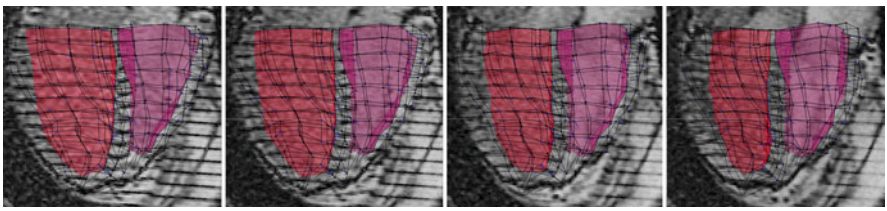

Fig. 7 3D model intersected by images during systole. LV endo (*red*) and RV endo (*purple)*

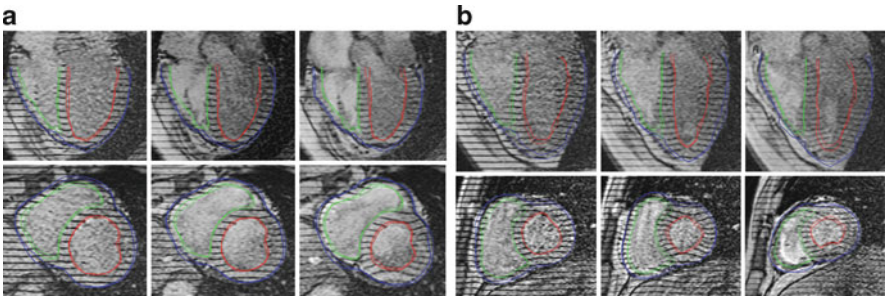

Fig. 8 (**a**) shows the image plane curves in early to end systole (from *left* to *right*), with *green* = RV endo, *red* = LV endo, *blue* = epi. Model (*solid*); experts (*dashed*), (**b**) is another subject

Table 1 Distance errors across subjects, Man = inter-expert, Auto = method-to-expert distance

Error measurement	Method	LV endocardial	RV endocardial	Epicardial	All surfaces
RMS	Man	1.78 ± 0.39	1.88 ± 0.63	1.35 ± 0.54	1.58 ± 0.46
	Auto	2.00 ± 0.41	2.58 ± 0.63	2.51 ± 0.12	2.38 ± 0.36
Median	Man	1.51 ± 0.32	1.41 ± 0.45	1.03 ± 0.48	1.19 ± 0.40
	Auto	1.63 ± 0.26	2.18 ± 0.54	2.06 ± 0.02	1.94 ± 0.25

using: $d(a, \boldsymbol{B}) = \min_{b \in \boldsymbol{B}} \|a - b\|$ for all points a on the model surface. In Table 1, the first error measure is the average root mean squared (RMS) distance across subjects; the second is the average median error across the subjects. For each error measure the first entry (Man) is the distance between the experts' manual delineations, while the second entry (Auto) is the distance between our method and the corresponding expert surface. The errors are computed for each surface and for all surfaces combined. Overall our method's RMS error is only $\sim$1 mm more than the interexpert distance. Our RMS error varies from 2.0 mm for the LV endo to 2.58 mm for the RV endo. The average median error across subjects is the second entry which is slightly lower than RMS error. Standard deviation is small for all measures, indicating we are consistently locating the boundary surfaces well across the subjects. Previous methods [12, 27] reporting $\sim$1 mm accuracy require *as input* the expert's contours in the first frame. Our method does not require this input as it solves heart localization automatically as part of the segmentation task.

4 Discussion and Conclusions

It is insightful to compare our method to a single statistical atlas approach. A challenge for our model from data-fusion (MFDF) approach is building adequate acquisition postprocessing to suppress image artifacts, while a challenge for a single statistical atlas is acquiring enough representative data of all patient variations. When the data is of high quality or when image examples are scarce (e.g. due to a substantially new MR pulse sequence, or lack of patients with a particular

condition), MFDF may be preferable. Another potential advantage of MFDF is that it may be applicable to a range of myocardial diseases since the method does *not* depend on the similarity of the test subject to samples in a training dataset. For example, MFDF may be adaptable for congenital heart disease (CHD). In CHD anatomical abnormalities such a hole in the septal wall can occur. In such cases, MFDF may be able to discover the topological variation (i.e., a hole) and construct a patient-specific model. Other methods that impose a defect-free model onto the diseased heart may be less able to segment the boundaries and abnormal motion. In such cases MFDF might be used to seed the statistical atlas with the required training segmentations, and this is an area of future work.

We have chosen not to incorporate muscle fiber orientations into our cardiac model for two reasons. The first is that we use the model for two distinct model fitting phases. In phase 1 we fit the early systolic approximate shape model to the specific patient anatomy in the first systolic frame in which the tags are not visible in the blood. In this case, the model adapts to the patient anatomy from an average and adding fiber orientations may over constrain. In phase 2, the model is propagated to earlier and later time frames. Here, it may make sense to add fiber orientations to further regularize, however, most clinics are currently not equipped to acquire patient-specific fiber orientation data in vivo, and assuming a standard orientation may add bias.

Our successful segmentation of low blood–myocardium contrast tMRI with spatially sparse 2D image samples suggests good potential applicability to segment higher contrast SSFP tMRI [28] and densely sampled true 3D tMRI [29]. In addition, our method is likely adaptable to still other types of tMRI. For example, for 2D grid tagging, our blood feature extraction (the most critical task) should work well since there are fewer bright pixels to suppress with the morphological opening. Epicardial features may be extracted, in part, through a slight modification: applying a closing with two orthogonal linear structuring elements and is a topic for future testing. Also, our method does not require perfect intersection of LA image planes; as long as the pose of each image plane is provided, then our region and edge features can be added to the overall set of features that guide modeling fitting.

There are several limitations of our method which are areas for our future work. First, our incompressible model does not yet follow the longitudinal descent of the valves toward the apex. For this, tag motion in LA images might be used to further guide model fitting. Second, the problem of papillary muscles is not fully addressed. We have chosen to include the parts of the papillary muscles that are clearly visible in tMRI (the papillary buds) with the myocardium. This was done for two reasons: (a) we are now in good position to exploit motion data visible from the papillary tags for future 3D motion recovery and (b) we do introduce additional uncertainty. Third, there are artifacts which we do not yet handle including (a) RF interference, (b) images that self-overlap (wrap-around) from aliasing, and (c) distortion from metal implants. The second and third artifacts can make the images difficult to interpret even by expert radiologists. Fourth, “slice misalignment” can be caused by respiratory-induced heart motion. Suppression methods proposed in the literature include breath-hold acquisition, respiratory gating, slice-following, and true 3D

MRI. Breath-hold and respiratory gating are the methods we use. However, breath-hold is not viable for some subject and respiratory gating can lengthen scan time. True 3D MRI is promising but requires the most advanced acquisition hardware and pulse sequences. If none of the methods for mitigating slice misalignment are available another motion correction is required and this remains an open research problem. Lastly, many methods do not attempt to segment either the apex of the LV or RV [12,13,20,27]. Our method attempts both, and does a good job at segmenting the LV apex but tends to truncate the RV apex. Causes include (1) our data samples the LV more densely than the RV, (2) RV apex tends to be narrower, (3) in some cases, RV apex is smaller than the opening structure element which works well to locate the remainder of the RV blood. Future work includes refining the features from this region.

In conclusion, we have presented a MFDF-based biventricular segmentation of the full complement of tMRI data, which required no user input. The model fitting consumes <3 min of CPU time to fit all frames on a dual core desktop, and obviates the interactive contouring task that requires up to 3 h/subject.

References

1. Axel L, Dougherty L. Heart wall motion: improved method of spatial modulation of magnetization for MR imaging. Radiology. 1989;172:349–350.
2. Zerhouni E, Parish D, Rogers W, Yang A, Shapiro E. Human heart: tagging with MR imaging-a method for non-invasive assessment of myocardial motion. Radiology. 1988;169:59–63.
3. Haber I, Metaxas D, Axel L. Three-dimensional motion reconstruction and analysis of the right ventricle using tagged MRI. Med Image Anal. 2000;4(4):335–355.
4. Tustison N, Amini A. Myocardial kinematics based on tagged MRI from volumetric NURBS models. In: SPIE. vol. 5369; 2003.
5. Young A, Axel L. Three-dimensional motion and deformation of the heart wall: estimation with spatial modulation of magnetization–a model-based approach. Radiology. 1992;185:241–247.
6. Osman N, Prince J. Angle images for measuring heart motion from tagged MRI. In: ICIP; 1998. p.704–8.
7. Young A, Fayad Z, Axel L. Right ventricular midwall surface motion and deformation using magnetic resonance tagging. Am J Physiol. 1996;271:H2677–H2688.
8. Hu Z, Metaxas D, Axel L. In vivo strain and stress estimation of the heart left and right ventricles from MRI images. Med Image Anal. 2003;7(4):435–444.
9. Dornier C, Ivancevic M, Lecoq G, Osman N, Foxall D, Righetti A, et al. Assessment of the left ventricle ejection fraction by MRI tagging. In: ISMRM; 2002.
10. Guttman M, Prince J, McVeigh E. Tag and Contour Detection in Tagged MR Images of the Left Ventricle. IEEE Trans Med Imaging. 1994;13(1):74–88.
11. Montillo A, Metaxas D, Axel L. Automated deformable model-based segmentation of the left and right ventricles in tagged cardiac MRI. In: MICCAI; 2003. p. 507–515.
12. Qian Z, Metaxas D, Axel L. Boosting and nonparametric based tracking of tagged MRI cardiac boundaries. In: MICCAI; 2006. p. 636–644.
13. Huang J, Huang X, Metaxas D, Axel L. Adaptive Metamorphs Model for 3D Medical Image Segmentation. In: MICCAI; 2007.
14. Sundar H, Davatzikos C, Biros G. Biomechanically-Constrained 4D Estimation of Myocardial Motion. In: MICCAI; 2009.
15. Chandrashekara R, Mohiaddin R, Razavi R, Rueckert D. Nonrigid Image Registration with Subdivision Lattices: Application to Cardiac MR Image Analysis. In: MICCAI; 2007.

16. Zhang S, Wang X, Metaxas D, Chen T, Axel L. LV surface reconstruction from sparse tMRI using laplacian surface deformation and optimization. In: ISBI; 2009. p. 698–701.
17. Yang L, Georgescu B, Zheng Y, Meer P, Comaniciu D. 3D ultrasound tracking of the left ventricle using one-step forward prediction and data fusion of collaborative trackers. In: CVPR; 2008.
18. Zhu Y, Papademetris X, Sinusas A, Duncan JS. Segmentation of myocardial volumes from real-time 3D echocardiography using an incompressibility constraint. MICCAI. 2007;10(Pt 1): 44–51.
19. Ecabert O, Peters J, Schramm H, Lorenz C, Von Berg J, Walker MJ, et al. Automatic model-based segmentation of the heart in CT images. IEEE Trans Med Imaging. 2008; 27(9):1189–1202.
20. Bistoquet A, Oshinski J, Skrinjar O. Myocardial deformation recovery from cine MRI using a nearly incompressible biventricular model. Med Image Anal. 2008;12(1):69–85.
21. Zhuge Y, Udupa J, Liu J, Saha P, Iwanaga T. A Scale-Based Method for Correcting Background Intensity Variation in Acquired Images. In: SPIE; 2002. p. 1103–1111.
22. Nyul L, Udupa J, Zhang X. New variants of a method of MRI scale standardization. IEEE Trans Med Imaging. 2000;19(2):143–150.
23. Herman G, Zheng J, Bucholtz C. Shape-based interpolation. IEEE Comput Graph. 1992;p. 69–80.
24. Xu C, Prince J. Generalized Gradient Vector Flow external forces for active contours. Sig Proc. 1998;71:131–9.
25. Cook R, Malkus D, M P. Concepts and applications of finite element analysis. Wiley; 1989.
26. Macneal R. Finite Elements: Their Design and Performance. Marcel Dekker; 1994.
27. Qian Z, Metaxas D, Axel L. Learning methods in segmentation of tMRI. ISBI; 2007. p. 688–691.
28. Herzka D, Guttman M, McVeigh E. Myocardial tagging with SSFP. Magn Reson Med. 2003;49(6):329–340.
29. Ryf S, Spiegel MA, Gerber M, Boesiger P. Myocardial tagging with 3D-CSPAMM. J of Mag Res Imaging. 2002;16:320–325.